Cutting forces in the linear rock cutting process

Validating and expanding cutting force calculation models

Tom Rutten

Delft University of Technology

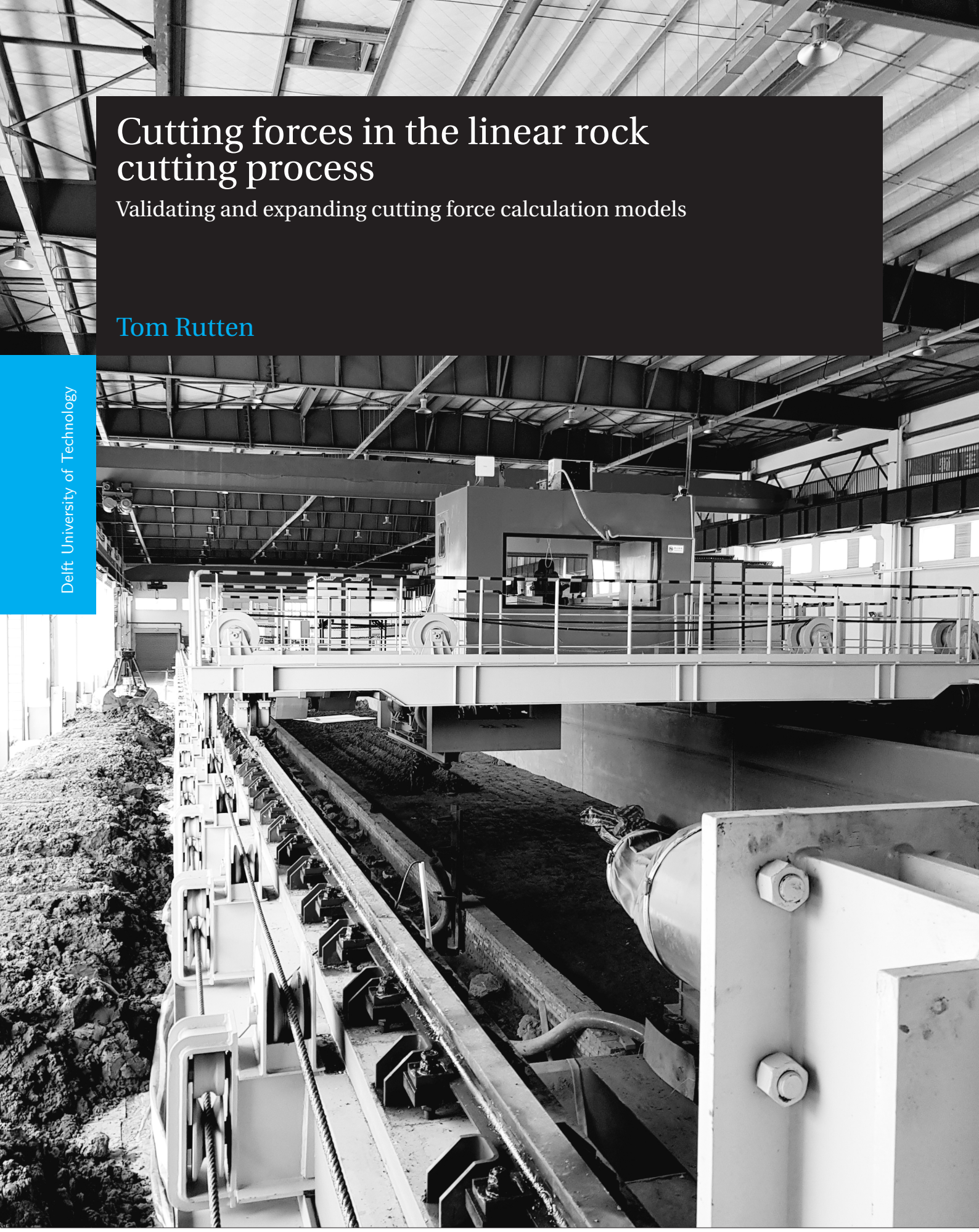

TU Delft Delft University of Technology

Challenge the future

CUTTING FORCES IN THE LINEAR ROCK CUTTING PROCESS

VALIDATING AND EXPANDING CUTTING FORCE CALCULATION MODELS

by

Tom Rutten

in partial fulfillment of the requirements for the degree of

Master of Science
in Offshore Engineering

at the Delft University of Technology.

Daily supervisor:	Dr. G. Liu,	NERCD
Daily supervisor:	Ir. X. Chen,	TU Delft
Chairman:	Dr. Ir. S. A. Miedema,	TU Delft
External member:	Dr. Ir. P. N. W. Verhoef,	TU Delft

TU Delft Delft University of Technology

ABSTRACT

Several calculation models have been developed to predict the cutting forces in the linear rock cutting process. Rock failure can occur in different manners: brittle tensile, brittle shear and ductile. Each failure mechanism has a corresponding calculation model with specific cutting geometries and assumptions to predict the cutting forces as accurate as possible. However, several researches conducted in the past show that the predicted forces can differ considerably from the forces measured in the experiments. In this research the author proposes expansions to the existing models to increase the accuracy of the force predictions and thereby contribute to a more (cost) efficient cutting process.

The calculation models considered in this research are based on two main assumptions: the cutting process is 3D and the tip of the cutting tool is sharp. In a 2D cutting process the width of the cut is equal to the width of the pick point and stays constant throughout the cut. During experiments the sideways outbreaking of rock pieces is observed which can increase the width of the cut tremendously and therefore increase the actual cutting forces. This sideways outbreaking makes the rock cutting process in fact a 3D problem. The assumption of a sharp cutting tool results in another inaccuracy in the force predictions. A sharp cutting tool will penetrate the rock more easily and create a clean cut. If the sharpness of the cutting tool decreases, for example due to wear and tear during the cutting process, a crushed zone will appear in front of the cutting tool, while a wear flat arise at the tip of the cutting tool. These phenomena result in extra forces that has to be overcome by the cutting force. For large cutting depths these effects might be negligible, but for small cutting depths these forces need to be considered. In some applications in the offshore environment only small cutting depths are encountered, such as the vertical drilling for monopile installation or the scraping techniques used in the oil and gas industry. An expansion to include these phenomena in the force prediction models would therefore be a widely applicable concept.

After conducting experiments on sandstone samples the magnitudes of the 2D force prediction models, the forces due to the 3D effects and the indentation forces are established. Afterwards the empirical relations of these terms are composed based on the rock characteristics and cutting geometry. The results of this research show that the proposed expansions increase the accuracy of the cutting force predictions tremendously. It also shows that for cutting at a very small depth the forces predicted by the 2D models are negligible compared to the 3D expansion and the indentation expansion, but the 2D models are necessary to calculate the angle and length of the shear plane. However, if the cutting depth increases the indentation force converges to a constant value and the influence of the 3D expansion decreases as well, while the forces in the 2D models increase. The author therefore suggests to keep the 2D effects into the equation to keep the total formula broadly applicable.

PREFACE

Last year I had the great opportunity to do research at a test facility of a subgroup of the China Communication Construction Company (CCCC): the National Engineer Research Center of Dredging Technology and Equipment. There have been a great number of people that I worked closely together with and that supported me throughout this period, whom I wish to thank. First of all, I would like to thank dr. ir. Miedema and ir. Chen for the time they have dedicated towards helping me successfully write this thesis. They provided me with lots of information and new insights and offered me great feedback during the research. I would also like to thank CCCC for the opportunity to do my research at their company, and especially mr. Hong and dr. Liu, who both put in a lot of effort to provide me all the facilities and guidance that I needed. Also mr. Shao and mr. Liwei who both supported me with the experiments. I enjoyed working together with you very much. Mr. Shuwei, mr. Zang and dr. Sun who helped me with everything from housing to visa applications and therefore contributed a lot to my pleasant stay in China. Also everyone from the department of geotechnical engineering of the Tongji University in Shanghai for helping me and letting me use their equipment for experiments. All these colleagues made me feel welcome and without them the experimental stage of my thesis would not be as enjoyable as it was. Finally I want to thank my family and friends who believed in me, supported me and without them I would most definitely not be where I am today.

The writing of this thesis also marks the end of my academic career and I look forward to the next chapter in my life. I wish the reader much enjoyment reading this paper.

Tom Rutten
Rijswijk, Februari 2019

CONTENTS

1
INTRODUCTION

1.1. BACKGROUND

Whether it is for the installation of monopiles, for trenching cables or to mine sand for land reclamation: lots of offshore projects require excavation works. While excavating soil either sand, clay or rock is encountered. The distinction between sand and clay is often done based on the grain size: soil with particle diameters of less than 0.002mm is referred to as clay, while soil with particle diameters larger than 0.06mm is called sand. Rock is defined as a collection of minerals with chemically bonded particles and can reach from stiff clay to very hard basalt. As described in **Forster, S.W.** [1991], rock consists of a composition of several mineral types: naturally occurring elements such as sulfur and graphite, a combination of metallic elements and sulfur (sulfides), combinations of metal and oxygen (oxides), naturally occurring halides such as rock salt and fluoride, carbonate containing minerals (carbonates), compositions including phosphate (phosphates), minerals including sulfate radical (sulfates) and the largest group of minerals are the silicates such as quartz and feldspar. Rock can also be classified based on the conditions under which the rock is formed. Igneous rock is formed by the hardening of high temperature molten material such as magma. Sedimentary rock is formed by material which is deposited by wind and water, while metamorphic rock is formed by a modification of existing rock by the application of heat or pressure within the earth.

Excavation work in the dredging industry is done with cutter heads. Figure 1.1 shows two types of cutter heads and a variety of teeth, each designed for specific soil characteristics. For excavating rock either pick points or chisels are most commonly used. Wear and tear of the teeth usually happens at a high rate, so the teeth need to be interchangeable.

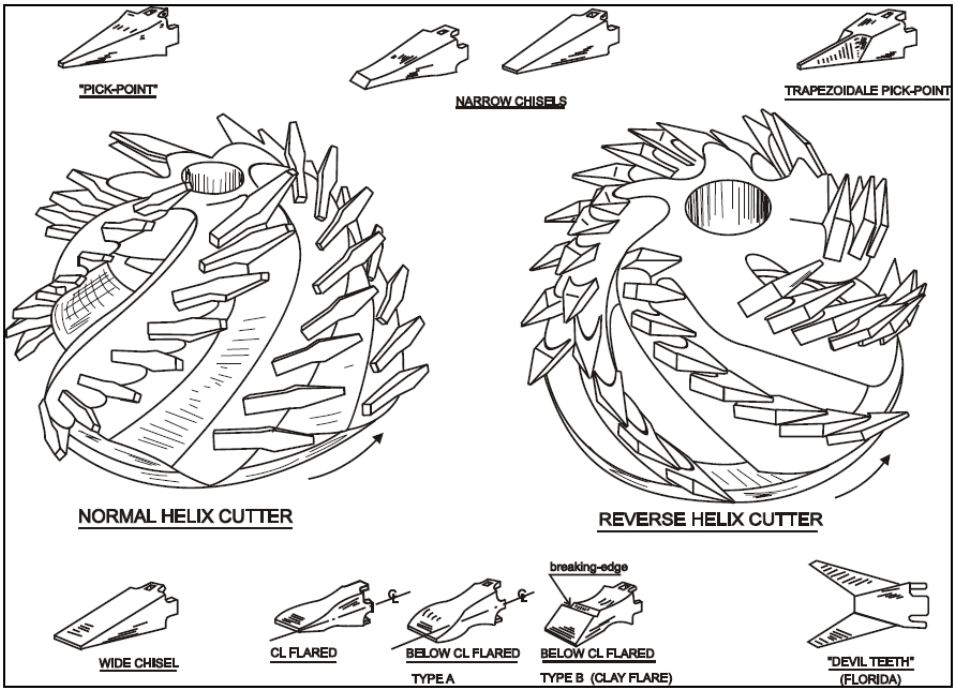

Figure 1.1: Equipment for cutting soil from Miedema (2014)

When rock is being cut, the existence of fractures in the rock mass, determines if the cutter will cut intact rock or break out rock blocks (**Vlasblom, W.J.** [2007]). If intact rock is being cut, the dredgebility depends on the strength (compressive and tensile), deformation properties and petrography (mineralogical proposition). While with the breaking out of rock blocks, the fracture frequency and the weathering is more important than the strength.

According to **Miedema, S.A.** [2014], six flow type mechanisms are distinguished in the rock cutting process: the curling type, flow type, tear type, shear type, chip type and the crushed type. The curling, flow and tear type might occur while cutting clay, the shear type while cutting sand, while the crushed and chip type might occur when cutting rock or stone (figure 1.2). The crushed type occurs when a thin layer of rock is scraped like in oil and gas drilling. Similar to the shear type, only the first layer of rock material has to be crushed. Since this process is assumed to be brittle (shear), the forces are peak forces. The chip type occurs when a thicker layer of rock is cut. This flow mechanism is based on the assumption of tensile failure.

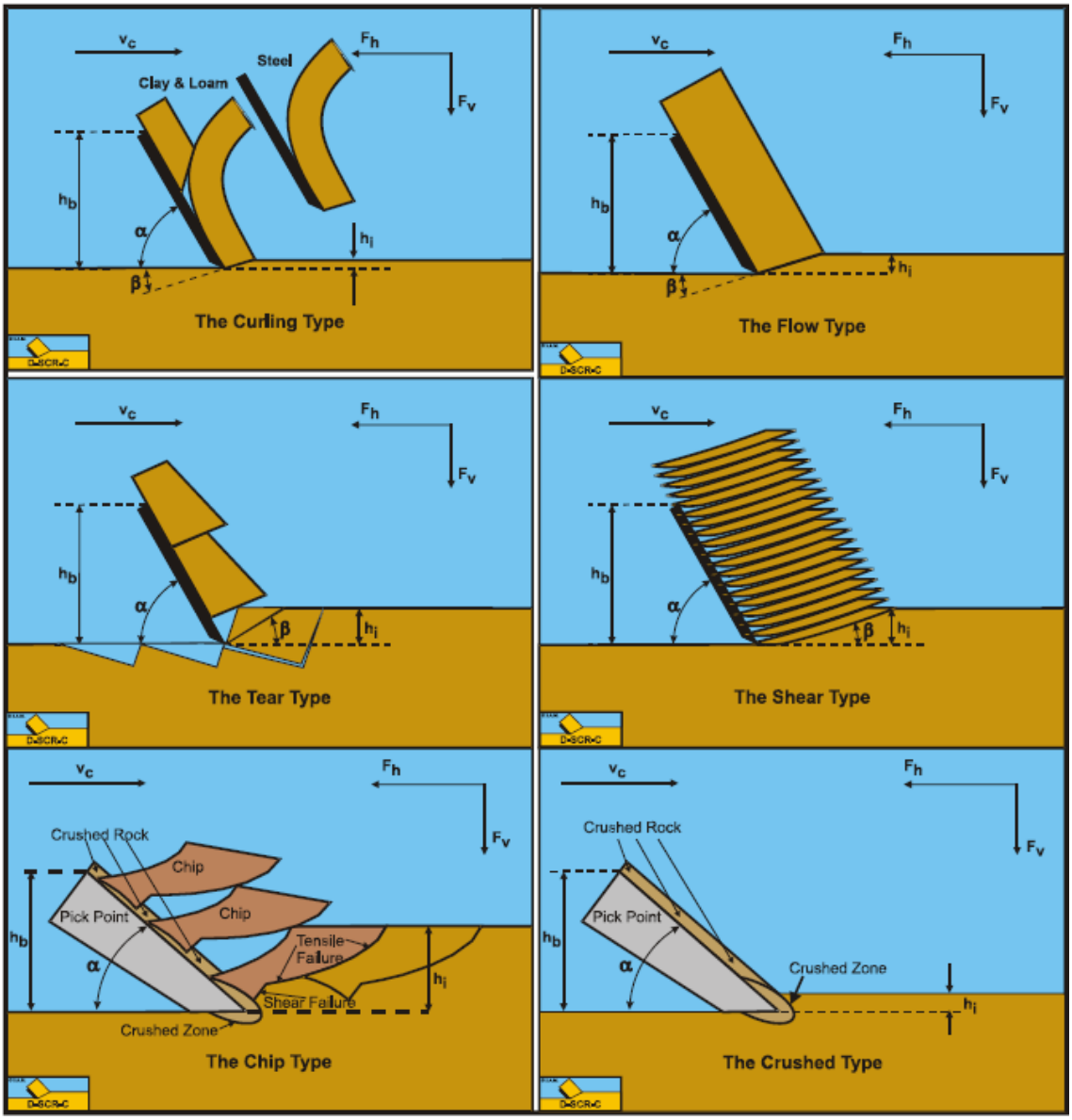

Figure 1.2: Flow type mechanisms in the soil cutting process from Miedema (2014)

1.2. RESEARCH OBJECTIVES

Several models exist to calculate and simulate the cutting of sand and clay. For rock cutting less models are available and the accuracy of the existing models can be improved. According to **Helmons, R.** [2017], one should be careful when applying rock cutting force calculation models. The brittle force calculation models are only able to predict the peak value of the cutting force, not the mean force. Another limitation is the fact that the force calculation models approach the cutting process as a 2D problem, while it is 3D in reality. As a consequence the cut out material can only flow along the cutting tool, while in practice the material will also move sidewards. It is also assumed that the relationship between the cutting force and depth is linear, which may be sufficient for a small cutting depth. However, for larger cutting depth a non-linear relationship might be more accurate. Furthermore, all models are based on the linear cutting process, while in the dredging industry mostly rotary cutting equipment is used. More research on the rock cutting process is necessary to thoroughly understand all occurring phenomena and improve the existing calculating and simulating models which help optimizing the designs and procedures to increase the efficiency of the excavation work.

This research describes the linear cutting experiments with a pick point conducted on sandstone samples. While increasing the cutting depth and using a variety of cutting angles, the existing cutting force prediction models are validated. Furthermore, in literature it is assumed that the cutting depth and cutting force are related linearly. The validity of this claim will be investigated. The experiments filmed to provide more insight in the failure behaviour of the rock samples. Also the chips who are cut out during the experiment will be collected to relate the chip sizes back to the occurring types of failure. The main objectives of this research are:

- Determine the characteristics of the rock samples by conducting laboratory experiments and use these to calculate the remaining relevant rock properties.
- Predict the (peak) cutting forces with use of the existing prediction models.
- Conduct linear cutting experiments to validate the (peak) cutting force by comparing the calculations with the actual measured forces. If any large deviations occur, find the reason based on the underlying physics.
- Capture video material of the experiments for more insights in the failure behaviour of the rock samples.
- Collect the chips to investigate the sizes and relate this back to the type of failure mechanism.
- Validate the linear relationship between cutting depth and force.

The research is conducted in corporation with a sub-group of the China Communication Construction Company (CCCC) Ltd.: the CCCC National Engineer Research Center of Dredging Technology and Equipment Co.,Ltd. The CCCC has executed many project worldwide including but not limited to the Hong Kong international airport land reclemation project, the Panama canal colon port project and the Bronka channel project in Russia. The experiments described in this research are conducted in the test facility of the National Engineer Research Center of Dredging Technology and Equipment located in the Pudong New Area in Shanghai.

1.3. OUTLINE OF THE REPORT

Chapter 2 is a description of the preliminary research that is conducted to support the rock cutting experiments. The experimental layout and characteristics of the rock samples are elaborated upon. Also the experimental procedure and planning are discussed. Then several cutting force prediction models are explained and derived in chapter 3. Subsequently, the rock - and cutting characteristics are substituted in these models to predict the forces. Next in chapter 4 the calibration of the pressure sensor and one set of experiments is described in detail. The remaining experiments are all included in the appendices. Finally the models are compared with the cutting forces during the experiments and two expansions are proposed. This report ends with conclusions and recommendations.

2
RESEARCH ORIENTATION

This chapter is a description of the preliminary research that is conducted to support the linear cutting experiments. The experimental layout and characteristics of the rock samples are elaborated upon. This information is later used in the report to predict the cutting forces.

2.1. OVERVIEW OF THE SETUP USED FOR THE LINEAR CUTTING EXPERIMENTS

The experiments conducted for this research consist of the linear cutting of sandstone samples with use of a pick point. A variety of cutting depths and angles are used while controlling the cutting velocity to a virtually constant value. Although it seems contradictory for the purpose of dredging, the experiments are conducted without water. Since the cutting is carried out at a limited velocity and in a linear direction, there would be no forming of voids. Therefore cavitation will not play a role. Secondly, the limited water depth would not cause hyperbaric conditions. So the addition of water would not yield extra data, but would increase the difficulty of the experiments tremendously. During the experiments the cutting forces and production are measured. From these measurements the forces can be plotted against the cutting depths and angles, which provides insights in the accuracy of the prediction models and in the assumption that the relationship between the cutting force and depth is linear. The experiments will be recorded on video for further analysis.

2.1.1. CUTTING TOOL

A pick point is used as a cutting tool for the experiments. This pick point was used in operations and is adjusted for the experiments. The tip is sharpened for a cleaner cut and to get a precise measurement of the pick point angle. Figure 2.1 shows some detailed pictures of the cutting tool (more in appendix 5.2). The pick point is mounted to a pressure sensor on an adjustable arm to control the cutting depth and cutting angle.

(a) Pressure sensor mounted on transition piece (b) Pick point mounted on pressure sensor

Figure 2.1: Mounted pick point to the pressure sensor: side - and front view

A 3D model of the pick point made with in SOLIDWORKS is attached in appendix 5.2. In figure 2.2 the pick point is schematized and the relevant pick point properties are listed in table 2.1.

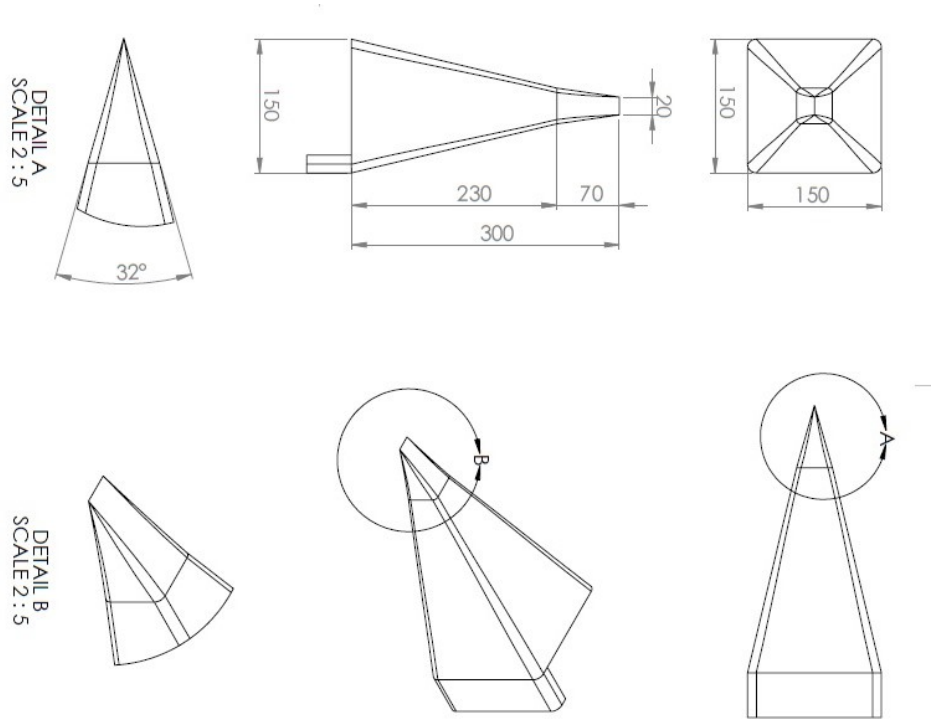

Figure 2.2: Detailed drawing of the pick point used for the cutting experiments

Table 2.1: Properties of the pick point used for the cutting experiments

Symbol	Desciption	Value	Unit
α_p	Pick point angle	16	°
w_p	Pick point width	20	mm
L_p	Pick point length	300	mm
L_t	Pick point tip length	70	mm

2.1.2. PLATFORM

The adjustable arm is connected to a platform which drives on a track over a concrete structure that can be used as a water flume. The flume measures roughly 100m in length, 10m in width with a depth of 3m. During the experiments conducted for this research, the flume was not filled with water. The adjustable arm is controlled by an operator who is positioned in a control room on top of the platform. A camera is positioned with a clear view on the pick point which is displayed on screens on the platform, so the operator can keep an eye on the cutting process.

Figure 2.3: Movable platform, as seen from the water flume

(a) Position of engineer controlling the adjustable arm(1)

(b) Position of engineer controlling the adjustable arm(2)

Figure 2.4: Controls of the engineering for operating the movable platform

2.1.3. CONTROL ROOM

The control room is the heart of this particular building on the test facility. This is the place where the main power switches for all test setups are located and also the controls for the water supply are positioned here. During the experiments the velocity of the moving platform is controlled from this room. The operator has a direct view on the pick point since the screens display from the camera as well.

(a) Control room as seen from the water flume

(b) View from control room

Figure 2.5: Location of the control room and the point of view from control room operator

2.1.4. SAMPLE CONTAINER

The rock samples are mounted to a concrete transition piece connected to the concrete floor of the test facility. Since the floor is covered with a thick layer of sand, a hole is dug so the sample container can be connected to the concrete floor. The rock sample is mounted on the container with clamps.

(a) Sample container mounting piece

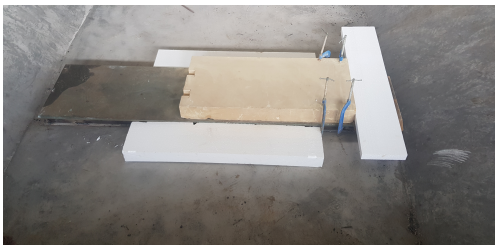

(b) Rock sample mounted on container

Figure 2.6: The sample container used to mount the rock sample to the steel beam

2.1.5. PRESSURE SENSOR

To measure the forces during the cutting process a pressure sensor is used (KD43032K from YZKDS). The pressure sensor measures the output in microvolt (uV) in 200Hz (1/0.005 sec) in x-, y-, and z-direction. The pressure sensor has a range from 0-3200kg. It is connected to a digital dynamic strain meter (DS-50A, from Tokyo Sokki Kenkyujo Co,. Ltd.) and a laptop. With use of Waveform display software (WF-7630) the output from the pressure sensor can be displayed in a time-microvolt graph. To calculate the force from the microvolt (uV) output, calibration tables are used, which were supplied by the sensor manufacturer. The calibration process is described in section 3.1.

(a) Pressure sensor YZKDS KD43032K

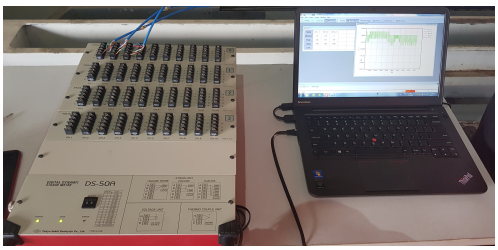

(b) Dynamic strain meter DS-50A

Figure 2.7: The devices used to measure the cutting forces

2.2. STUDY ON THE ROCK SAMPLES TO DETERMINE THE RELEVANT ROCK PROPERTIES

The sandstone rock samples are supplied from a quarry in the Yunnan province of China by the Yunnan Shihui Stone Co., Ltd. A test report by the Yunnan Institute of Product Quality Supervision & Inspection shows the general properties of the samples (appendix 5.2). A translated summary of the properties is presented in table 2.2. Laboratory experiments are conducted to determine the other relevant rock properties.

Table 2.2: Translated summary of general properties of rock samples

#	Property	Unit	Requirement	Tested value
1	Density	g/cm^3	$\geqslant$ 2.00	2.34
2	Water content	%	$\leqslant$ 8.00	2.80
3	Compressive strength (dry)	MPa	$\geqslant$ 12.60	36.00
	Compressive strength (saturated)	MPa	$\geqslant$ 12.60	49.00
4	Bending resistance (dry)	MPa	$\geqslant$ 2.40	5.40
	Bending resistance (saturated)	MPa	$\geqslant$ 2.40	3.90
5	Water resistance	$1/cm^3$	$\geqslant$ 2.00	10.00
6	Radionuclide limit	I_{Ra}	-	0.31
	Radionuclide limit	I_y	-	1.07

Figure 2.8 shows a picture of the rock samples. A total of 9 rock samples were used for these laboratory experiments. From each sample a small stroke was cut out by the supplier. These are used for the laboratory experiments to determine the rock properties for every sample. The approximated size of the rock plates is 210x53x12cm (LxBxH). Since the sizes of the samples is limited by the length of the pit in the floor of the facility, the rock plates are cut in half. So the size of the rock samples used for the experiments are approximately 105x53x12cm (LxBxH).

Figure 2.8: The first batch of sandstone samples used for the cutting experiments

To get the precise properties of the rock samples several laboratory experiments are conducted at the department of geotechnical engineering of the Tongji University in Shanghai. Small cylindrical samples were cut out of the small strokes. For the experiments to determine the compressive strength samples of 0.11m length were used, while for the determination of the tensile strength a length of 0.055m was required. Table 2.3 gives an overview of the dimensions of the samples:

Table 2.3: Dimensions laboratory test samples

Description	Symbol	Amount	Unit
Length UCS sample	L_U	0.11	m
Length BTS sample	L_B	0.055	m
Diameter	D	0.055	m
Area	A	0.0024	m^2

2.2.1. UNIAXIAL COMPRESSION TEST

A cylindrical rock sample is axially loaded until failure, while measuring the force and deformation. From these measurements the stress-strain curve can be constructed (figure 2.9a) and several properties can be determined.

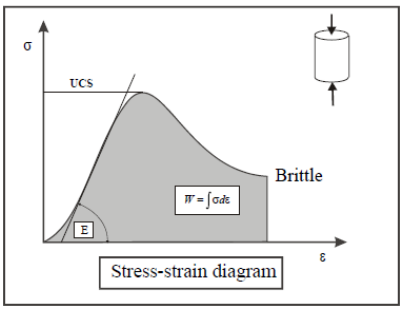

(a) Stress-strain diagram from Vlasblom (2007)

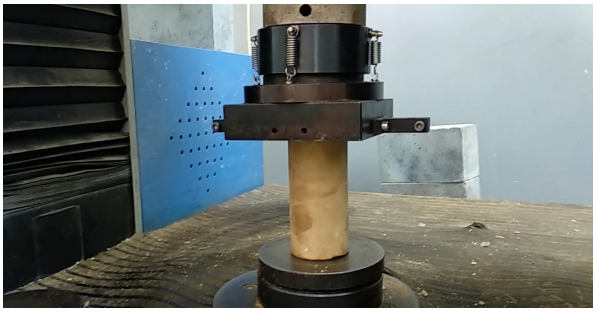

(b) UCS test at Tongji University

Figure 2.9: Stress-strain diagram and UCS test performed at Tongji University

Each of the 9 samples were tested 3 times for the compressive strength. The samples are numbered 1 to 9, while subscript 1, 2 or 3 counts the test per sample. The maximum forces that occurred during the uniaxial compression test (F_U) are presented in table 2.4.

UNCONFINED COMPRESSIVE STRENGTH

The compressive strength is the capacity of the material to withstand a reduction in size due to loads. The determination of the Unconfined Compressive Strength (UCS) is done by a uniaxial compression test. The UCS [MPa] is defined as the ratio between the compressive force at failure (F_U) and the cross sectional area of the cylindrical rock sample (A) (equation 2.1).

$$UCS = \frac{F_U}{A} \tag{2.1}$$

Applying equation 2.1 to the force output from the UCS test gives the stress-strain diagrams (figures in appendix 5.2). The UCS value of the rock samples is the maximum stress in the stress-strain diagram. To approximate the final UCS value the average (with subscript av) of the 3 measurements is used (table 2.4).

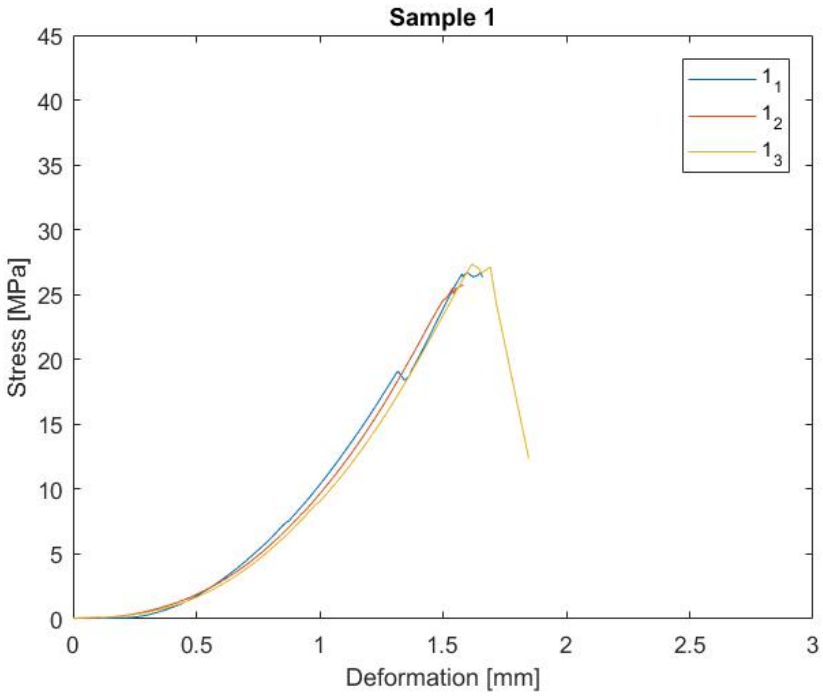

Figure 2.10: Stress - deformation diagram to determine the UCS value of rock sample 1

YOUNG'S MODULUS

The Young's Modulus (E) (or elastic strain) is a measure of stiffness which can be determined with use of the unconfined compressive strength test. The Young's Modulus is defined as the ratio of uniaxial stress over uniaxial strain [MPa]. In this case, stress is defined as the ratio of force F over area A devided by the ratio of ΔL_U devided by L_U, where ΔL_U is the change in size due to the application of the force. The Young's Modulus per sample is presented in table 2.4.

$$E = \frac{F_U / A}{\Delta L_U / L_U} \tag{2.2}$$

2.2.2. BRAZILIAN SPLIT TEST

In the Brazilian Split Test a cylindrical rock sample is loaded in radial direction (figure 2.11a). This test is most commonly used to determine the Brazilian Tensile Strength (BTS). On each sample 3 split tests were conducted. The samples are again numbered with 1 until 9, while the subscript 1-3 represent the test number.

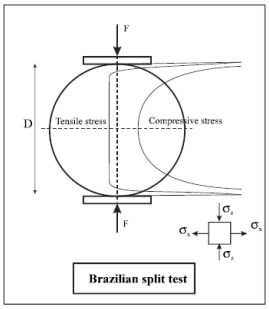

(a) Brazilian split test from Vlasblom (2007)

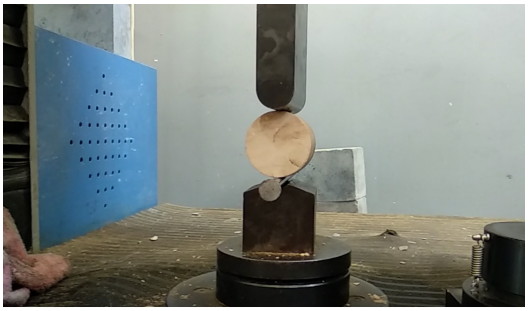

(b) Brazilian split test at Tongji University

Figure 2.11: Brazilian split test to determine the BTS value of rock samples

BRAZILIAN TENSILE STRENGTH

The tensile strength (σ_t) of a material is the capacity to withstand an elongating load. The Brazilian Tensile Strength (BTS) is the maximum tensile stress a sample can withstand. The tensile stress [MPa] in the centre of the cross sectional is calculated with equation 2.3 , where L_B is the length of the sample, D the diameter and F_B the compressive force. The stress-strain diagrams are attached in appendix 5.2, the results of the split test are presented in table 2.4.

$$BTS = \frac{2F_B}{\pi D L_B} \tag{2.3}$$

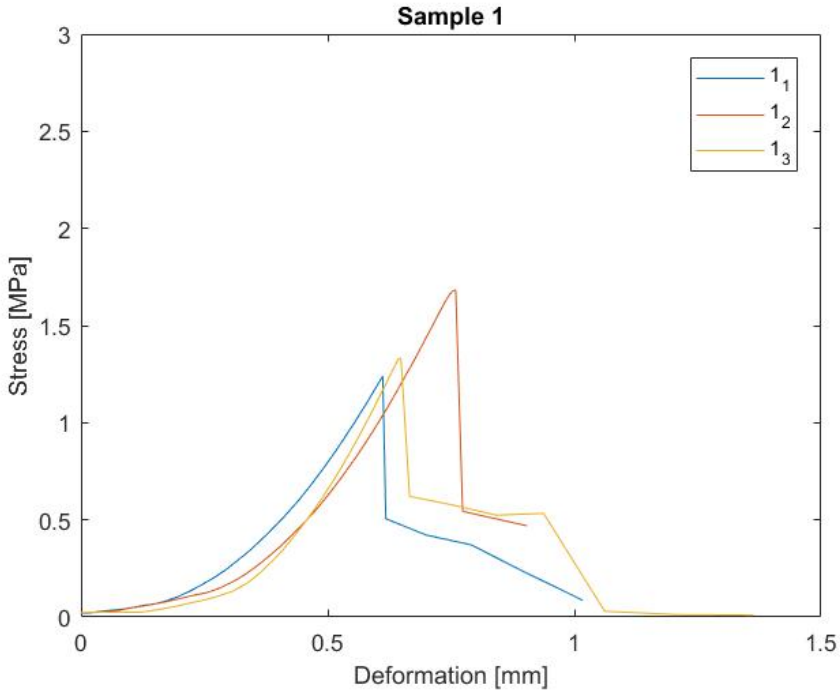

Figure 2.12: Stress - deformation diagram to determine the BTS value of rock sample 1

2.2.3. TILTING TABLE TEST

An easy test to determine the remaining rock properties is the tilting test. In a tilting test the samples are placed on a table. The table is then tilted slowly until the sample slides off (figure 2.13). The tilting tests are conducted according to the United States Bureau of Reclamation procedure for determining the (static) angle of basic friction using a tilting table test (**USBR** [2009]).

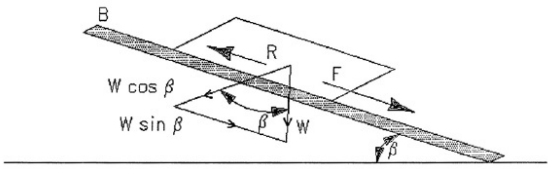

(a) Tilting table test from USBR 6258 (2009)

(b) Tilting table test to determine the basic friction angle

Figure 2.13: The tilting table test as performed to determine the basic friction angle

INTERNAL FRICTION ANGLE

The internal friction angle (ϕ) delivers an internal resistance force against the movement due to shear stresses between the particles of a material. These movements can be due to external changes in temperature and deformations. Where the internal friction angle refers to the peak resistance, the residual friction angle is a more conservative value. With the absence of a shear test or triaxial stress test apparatus it is a save estimation of the internal friction angle. If the tilting table test is conducted in an adjusted manner it can be used to determine the residual friction angle. Instead of using a table and a rock sample, the test is conducted with 2 samples on top of each other where the bottom sample acts as the tilting table. The internal friction angle of the material can be determined by the force equilibrium, which proves that the tilting angle of the table (or sample) (β) is equal to the basic friction angle of the material (ϕ).

$$F = R \rightarrow \qquad W \cdot sin(\beta) = W \cdot cos(\beta) \cdot tan(\phi) \rightarrow \qquad tan(\beta) = tan(\phi) \rightarrow \qquad \phi = \beta \tag{2.4}$$

EXTERNAL FRICTION ANGLE

The external friction angle (δ) determines the friction between the soil sample and a different material. The external friction angle is related to the internal friction angle and is most commonly approximated by:

$$\delta = \frac{2}{3}\phi \tag{2.5}$$

COHESION

Cohesion (c) is a component of the shear strength of a material. Also this characteristic is measured in force per unit area [MPa]. In natural soils, cohesion results from electrostatic bonds between particles. Cohesion is also responsible for the finite value of tensile strength in both soils and rocks (**Blasio, F.V. de** [2011]). The determination of the cohesion is done with use of the Mohr-Coulomb theory. In the Mohr-Coulomb theory an infinitesimal element of soil is considered. The principal stresses (vertical and horizontal, σ_v and σ_h) are acting on this soil element. By deriving the equilibrium of forces in horizontal and vertical direction and applying rules from trigonometry, the Mohr-Coulomb failure criterion is obtained (equation 2.6). From the Mohr circle (figure 2.14) it is noticed that the initial angle (α_i) of the plane considered (in the infinitesimal soil element) appears as an angle of $2 \cdot \alpha_i$ in the Mohr circle.

$$\tau = c + \sigma \tan(\phi) \tag{2.6}$$

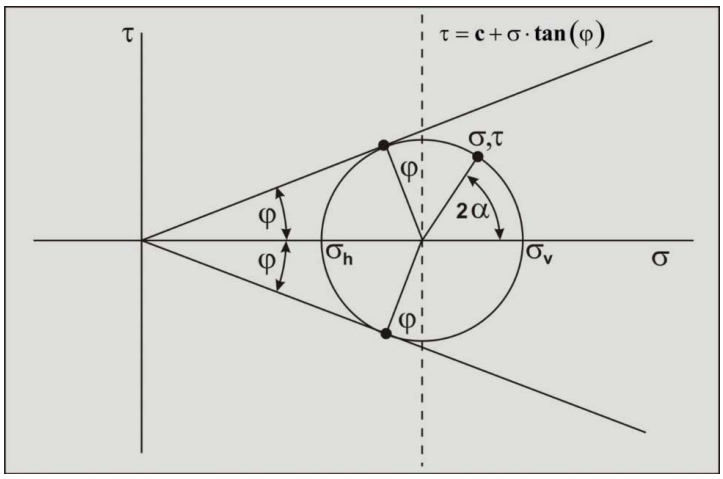

Figure 2.14: Mohr circle for cohesion less soil from Miedema (2014)

With use of the Mohr circle an expression for the cohesion can be derived with respect to the angle of internal friction:

$$c = \frac{UCS}{2} \cdot \frac{1 - sin(\phi)}{cos(\phi)} \tag{2.7}$$

2.2.4. DENSITY TEST

The density (ρ), or volumetric mass density, is a measure of mass per unit volume [kg/m^3]. Density of homogeneous materials can be calculated by measuring the mass and divide this by the volume. For heterogeneous materials, the density can vary between different regions in the sample. In that case the density can be approximated with equation 2.8. Where dV is an elementary volume at position r. Note that in these density calculations the pressure and temperature is not included since their influence on the density of rock samples is negligible.

$$m = \int_V \rho(\vec{r}) dV \tag{2.8}$$

2.2.5. BRITTLENESS

The type of rock failure is partly determined by the brittleness (or ductility number), but also confining pressure and temperature play a role. Although brittleness is one of the most important properties of rocks, there is no universally accepted concept or measuring method. In literature, brittleness is often defined as the lack of ductility.

According to **Hucka, V. and Das, B.** [1974], samples with higher brittleness tend to have: low values of elongation, fracture failure, formation of fines, higher ratio of compressive to tensile strength, high resilience, high angle of internal friction and formation of cracks in indentation.

A method to determine the brittleness based on the ductility number is described in **Miedema, S.A.** [2014]. This method uses the ratio of UCS over BTS equation 2.9. If this ratio is below 9, ductile failure will occur. While a ratio above 15 will lead to brittle failure.

$$B = \frac{UCS}{BTS} \tag{2.9}$$

2.2.6. RESULTS OF LABORATORY TESTS

Table 2.4 contains the values of the rock properties for all 9 samples. The samples were ordered in 2 batches (1-4 and 5-9) and therefore might be from a different area of the quarry. Since the pressure sensor has a limited capacity, it is chosen to conduct the experiments for this research on samples 5-9. The samples 1-4 will be used by CCCC for other research.

Table 2.4: Laboratory test results: rock properties

Sample nr	F_U kN	F_B kN	UCS MPa	BTS MPa	B [-]	E GPa	C MPa	ϕ °	δ °	ρ kg/m^3
Sample 1_1	63.485	5.890	26.721	1.239	21.567	1.771	8.349	26	17	2297.639
Sample 1_2	61.238	8.003	25.775	1.684	15.306	1.791	8.053	26	17	2304.457
Sample 1_3	64.976	6.328	27.349	1.331	20.548	1.628	8.545	26	17	2297.639
Sample 1_{av}	**63.224**	**6.740**	**26.611**	**1.412**	**19.140**	**1.730**	**8.316**	**26**	**17**	**2299.911**
Sample 2_1	76.425	8.608	32.168	1.811	17.763	2.080	9.664	28	19	2277.185
Sample 2_2	105.030	10.410	44.208	2.191	20.177	3.648	14.082	25	17	2263.549
Sample 2_3	72.340	8.651	30.448	1.821	16.720	2.231	9.329	27	18	2270.367
Sample 2_{av}	**84.559**	**9.809**	**35.592**	**2.064**	**18.220**	**2.653**	**11.025**	**27**	**18**	**2270.367**
Sample 3_1	60.841	7.334	25.608	1.543	16.596	1.322	8.001	26	17	2263.549
Sample 3_2	65.521	7.073	27.578	1.488	18.534	1.658	8.616	26	17	2270.367
Sample 3_3	61.121	12.509	25.726	2.633	9.771	1.524	7.883	27	18	2263.549
Sample 3_{av}	**62.413**	**8.972**	**26.270**	**1.888**	**14.967**	**1.501**	**8.170**	**26**	**17**	**2265.822**
Sample 4_1	30.998	11.965	13.047	2.518	5.181	0.738	4.156	25	17	2331.728
Sample 4_2	46.660	5.994	19.639	1.261	15.574	0.529	6.017	27	18	2331.728
Sample 4_3	30.304	6.796	12.755	1.430	8.920	0.353	3.985	26	17	2311.275
Sample 4_{av}	**35.987**	**8.972**	**15.147**	**1.737**	**9.892**	**0.540**	**4.719**	**26**	**17**	**2324.910**
Sample 5_1	39.346	6.813	16.560	1.434	11.548	0.885	4.781	30	20	2323.750
Sample 5_2	37.852	6.683	15.932	1.406	11.331	0.458	4.599	30	20	2257.585
Sample 5_3	57.190	10.396	24.072	2.188	11.002	1.798	7.080	29	20	2249.214
Sample 5_{av}	**44.796**	**8.252**	**18.855**	**1.676**	**11.294**	**1.047**	**5.489**	**30**	**20**	**2276.850**
Sample 6_1	41.302	4.750	17.384	1.000	17.384	2.416	4.918	31	21	2297.443
Sample 6_2	44.380	5.204	18.680	1.095	17.059	1.705	5.392	30	20	2274.978
Sample 6_3	34.940	6.231	14.706	1.311	11.217	1.146	4.245	30	20	2311.473
Sample 6_{av}	**40.206**	**5.395**	**16.923**	**1.135**	**15.220**	**1.756**	**4.885**	**30**	**20**	**2294.631**
Sample 7_1	69.245	8.501	29.146	1.789	16.292	1.477	8.414	30	20	2381.624
Sample 7_2	41.849	7.124	17.615	1.499	11.751	0.443	4.983	31	21	2379.334
Sample 7_3	34.625	8.437	14.574	1.776	8.206	0.863	4.123	31	21	2348.027
Sample 7_{av}	**48.573**	**8.021**	**20.445**	**1.688**	**12.083**	**0.928**	**5.784**	**31**	**21**	**2369.662**
Sample 8_1	46.082	6.074	19.396	1.278	15.177	0.986	5.599	30	20	2313.182
Sample 8_2	36.167	6.231	15.223	1.311	11.612	1.413	4.306	31	21	2305.987
Sample 8_3	43.521	5.706	18.318	1.201	15.252	0.828	5.288	30	21	2288.000
Sample 8_{av}	**41.923**	**6.004**	**17.646**	**1.264**	**14.014**	**1.076**	**5.094**	**30**	**21**	**2302.390**
Sample 9_1	37.414	7.063	15.748	1.487	10.590	1.459	4.825	27	18	2318.431
Sample 9_2	47.763	8.360	20.104	1.760	11.423	0.940	6.040	28	19	2308.081
Sample 9_3	48.007	6.886	20.207	1.449	13.945	1.236	5.833	30	20	2311.531
Sample 9_{av}	**44.395**	**7.437**	**18.686**	**1.565**	**11.986**	**1.211**	**5.614**	**28**	**19**	**2312.681**

2.3. STUDY ON THE CUTTING FORCE PREDICTION MODELS

The failure of rock can occur in several manners depending on the rock properties, confining pressure (for example the rock cutting process in deep water) and cutting depth. Cutting force prediction models have been developed for each type of failure. An important aspect to consider is the fact that these models are 2D. Each model assumes a cutting area, calculated by multiplying the depth of the cut h with the width of the cutting tool w_p. This is multiplied with the rock property that delivers the resistance force to the assumed type of failure. The output of these models is the cutting force in horizontal and vertical direction.

A first assumption made in these models is that the sideways force during cutting is negligible. This seems to be a reasonable assumption for a linear cutting process. Another assumption is that the area of the cut is equal to the depth of the cut multiplied with the width of the cutting tool. One could imagine that the rock pieces that break out during the cutting process can be much wider and deeper than this. This has a huge influence on the cutting forces: a larger the depth and width increases the area quadratically. Finally the models also assume the use of a sharp cutting tool. Especially with small cutting depths the effects of wear and tear of the tool could have its influence on the measured forces.

Rock failure occurs either in a brittle (high brittleness), a brittle-ductile (medium brittleness) or a ductile manner (low brittleness) (figure 2.15a). Brittle failure occurs at relatively low confining pressure and deviatoric stress. As shown in figure 2.15b, pure tensile failure, axial tensile failure and (discrete) shear plane failure are all considered types of brittle failure. In brittle failure the force builds up until a certain limit is exceeded and then the failure occurs. This failure is irreversible. At higher confining pressures during the cutting process, the failure shifts to a more brittle-ductile (or semi brittle) failure with either a shear belt or a shear zone. Even higher confining pressures lead to a ductile failure mode.

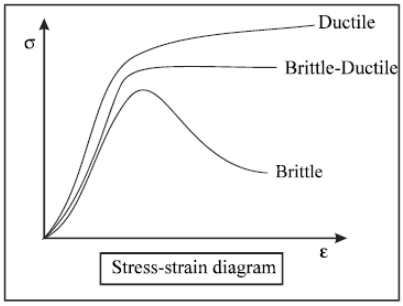

(a) Rock failure modes from Vlasblom (2007)

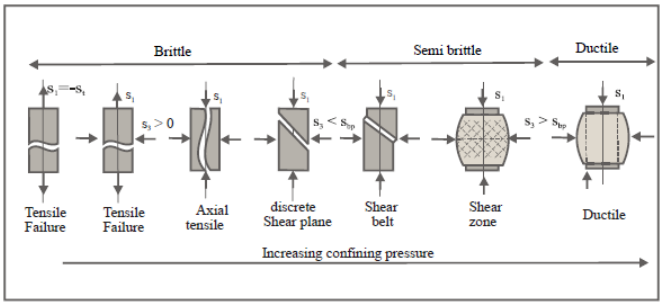

(b) Types of rock failure modes from Vlasblom (2007)

Figure 2.15: The different types of rock failure modes from Vlasblom(2007)

The cutting force prediction models considered in this report assume either a brittle tensile, brittle shear of ductile failure mechanism:

- Brittle tensile: The Evans Model
- Brittle shear : The Nishimatsu Model
- Brittle shear : The Tear Model
- Ductile : The Flow Model

2.3.1. BRITTLE TENSILE - THE EVANS MODEL

The model of **Evans, I.** [1964] assumes failure in a brittle tensile manner. From analysing the cutting of a blunt wedge through a coal sample the geometry of the forces is constructed, as described by **Miedema, S.A.** [2014].

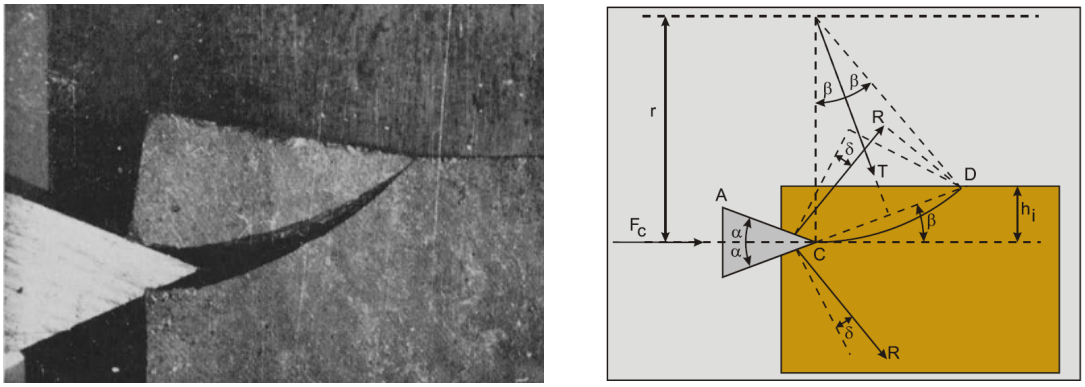

(a) Blunt wedge cutting through coal sample from Evans (1964)

(b) The model of Evans schematized by Miedema (2014)

Figure 2.16: Schematization of the model of Evans from Miedema (2014)

Adjusting the Evans model to include the cutting angle (while cutting horizontally with a constant depth) makes it applicable for the experiments conducted for this research, as shown in figure 2.17. The new geometry is now combined with the derivation of the regular Evans Model.

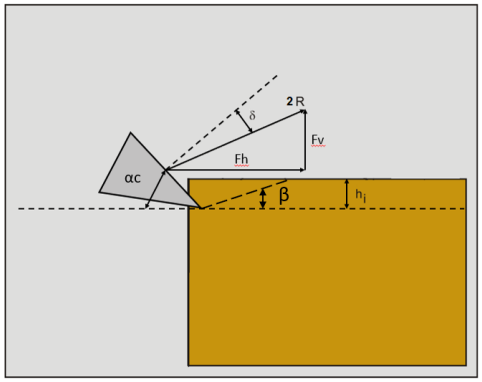

Figure 2.17: Schematized adjusted Evans Model

Since the Evans Model assume failure in a brittle tensile manner, the resistance of the rock (R_R) is assumed to be the area of the cut times the tensile strength. In equation 2.10 h_i represents the depth of the cut, while w represents the width of the pick point.

$$R_R = h_i \cdot w \cdot \sigma_t \tag{2.10}$$

The expression for force R is calculated by taking the moment of R around point D (figure 2.16). Force R acts under angle δ to the surface of the cutting tool, with δ is the external friction angle of the rock sample. The angle of the tool (α) however, is now substituted with the cutting angle (α_c). Which leads to the final expression for force R:

$$R = \frac{R_R}{2 \cdot sin(\beta) \cdot cos(\alpha_c + \beta + \delta)} = \frac{\sigma_t \cdot h_i \cdot w}{2 \cdot sin(\beta) \cdot cos(\alpha_c + \beta + \delta)} \tag{2.11}$$

From force R an expression for the horizontal and vertical cutting force is composed. As seen from figure 2.17 the total force on the top side of the cutting tool is $2R$ instead of R on both the top and bottom (figure 2.16).

This results in a vertical component of the cutting force in the adjusted model of Evans, while in the regular model of Evans the vertical components cancel each other out of the equation.

$$F_h = 2 \cdot R \cdot sin(\alpha_c + \delta) = \frac{\sigma_t \cdot h_i \cdot w}{sin(\beta) \cdot cos(\alpha_c + \beta + \delta)} \cdot sin(\alpha_c + \delta) \tag{2.12}$$

$$F_v = 2 \cdot R \cdot cos(\alpha_c + \delta) = \frac{\sigma_t \cdot h_i \cdot w}{sin(\beta) \cdot cos(\alpha_c + \beta + \delta)} \cdot cos(\alpha_c + \delta) \tag{2.13}$$

In equations 2.12 and 2.13 β represents the shear angle. In literature the shear angle is explained as the the degree of angle that changes at peak frictional force and at the commencement of the experiment. Practically seen this indicates the angle of the shear plane that appears during the experiments.
Shear angle β can be expressed in α_c and δ by applying the principle of minimum energy. This principle, based on the second law of thermodynamics, states that (in a closed system) the internal energy will decrease to a minimum value at equilibrium. The minimum is determined by finding the conditions for which the derivative of the force expressions with respect to β are equal to zero.

$$\frac{dF_h}{d\beta} = 0 \tag{2.14}$$

Resulting in:

$$\beta = \frac{\pi}{4} - \frac{\alpha_c + \delta}{2} \tag{2.15}$$

Substituting this into equations 2.12 and 2.13 gives the final expression for the horizontal and vertical cutting forces:

$$F_h = \sigma_t \cdot h_i \cdot w \cdot \frac{2 \cdot sin(\alpha_c + \delta)}{1 - sin(\alpha_c + \delta)} \tag{2.16}$$

$$F_v = \sigma_t \cdot h_i \cdot w \cdot \frac{2 \cdot cos(\alpha_c + \delta)}{1 - sin(\alpha_c + \delta)} \tag{2.17}$$

However, a quick look at the expression for the shear angle reveals a problem for the applicability of this calculation model, especially for the larger cutting angles. Cutting under an angle of α_c = 70°, while the external friction angle δ = 19-21°, gives $\beta \approx 0$ °. With δ = 21° the shear angle even has a negative sign. Considering figure 2.17 again, this appears to be physically incorrect. The crack will always search for the direction with the least resistance. With these small cutting depths with a maximum of 1.5cm, the crack will always develop upwards instead of parallel to the cut or even pushing downwards through the 10cm thick rock layer.

In terms of cutting forces, a similar problem occurs. When cutting angle α_c approaches 70° the $sin(\alpha_c + \delta)$ = 1, while $cos(\alpha_c + \delta)$ = 0. This results in a horizontal force $F_h = \infty$, while the vertical force F_v = 0. This is, of course, impossible in reality.

To investigate the extend to which this force prediction model is applicable, the maximum cutting forces are plotted over the depth while using a variety of cutting angles (figure 2.18). To keep the other parameters constant, it is chosen to use sample 5 for these calculations. Since the 70° angle gives infinitely large values, this is impossible to plot and therefore not included.

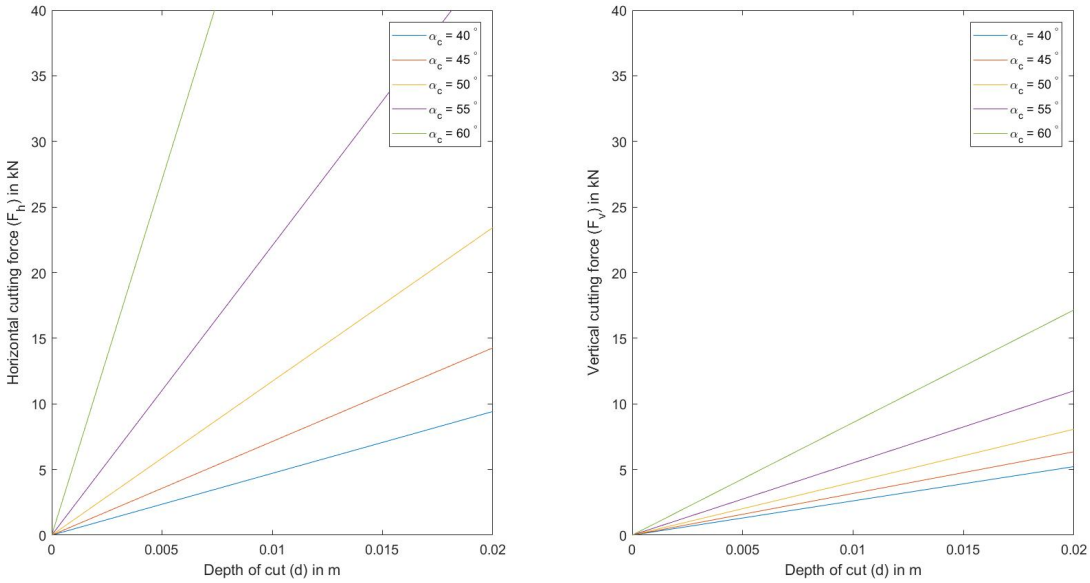

Figure 2.18: Cutting forces over depth using Evans model

Since all parameters are kept constant and only the cutting angle varies, the large spread is completely due to the cutting angle. Even though there might be a configuration (cutting angle and rock characteristics) for which this model incidentally predicts a force in the vicinity of the measured force, one should wonder if this is due to a correct application of the underlying physics or simply a lucky coincidence.

2.3.2. BRITTLE SHEAR - THE NISHIMATSU MODEL

In the cutting force calculation model by **Nishimatsu, Y.** [1971], the failure is assumed to be brittle shear. The model was validated with experiments, where an orthogonal cutting tool was used to cut through 20x300x100 mm samples of sandy tuff (Aoishi) and cement mortar, while measuring the cutting forces. In order to consider the rock cutting process as a two-dimensional problem, it is assumed that the width of the cutting edge is much larger than the depth of the cut. Figure 2.19a illustrates that a crushed zone arises in front of the cutting tool. The deeper the penetration of the tool, the greater the cutting force becomes. If a critical value is exceeded, macroscopic cracks appear. Propagation of these cracks lead to a failure crack and results in a coarse cutting chip. From a schematization described in **Miedema, S.A.** [2014] (figure 2.19b) it is seen that this calculation model needs no adjustment since the cutting geometry is equal to the one used in this research .

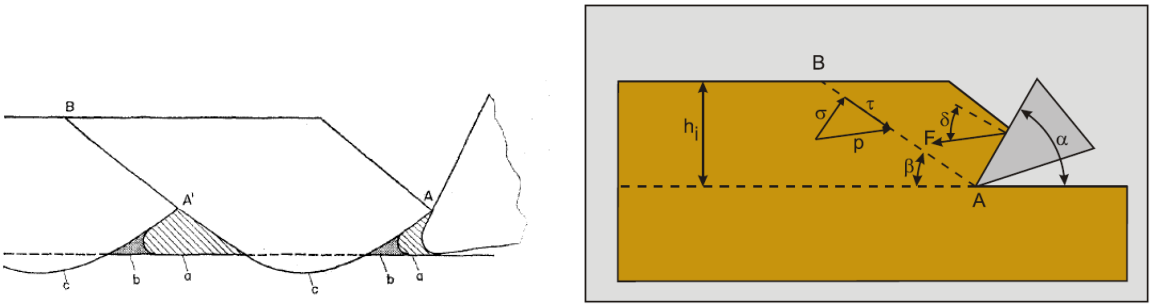

(a) Failure process of rock by Nishimatsu (1971)

(b) Schematization by Miedema (2014)

Figure 2.19: Schematization of the Nishimatsu failure process

Since the Nishimatsu model assumes failure in a brittle shear manner, the normal stress σ_0 and shear stress τ_0 are taken into account and multiplied with the area of the cut (h_i times w). This stress has to be equal to a term including the cutting force F times a stress distribution factor (n) and applying the goniometric rules.

$$\sigma_0 \cdot h_i \cdot w = -(n+1) \cdot sin(\beta) \cdot cos(\alpha+\beta+\delta) \cdot F \tag{2.18}$$

$$\tau_0 \cdot h_i \cdot w = (n+1) \cdot sin(\beta) \cdot sin(\alpha+\beta+\delta) \cdot F \tag{2.19}$$

The expressions found for the normal and shear stress can be substituted into the Mohr-Coulomb failure criterion (equation 2.6). Substituting this into equations 2.18 and 2.19 gives the following expressions for the horizontal and vertical cutting force:

$$F_h = \frac{1}{n+1} \cdot \frac{c \cdot h_i \cdot w \cdot cos(\phi) \cdot sin(\alpha+\delta)}{sin(\beta) \cdot sin(\alpha+\beta+\delta+\phi)} \tag{2.20}$$

$$F_v = \frac{1}{n+1} \cdot \frac{c \cdot h_i \cdot w \cdot cos(\phi) \cdot cos(\alpha+\delta)}{sin(\beta) \cdot sin(\alpha+\beta+\delta+\phi)} \tag{2.21}$$

With use of the principle of minimum energy $\left(\frac{\delta F_h}{\delta \beta} = 0\right)$, β can be expressed in α, δ and ϕ, which can be substituted in formulae 2.20 and 2.21:

$$\beta = \frac{\pi}{2} - \frac{\alpha+\delta+\phi}{2} \tag{2.22}$$

$$F_h = \frac{1}{n+1} \cdot \frac{2 \cdot c \cdot h_i \cdot w \cdot cos(\phi) \cdot sin(\alpha+\delta)}{1+cos(\alpha+\delta+\phi)} \tag{2.23}$$

$$F_v = \frac{1}{n+1} \cdot \frac{2 \cdot c \cdot h_i \cdot w \cdot cos(\phi) \cdot cos(\alpha+\delta)}{1+cos(\alpha+\delta+\phi)} \tag{2.24}$$

Quickly analysing shear angle β for the Nishimatsu model shows reasonable results when the cutting parameters are filled in. Again sample nr 5 is used to keep the rock characteristics constant. For a cutting angle α_c = 40° the shear angle becomes β = 44°. For the largest cutting angle α_c = 70° the shear angle decreases to β = 29°.

Again the values of sample nr 5 are filled into the equations for the horizontal and vertical cutting force. The results show the cutting force over the depth of the cut (figure 2.20). From this figure it is seen that the spread of the results is reasonable. Therefore it seems that the Nishimatsu model is applicable for the cutting geometry used in this research.

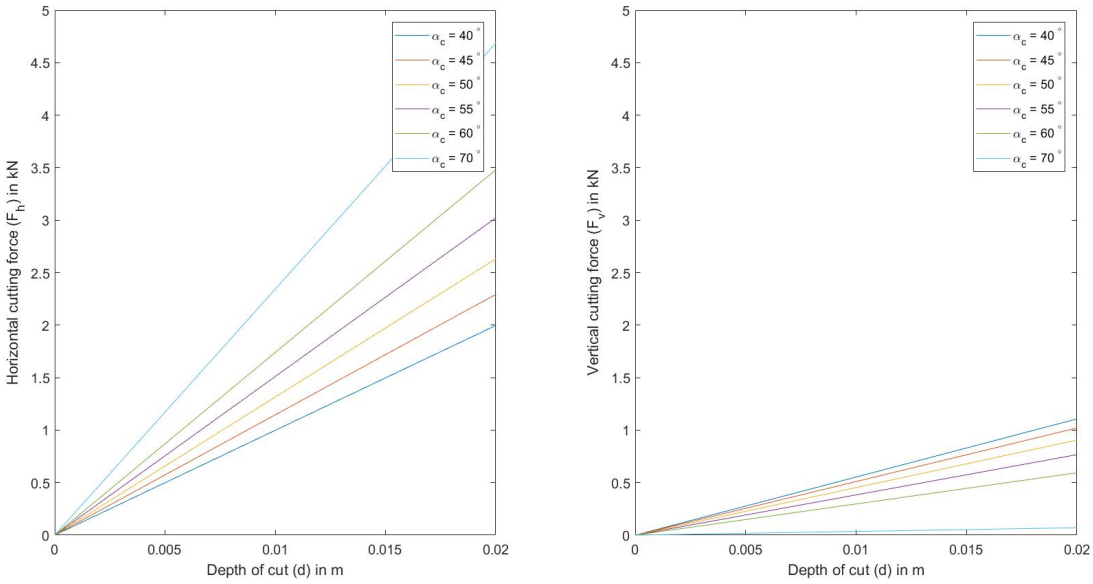

Figure 2.20: Cutting forces over depth using Nishimatsu model

2.3.3. BRITTLE SHEAR - THE TEAR/CHIP MODEL

The Tear/Chip model is based on the assumption that rock failure occurs by tensile rupture. A derivation of this model is made with use of figure 2.21 from **Miedema, S.A.** [2014]. From the cutting geometry in this figure one can observe that this is similar to the one in this research, therefore this cutting model could be applied without adjustments.

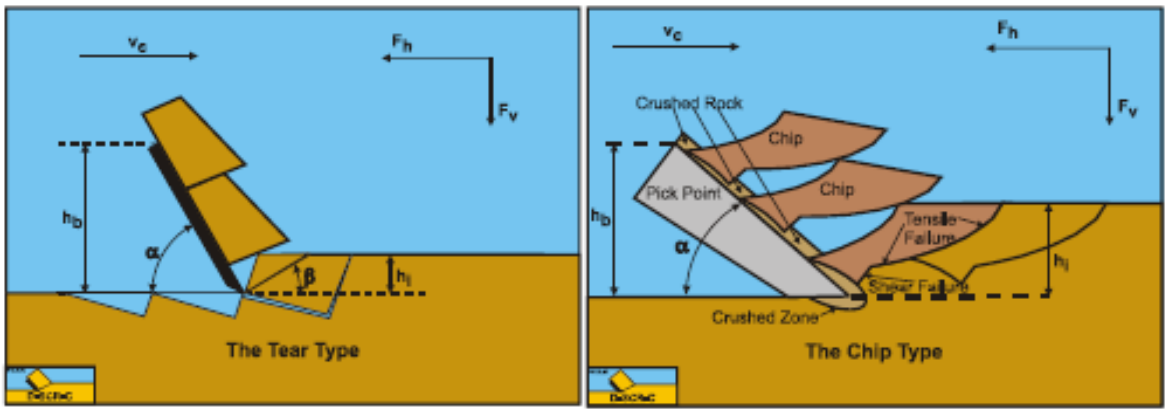

Figure 2.21: Schematization of the Tear and Chip type by Miedema (2014)

Since tensile failure is assumed, the cohesion is taken into account by multiplying this with the area of the cut (depth of the cut h_i times width of the cut w). So first, an expression for the cohesion c is composed with use of figure 2.22a.

$$c = \frac{UCS}{2} \cdot \frac{1 - sin(\phi)}{cos(\phi)} \tag{2.25}$$

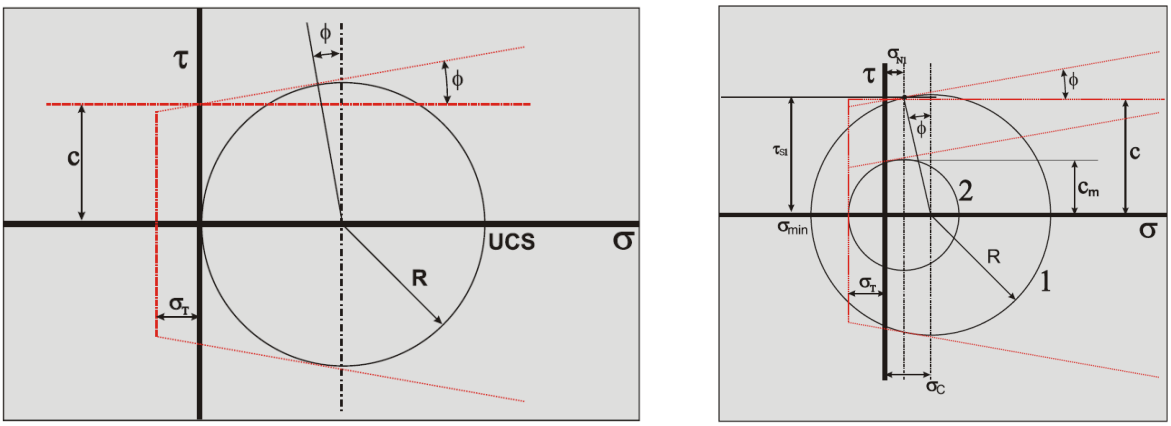

(a) The Mohr circle for the UCS and cohesion

(b) The Mohr circle for the Tear type

Figure 2.22: The Mohr circle for the UCS value and the Tear type from Miedema (2014)

With use of the tensile strength σ_t the mobilized cohesion is constructed. The phenomenon of mobilized cohesion can be explained as the amount of shear resistance developed due to a load in order to resist the deformation.

$$c_m = \frac{\sigma_t}{\left(\frac{sin\left(\frac{\alpha_c+\delta-\phi}{2}\right)}{cos\left(\frac{\alpha_c+\delta+\phi}{2}\right)} - 1\right)\left(\frac{1-sin(\phi)}{cos(\phi)}\right)} \tag{2.26}$$

The shear angle and force expressions for the tear type failure mechanism become:

$$\beta = \frac{\pi}{2} - \frac{\frac{\pi}{4} + \alpha_c + \delta + \phi}{2} \tag{2.27}$$

$$F_h = \frac{2 \cdot c_m \cdot h_i \cdot w \cdot cos(\phi) \cdot sin(\alpha_c + \delta)}{1 + cos(\alpha_c + \delta + \phi)} \tag{2.28}$$

$$F_v = \frac{2 \cdot c_m \cdot h_i \cdot w \cdot cos(\phi) \cdot cos(\alpha_c + \delta)}{1 + cos(\alpha_c + \delta + \phi)} \tag{2.29}$$

Analysing the expressions for the mobilized cohesion c_m and the shear angle β reveal questionable results for larger cutting angles.

If the rock characteristics of sample nr 5 are substituted in the expression for the mobilized cohesion, the term $\frac{sin(\frac{\alpha_c+\delta-\phi}{2})}{cos(\frac{\alpha_c+\delta+\phi}{2})} - 1$ goes to zero for cutting angle $\alpha_c = 70°$, external friction angle $\delta = 20°$ and internal friction angle $\phi = 30°$. This leads to an infinitely large value for the mobilized cohesion.

Similar problems occur for the shear angle β when the rock characteristics are filed into the equation. For cutting angle $\alpha_c = 70°$ the shear angle $\beta = 7.5°$. This low shear angle would imply a very long shear length through the sample, which increases the cutting forces drastically.

To check the applicability of this model, the forces are plotted over the cutting depth again. Like the Evans model, the cutting angle $\alpha_c = 70°$ is kept out since it is impossible to plot infinitely large values.

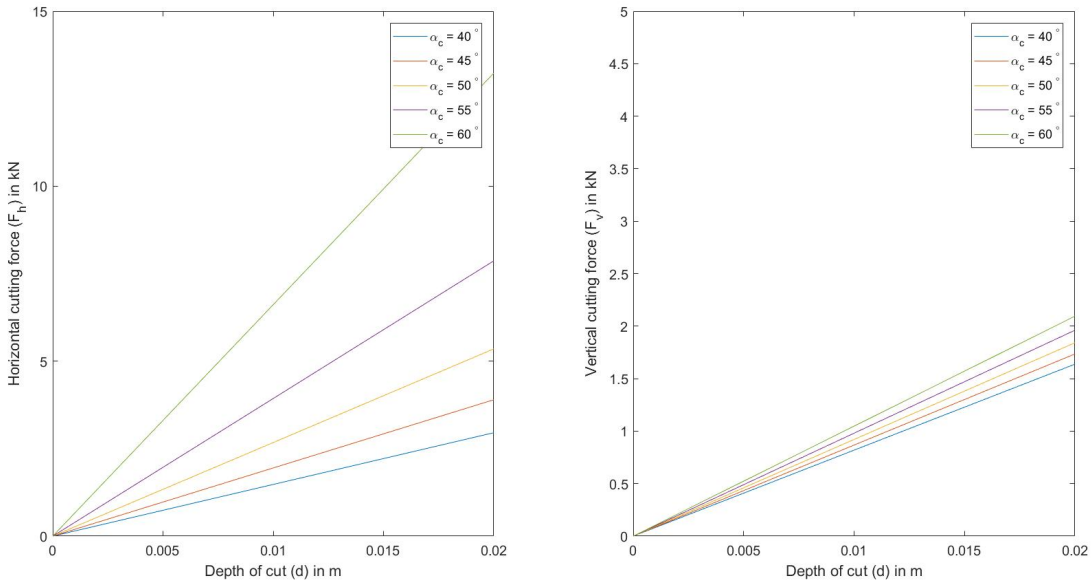

Figure 2.23: Cutting forces over depth using Tear model

An interesting observation one could make after studying figure 2.23, is that even though the model is not suitable for modelling the cutting angle of $\alpha_c = 70°$. It appears to be applicable for all other cutting angles used in this research. The value of the horizontal cutting force with a cutting angle of $\alpha_c = 60°$ seems to have start exploding, however the value for the vertical cutting force under this angle seems to follow the trend of the lower cutting angles. Therefore this model is assumed to be applicable for the cutting geometry used in this research.

2.3.4. DUCTILE - THE FLOW MODEL

The Flow model is based on the model by **Merchant, M.E.** [1945], which is used for steel cutting purposes. The Merchant model distinguishes three chip types (figure 2.24a): discontinuous chip (left), continuous chip without built-up edge (middle) and continuous chip with built-up edge (right). **Miedema, S.A.** [2014] extended the Merchant model for the continuous chip without built-up by including adhesion, gravity, inertia and pore pressure to make it applicable for rock cutting calculations. From figure 2.24b it is seen that the cutting geometry is similar to the one used in the research. Therefore the model needs no adjustments before it can be applied.

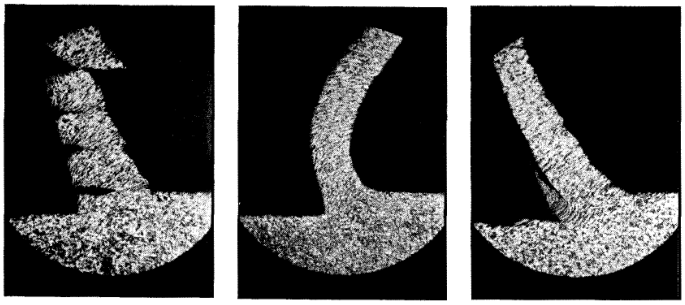

(a) Three basic chip types according to Ernst from Merchant (1945)

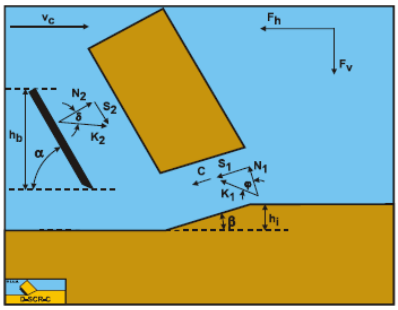

(b) Schematization by Miedema (2014)

Figure 2.24: Chip types according to Ernst from Merchant (1945) and the schematization by Miedema(2014)

With use of figure 2.24b, the horizontal and vertical equilibrium of forces can be composed, where K_1 and K_2 are the resulting forces on the blade and shear plane and C is the force due to cohesion c of the rock. From these force equilibrium equations, expressions for K_1 and K_2 can be found:

$$\sum F_h = K_1 \cdot sin(\beta+\phi) + C \cdot cos(\beta) - K_2 \cdot sin(\alpha+\delta) = 0 \tag{2.30}$$

$$\sum F_v = K_1 \cdot cos(\beta+\phi) + C \cdot sin(\beta) - K_2 \cdot cos(\alpha+\delta) = 0 \tag{2.31}$$

$$K_1 = \frac{-C \cdot cos(\alpha+\beta+\delta)}{sin(\alpha+\beta+\delta+\phi)} \tag{2.32}$$

$$K_2 = \frac{C \cdot cos(\phi)}{sin(\alpha+\beta+\delta+\phi)} \tag{2.33}$$

For the cohesion of the material, the following equation can be used, where factor λ is the velocity strengthening factor. This factor causes an increase of the cohesive strength. In rock the strengthening factor should be equal to 1, while with clay cutting this factor is approximately 2.

$$C = \frac{\lambda \cdot c \cdot h_i \cdot w}{sin(\beta)} \tag{2.34}$$

By substituting the expression for C in equations 2.32 and 2.33 leads to the formulae for the horizontal and vertical force. From these expressions it clearly shows the assumption of ductile behaviour of the rock. The area of the cut (cutting depth h_i times width of pick point w) is multiplied with the cohesion of the material. This is the property that gives the rock its resistance to ductile failure.

$$F_h = \frac{\lambda \cdot c \cdot h_i \cdot w \cdot cos(\phi) \cdot sin(\alpha+\delta)}{sin(\beta) \cdot sin(\alpha+\beta+\delta+\phi)} \tag{2.35}$$

$$F_v = \frac{\lambda \cdot c \cdot h_i \cdot w \cdot cos(\phi) \cdot cos(\alpha + \delta)}{sin(\beta) \cdot sin(\alpha + \beta + \delta + \phi)} \tag{2.36}$$

To determine the shear angle β, the principle of minimum energy $\left(\frac{\delta F_h}{\delta \beta} = 0\right)$ is applied and substituted in equations 2.35 and 2.36 to get the final expression for the horizontal and vertical cutting forces:

$$\beta = \frac{\pi}{2} - \frac{\alpha + \delta + \phi}{2} \tag{2.37}$$

$$F_h = \frac{2 \cdot c \cdot h_i \cdot w \cdot cos(\phi) \cdot sin(\alpha + \delta)}{1 + cos(\alpha + \delta + \phi)} \tag{2.38}$$

$$F_v = \frac{2 \cdot c \cdot h_i \cdot w \cdot cos(\phi) \cdot cos(\alpha + \delta)}{1 + cos(\alpha + \delta + \phi)} \tag{2.39}$$

Analysing the shear angle by substituting the rock properties of sample nr 5 reveal that this model can handle the large cutting angles used in this research. With cutting angle α_c = 70°, external friction angle δ = 20° and internal friction angle ϕ = 30° the shear angle becomes β = 30°. Considering the geometry in figure 2.24b again, this appears to be a reasonable angle for the shear plane.

However, after a first look at the force expressions, in particular the $\sin(\alpha_c + \delta)$ and $\cos(\alpha_c + \delta)$ terms, reveal a possible problem at large cutting angles. Substituting cutting angle α_c = 70° and external friction angle δ = 20° into these terms give respectively 1 and 0 as results. Considering the fact that some samples have a larger external friction angle, the cosine term even becomes negative, leading to a negative cutting force. This is, of course, impossible.

To fully check the applicability of this model, the forces are plotted over the cutting depth:

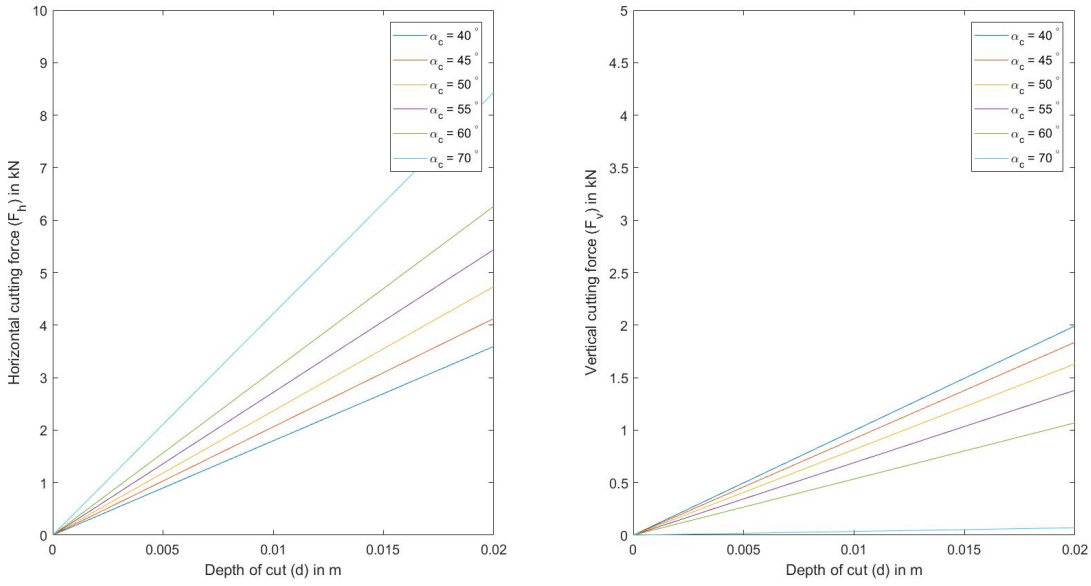

Figure 2.25: Cutting forces over depth using Flow model

Considering figure 2.25, one can observe a reasonable distribution of the forces for cutting angles in the range of 40°-60°. Although the horizontal cutting force F_h seems reasonable, the vertical cutting force F_v does not follow the trend. Therefore this cutting model is considered to be applicable, but only for the 40°-60° range.

2.4. DESCRIPTION OF THE EXPERIMENTAL LAYOUT

The experiments are conducted in a test facility of CCCC. The setup was used for a variety of experiments, reaching from the efficiency of farming equipment and (of course) different types of cutting experiments. In order to conduct the experiments several changes had to be made to the machine. First of all, a pick point is mounted on the machine to act as a cutting tool. A small pit is dug in the sandy floor of the facility to reach the concrete floor where a steel beam is connected to. The rock samples are mounted with clamps to this beam.

2.4.1. EXPERIMENTAL OVERVIEW

A 3D overview of the experiments is made in SOLIDWORKS (appendix 5.2) and is shown in figure 2.26. Once the cutting angle and depth are adjusted to the preferred values, the platform starts moving over the track and pulls the pick point through the rock sample. Every rock sample is used for 4 cutting experiments, 2 on the top and 2 on the bottom of the rock sample.

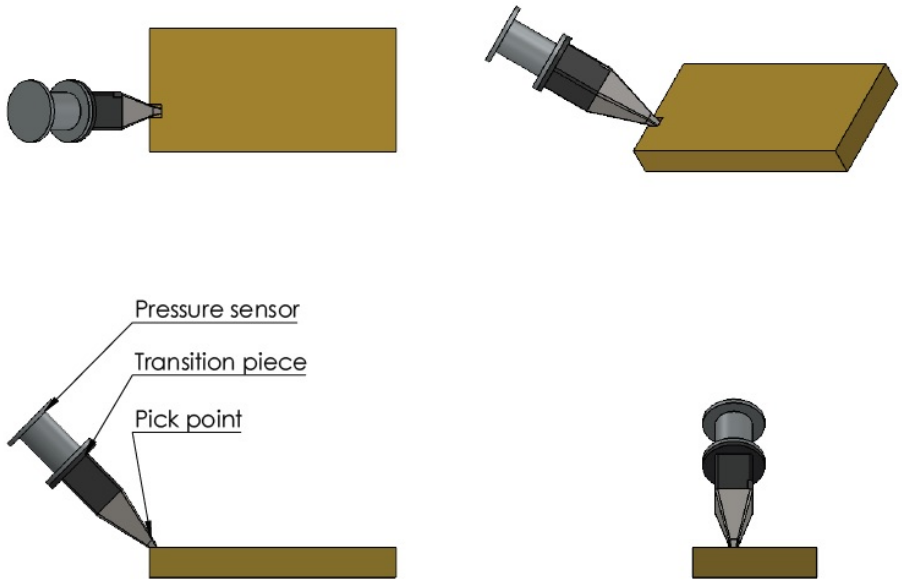

Figure 2.26: 3D overview of experiments

2.4.2. EXPERIMENTAL PROCEDURE

To conduct the experiments in a standardized manner, a experimental procedure is developed (table 2.5). The experiments start with weighing the sample.(1) Then the settings are tuned according to the experimental plan (section 2.4.4). The angle of attack,(2) the position of the pick point horizontally on the rock sample,(3) cutting depth(4) and the cutting velocity(5) are all set to the desired positions and values. Now the camera is started to start recording(6). Next, the settings of the software is checked. This starts with balancing the software to make sure the measurements start at zero.(7) Then a new file is created with the file name according to the experimental plan.(8) Then the software is armed and the recording starts.(9) To prevent any errors, a check is carried out to make sure the measurements have actually started.(10) Subsequently, the machine is started and the movement of the platform is initiated.(11) If the cutting test is finished,(12) the recording software is stopped(13) and the file is saved.(14) Also the video recording is stopped(15) and the file is saved according to the experimental plan.(16) Afterwards the cut out chips are collected for further research.(17) Finally the weight of the rock samples is determined again to calculate the production.(18)

Table 2.5: Experimental procedure

#	Item	Setting	Description
1	Samples	Weight	Check weight of the rock samples before measurement
2	Settings	Angle of attack	Set pick point angle according to experimental plan
3		Pick point position	Position pick point according to experimental plan
4		Cutting depth	Set cutting depth according to experimental plan
5		Velocity	Set velocity to 0.1 m/s
6	Camera	Start recording	Start the camera to record the experiments
7	Software	Balancing	Balance the software to start measuring at zero
8		File creation	Create new file with name according to experimental plan
9		Start recording	Begin measuring
10		Check	Check that recording actually started
11	Experiment	Start machine	Start machine from control room and proceed cutting
12		Stop machine	Stop machine from control room after the sample is cut
13	Software	Stop recording	Stop measuring
14		Save file	Save file
15	Camera	Stop recording	Stop the camera
16		Save file	Save the file according to experimental plan
17	Samples	Collect chips	Collect the cut out chips after the experiment
18		Weight	Check weight of the rock samples after measurement

2.4.3. EXPERIMENTAL SETTINGS

To determine the experimental settings, the limitations of the test setup are combined with values encountered in the dredging industry. The maximum allowed force in the pressure sensor was the bottleneck during this research. Before testing, the experimental settings were determined with use of calculations, but during experiments it was noticed that in certain configurations the forces reached the limits of the sensor. Therefore some settings were adjusted in order to preserve the sensor.

CUTTING ANGLE

When cutting soil in the dredging industry, cutting angles of 40-60° are most commonly used. While in the oil and gas industry one uses even bigger angles. The difference lays in the fact that in the dredging industry one aims for a maximum production of soil. So the cutting depths are larger, while the cutting angles are smaller. In the oil and gas industry the soil is only being scraped instead of being cut. Usually larger cutting angles are used for these applications. For academic purpose it was therefore necessary to include at least the cutting angles in the range 40-60°. However, extending this range to also include a possible application in the oil and gas industry would improve the relevance of this research and therefore it is chosen to include a 70° cutting angle as well. To investigate the influence of the cutting angle on the cutting process intervals of 5° were used. So the used cutting angles are: 40, 45, 50, 55, 60 and 70°.

CUTTING DEPTH

The cutting depth is one of the main factors in the occurring cutting force. Increasing the cutting depth increases the cutting forces as well. In most force prediction models it is assumed that the cutting force increases linearly. Like mentioned earlier, the force should not exceed the maximum allowed force of the sensor. For practical reasons it was chosen to use increments of 0.5cm. Measuring the cutting depth with a ruler leaves some room for error, making the increments smaller was therefore impracticable. To eliminate potential measurement errors, the actual occurring cutting depth was measured in the rock sample after the experiment and this value is used for later calculations. So the experiments were first conducted with a cutting depth of 0.5cm and increased with increments of 0.5cm. In some configurations and with a cutting depth of 1.5cm the forces reached the limits of the sensor. Therefore cutting depths of 0.5, 1.0 and 1.5cm are used. Since every rock sample had room for 4 cutting tests, the final test cut is used for the intermediate values (in case the cutting depths were not distributed evenly enough in the preferred range).

CUTTING VELOCITY

Although the cutting velocity is not included in the cutting force prediction models, it has its influence on the experiments. Before testing, the pick point is positioned in the desired configuration at a small distance from the rock, so at the time the pick point hits the rock it has already reached the desired velocity. Some trial runs where done with a cutting velocity of 0.1m/s but it was noticed that the impact of the pick point when it reached the rock sample produced a large peak force. In order to preserve the sensor, the velocity was reduced to a value of 0.05m/s, which reduced the peak force to acceptable levels. Another advantage of using a smaller velocity is the increased length of the dataset obtained from the experiments. With a sample length of approximately 1m and a velocity of 0.05m/s it gives an actual cutting time of 20 sec. Which, for rock cutting experiments, is a very large time frame.

2.4.4. EXPERIMENTAL PLANNING

Every sample (numbered 5-9) is used for 4 cuts. Each cut is indicated with either A,B,C or D. Tests indicated with A are executed with the cutting depth set to 0.5cm, B with 1.0cm and C with 1.5cm. Tests D were supposed to be used for intermediate cutting depths. Unfortunately, the sensor broke near the end of the research (pictures in appendix 5.2). However, enough data was gathered already so the setback was minimal. Whenever intermediate depths are used in the experiments, the depth is noted with the range in table 2.6. This table contains a list with the executed experiments. A full overview of the experimental planning is attached in appendix 5.2.

Table 2.6: Experimental planning

#	Date	Sample	Exp.	Depth cm	Angle °	#	Date	Sample	Exp.	Depth cm	Angle °
1	28-08-2018	5	A	0.5	40	13	11-09-2018	6	A	0.5	55
2	28-08-2018	5	B	1.0	40	14	11-09-2018	6	B	1.0	55
3	28-08-2018	5	C	1.5	40	15	11-09-2018	6	C	1.5	55
4	19-09-2018	5	D	0.5-1.0	40	16	-	-	-	-	-
5	31-08-2018	9	A	0.5	45	17	11-09-2018	7	A	0.5	60
6	31-08-2018	9	B	1.0	45	18	11-09-2018	7	B	1.0	60
7	31-08-2018	9	C	1.5	45	19	11-09-2018	7	C	1.5	60
8	19-09-2018	9	D	0.0-0.5	45	20	-	-	-	-	-
9	10-09-2018	8	A	0.5	50	21	19-09-2018	7.2	A	0.5	70
10	10-09-2018	8	B	1.0	50	22	19-09-2018	7.2	B	1.0	70
11	10-09-2018	8	C	1.5	50	23	19-09-2018	7.2	C	1.5	70
12	19-09-2018	8	D	0.5-1.0	50	24	-	-	-	-	-

3

EXPERIMENTAL STAGE

First the calibration process of the pressure sensor is described. Afterwards one set of experiments is explained in detail.

3.1. CALIBRATING THE EXPERIMENTAL SETUP

In order to get from the uV output from the pressure sensor to a force, the supplier provided calibration tables for every direction: X-positive (X^+), X-negative (X^-), Y-positive (Y^+), Y-negative (Y^-) and Z-positive (Z^+). A copy of the original files is attached in appendix 5.2. A merged table is presented in table 3.1. The orientation of the axis-system is determined by the pressure sensor (figure 3.1). The Z axis is in line with the pick point, while the X^+ is faced upwards and Y^+ to the left.

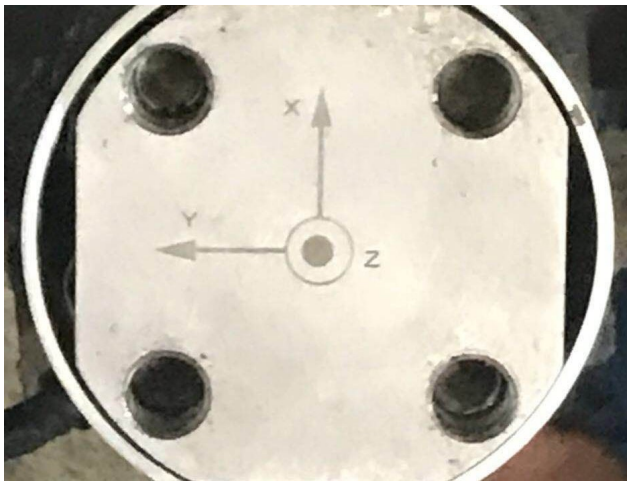

Figure 3.1: Orientation axis system on pressure sensor

To get from the uV output to the force, the supplier included formula 3.1. Where F is the force in kN, uV is the output from the sensor and c is a constant. Since the uV and the corresponding weights are known formula 3.1 is rewritten to solve for c with application of $F = \frac{kg \cdot g}{1000}$ (equation 3.2).

$$F = \frac{uV \cdot 3200}{c \cdot 2000} \tag{3.1}$$

$$c = \frac{uV \cdot 3200}{kg \cdot g \cdot 2} \tag{3.2}$$

Table 3.1: Merged calibration tables and corresponding constants

Weight	X		Y		Z		C_x		C_y	C_z
	X^+	X^-	Y^+	Y^-	Z^+					
kg	uV	uV	uV	uV	uV	C_{x+}	C_{x-}	C_{y+}	C_{y-}	C_{z+}
0	1	1	1	1	1	1	-	-	-	-
200	227	-222	202	-202	18	185.1	-181.0	164.7	-164.7	14.7
400	456	-446	404	-417	36	185.9	-181.9	164.7	-170.0	14.7
600	686	-669	608	-630	54	186.5	-181.9	165.3	-171.3	14.7
800	913	-896	815	-847	72	186.2	-182.7	166.2	-172.7	14.7
1000	1150	-1122	1024	-1054	90	187.6	-183.0	167.0	-171.9	14.7
1200	1380	-1350	1236	-1269	107	187.6	-183.5	168.0	-172.5	14.5
1400	1621	-1575	1445	-1486	125	188.9	-183.5	168.3	-173.1	14.6
1600	1846	-1800	1659	-1698	142	188.2	-183.5	169.1	-173.1	14.5
1800	2092	-2020	1865	-1908	160	189.6	-183.0	169.0	-172.9	14.5
2000	2326	-2242	2070	-2125	179	189.7	-182.8	168.8	-173.3	14.6
2200	2572	-2466	2266	-2345	196	190.7	-182.8	168.0	-173.9	14.5
2400	2792	-2690	2485	-2557	213	189.7	-182.8	168.9	-173.8	14.5
2600	3039	-2915	2701	-2771	231	190.6	-182.9	169.4	-173.8	14.5
2800	3273	-3139	2899	-2984	248	190.7	-182.9	168.9	-173.8	14.4
3000	3490	-3364	3105	-3200	264	189.7	-182.9	168.8	-174.0	14.4
3200	3733	-3622	3312	-3411	285	190.3	-184.6	168.8	-173.9	14.5

From the calibration tables 16 data points are known, each with a corresponding weight and sensor output. These values are substituted in equation 3.2, resulting in the constants (the right hand side of table 3.1). For every direction the constants are plotted against the uV signal. Next, a line is fitted through the points which shows the behaviour of a 3^{rd} degree polynomial (figure 3.2).

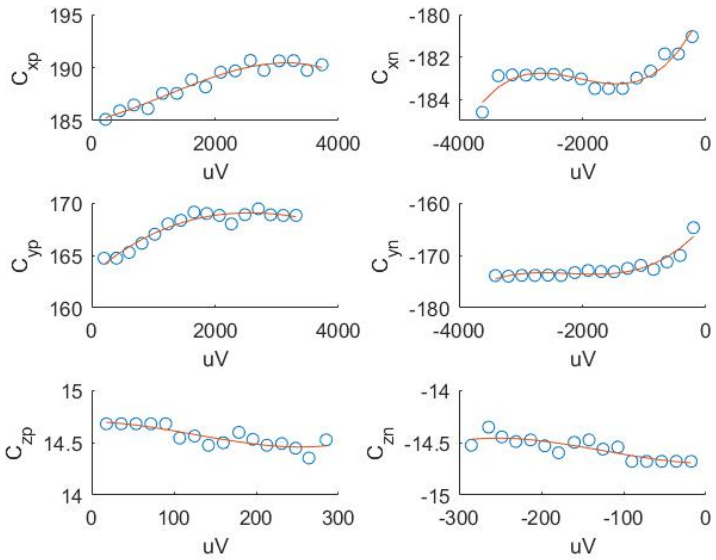

Figure 3.2: Calibration table pressure sensor

The intermediate values of this polynomial are calculated with use of formula 3.3, where x_i is a known value from the calibration output, C is the corresponding constant, n is the degree of the polynomial (for this case $n = 3$) and result P is the vector containing all intermediate values. When plotting polynomial P against the range of sensor output for every direction, figure 3.3 arises.

$$C_{i,j} = x_1 uV^n + x_2 uV^{n-1} + x_3 uV^{n-2} + x_4 \tag{3.3}$$

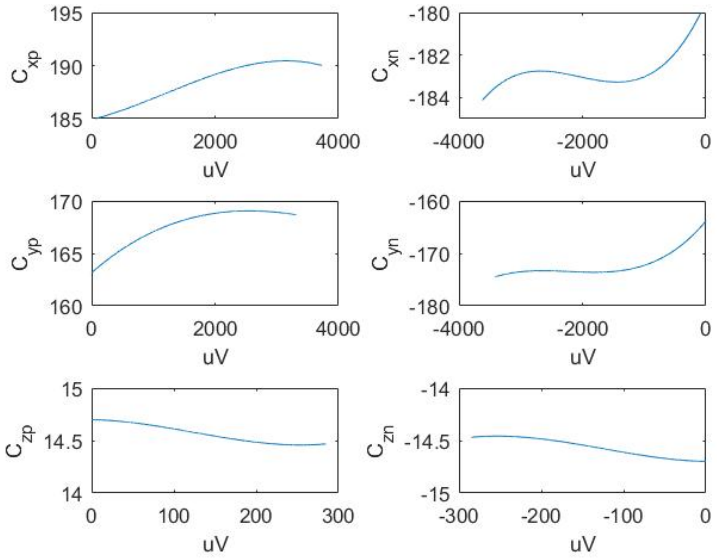

Figure 3.3: Polynomial pressure sensor

For comparison figure 3.2 and 3.3 are plotted together in figure 3.4. As one can see, the constructed polynomial P is an exact copy of the fitted line through the data points for each direction. But more importantly it not only contains the 16 data points, but also all intermediate values.

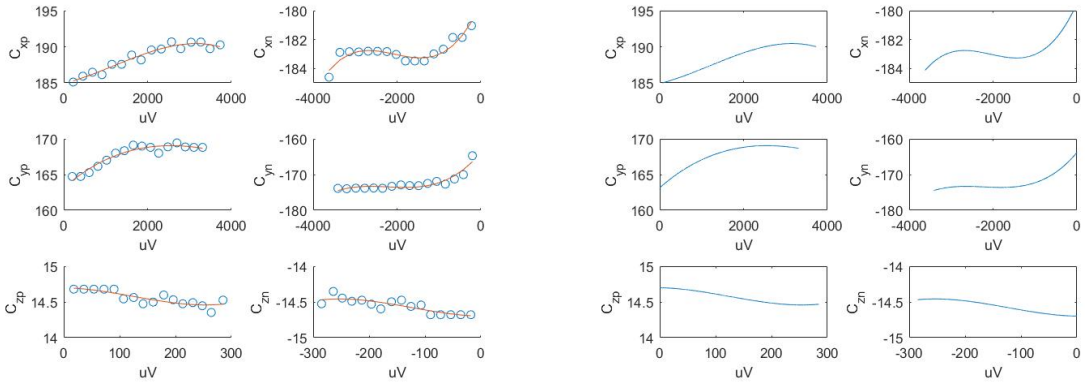

(a) Line fit through data points

(b) Constructed polynomial

Figure 3.4: Comparison data points and constructed polynomial

3.1.1. ORIENTATION OF AXIS SYSTEM

The values of the uV output of the pressure sensor are searched in polynomial P. Since every value for uV is connected to a certain value for coefficient C, every variable in formula 3.2 is known, except for the weight in kg. Rewriting this formula and substituting the sensor output, results in the weight values. Simply multiplying the weight with the gravitation (g=9,81m/s^2) gives the force. However, the pressure sensor is mounted under angle α_s, where the angle of the sensor is the cutting angle minus the pick point angle: $\alpha_s = \alpha - \alpha_p$. The orientation of the sensor is sketched in figure 3.5, where FZ is the force in z-direction, FX$^+$ and FX$^-$ are the forces in positive and negative x-direction. Keep in mind that the z-axis is in line with the cutting direction and the x-axis is vertical, with the positive pointing upwards. Another note, the orientation of the pressure sensor has no influence on the force in y-direction (perpendicular to figure 3.5).

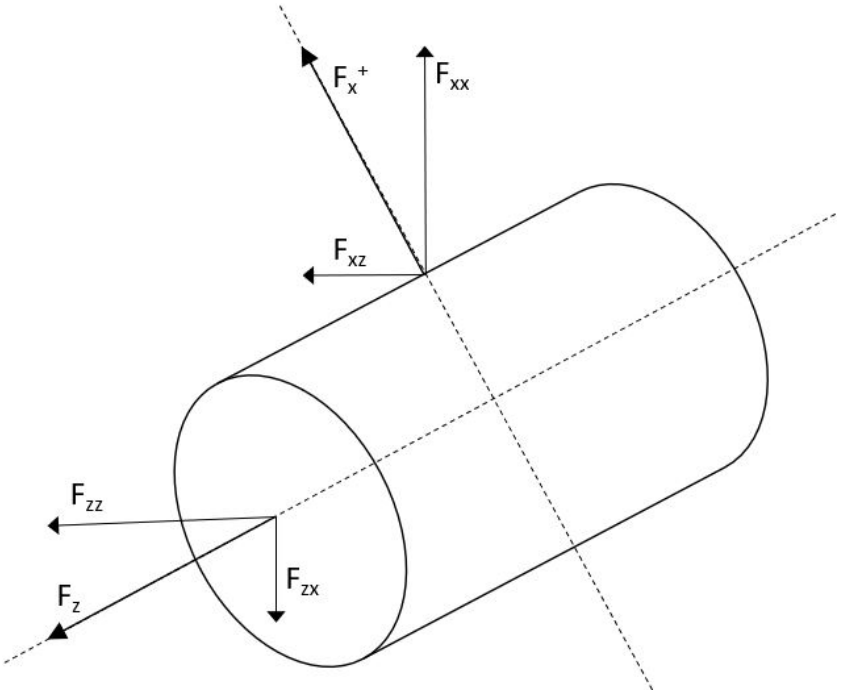

Figure 3.5: Pressure sensor orientation

From this image, one can identify two scenario's: where FZ is positive and FX is positive (1) and where FZ is positive and FX is negative(2). The formula's to calculate the forces in both scenario's are given below:

SCENARIO 1: FZ POSITIVE AND FX POSITIVE

Horizontal force:

The contribution of FZ to the horizontal force is FZz, while the contribution of FX$^+$ to the horizontal force is FXz. Since these forces are directed in opposite direction, FZz in positive and FXz in negative direction, FXz is deducted from FZx.

$$F_z = FZz - FXz = cos(\alpha) \cdot FZ - sin(\alpha) \cdot FX^+ \tag{3.4}$$

Vertical force:

The contribution of FZ to the vertical force is FZx, while the contribution of FX$^+$ is FXx. Since these forces are directed in the same direction, FZx and FXx are added together:

$$F_x = FZx + FXx = sin(\alpha) \cdot FZ + cos(\alpha) \cdot FX^+ \tag{3.5}$$

SCENARIO 2: FZ POSITIVE AND FX NEGATIVE

Horizontal force:

The contribution of FZ to the horizontal force is again FZz, while the contribution of FX^- to the horizontal force is FXz. Since these forces are directed in the same direction, FZz and FXz are added together.

$$F_z = FZz + FXz = cos(\alpha) \cdot FZ + sin(\alpha) \cdot FX^- \tag{3.6}$$

Vertical force:

The contribution of FZ to the vertical force is FZx, while the contribution of FX^- is FXx. Since these forces are directed in opposite direction, FXx is deducted from FZx:

$$F_x = FZx - FXx = sin(\alpha) \cdot FZ - cos(\alpha) \cdot FX^- \tag{3.7}$$

For the output of the sensor, the scenario has to be checked and according to formulae 3.4-3.7 the forces need to be either deducted or added together. Finally, the total cutting force can be calculated with:

$$F_t = \sqrt{F_x^2 + F_y^2 + F_z^2} \tag{3.8}$$

3.2. LINEAR ROCK CUTTING EXPERIMENTS

The experiments are described per sample, according to table 2.6. The first set of four experiments are described in detail. For the remaining experiments the same algorithm is used but only the results are shown. A full description of all experiments, including all plots, is attached in appendices 5.2-.26. After a short recap on the rock sample characteristics several aspects are elaborated upon in the next section:

CUTTING FORCES

The cutting forces per experiment are plotted in time. These plots contain the entire time window, from the start of the machine until the machine shuts off. During the post processing of the data, the time frame will be shortened so it only contains the actual cutting process.

MAXIMUM CUTTING FORCES

Subsequently, for every set of experiments the maximum forces are determined and combined with the average cutting depth during the test. After plotting this into a single graph it gives insight in the influence of the cutting depth on the force.

PARTICLE SIZE DISTRIBUTIONS

After every experiment the weight of the cut out material is determined. The material is than spread out in the sieves in figure 3.6a. These sieves have a hole diameter of 20mm, 10mm, 5mm and 2mm. So the particle distribution can be determined with the following ranges: >20mm, 20-10mm, 10-5mm, 5-2mm and <2mm. When all material is spread out in the sieves, the stack is first manually shook to initiate the first particles to fall down. Afterwards the stack is placed on a vibrating plate figure 3.6b. To prevent the rock pieces from breaking during vibration, the vibration time was limited to 15 seconds. The particle size distribution is an indicator of the type of failure, size of the crushed zone and other important parameters.

(a) Stack of sieves

(b) Stack of sieves on vibration machine

Figure 3.6: Stack of sieves and vibration machine to determine the particle size distribution of every experiment

CUTTING PROFILES

After the experiments the cutting profiles in the rock samples were constructed. Figure 3.7b contains a detailed picture of a rock sample after it was cut. It is clearly visible that a trapezoidal shape arises, which is schematized in figure 3.7a. In this schematization the width of the cutting tool is indicated with w, the depth of the cut with h and the width of the cut width w_c.

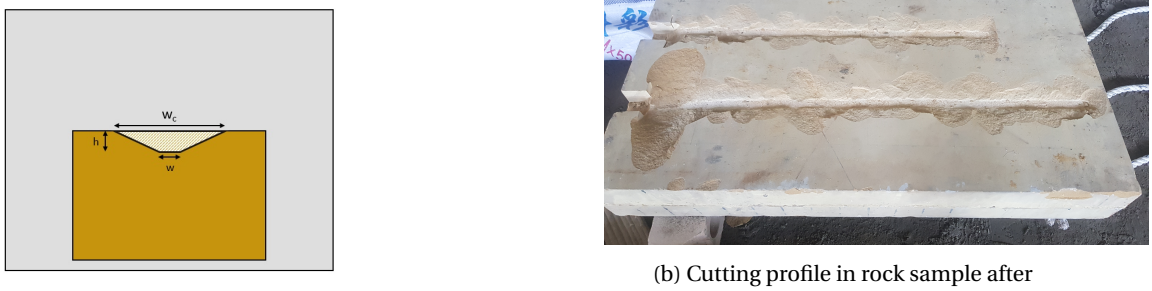

(a) Schematization of cutting profile

(b) Cutting profile in rock sample after experiment

Figure 3.7: Cutting profiles after experiment

In the description of the experiments the cutting profiles are constructed in MATLAB: one for the depth and one for the width of the cut. Keep in mind that the shape of the cut is always trapezoidal, as portrait in the above figure.

3.2.1. DETAILED DESCRIPTION OF CUTTING EXPERIMENTS

The properties of sample number 5 are listed below in table 3.2. This sample was used to conduct 4 cutting experiments. The first three were performed with the machine set to depths of 0.5cm, 1.0cm and 1.5cm. The fourth cut is used for an intermediate cutting depth, depending on the average depths of the first three cuts.

Table 3.2: Sample 5: rock characteristics

	F_U kN	F_B kN	UCS MPa	BTS MPa	B [-]	E GPa	C MPa	ϕ °	δ °	ρ kg/m^3
Sample 5	44.796	8.252	18.855	1.676	11.294	1.047	5.489	30	20	2276.850

Note the positive F_x is pointing upwards, the positive F_y points to the left of the cutting direction and the positive F_z is in cutting direction. Equation 3.8 is used to calculate total force F_t.

EXPERIMENT 5A

The graphs in in figures 3.8 shows the cutting forces in the time for experiment 5A (sample 5, 0.5cm depth, 40 degrees). It is seen that the cutting starts 50 seconds after the sensor started measuring and the total cutting time is approximately 15 seconds.

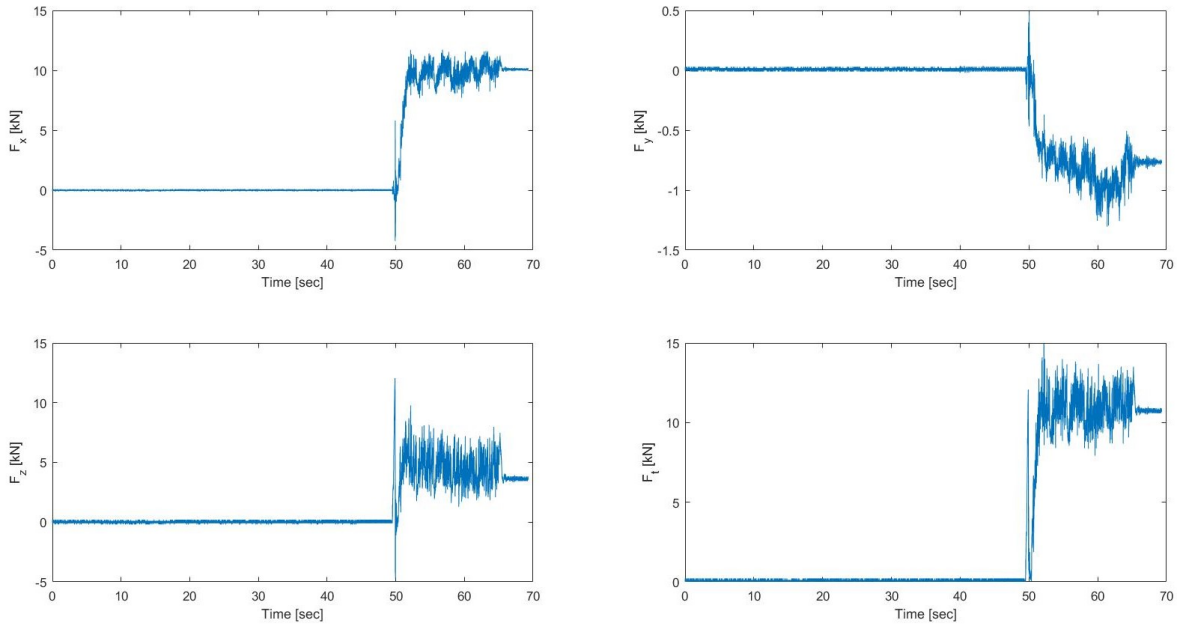

Figure 3.8: Experiment 5A: force in time

An analysis of the video material of this experiment indicates there is a certain amount of vibration in the pick point during the cutting process. The peaks in the force signal are the maximum forces necessary to break out the rock pieces. After breaking out the pieces, the pick point swings forwards until it reaches the intact rock sample again. This movement results in the troughs in the force signal.

From measuring the depth and width of the cut in the rock sample, a cutting profile was constructed with use of MATLAB (figure 3.9). The vibrations in the pick point, in combination with the out breaking rock samples, results in a non-uniform cutting depth over the length. This results in an average cutting depth of 0.49cm. Also the width is influenced by the above described phenomena. Especially the first rock piece with a maximum width of 15cm is huge compared with the width of the rest of the cut.
The weight of the cut out material was 0.229kg. This is important for the particle size distribution calculations, which is described later in this chapter. A summary of the discussed laboratory data is presented in table 3.3.

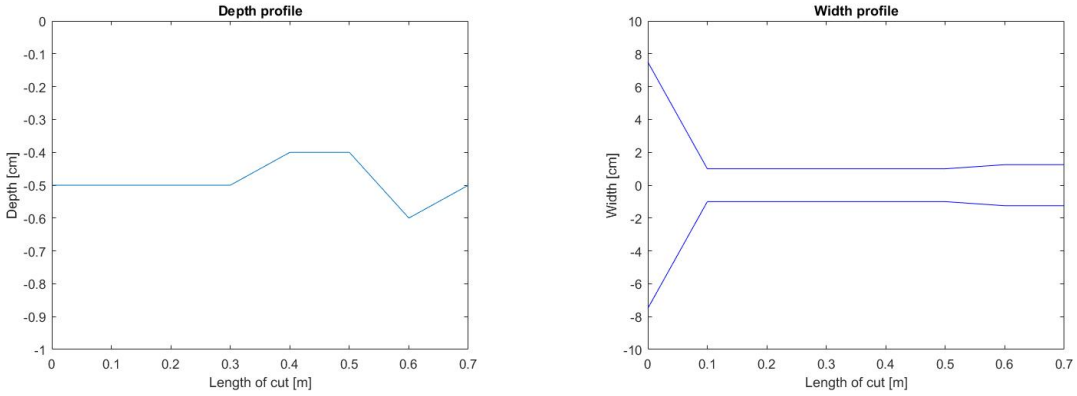

(a) Depth of cut (b) Width of cut

Figure 3.9: Depth and width of experiment 5A

Table 3.3: Laboratory data of experiment 5A

	Cutting time [sec]	Average depth [cm]	Average width [cm]	Length [m]	Weight [kg]
Experiment 5A	15	0.49	3.75	0.7	0.229

EXPERIMENT 5B

In figures 3.10 the cutting forces are plotted in time for experiment 5B (sample 5, 1.0cm depth, 40 degrees). It is seen that the cutting starts approximately 25 seconds after the sensor started measuring and the total cutting time is approximately 12 seconds.

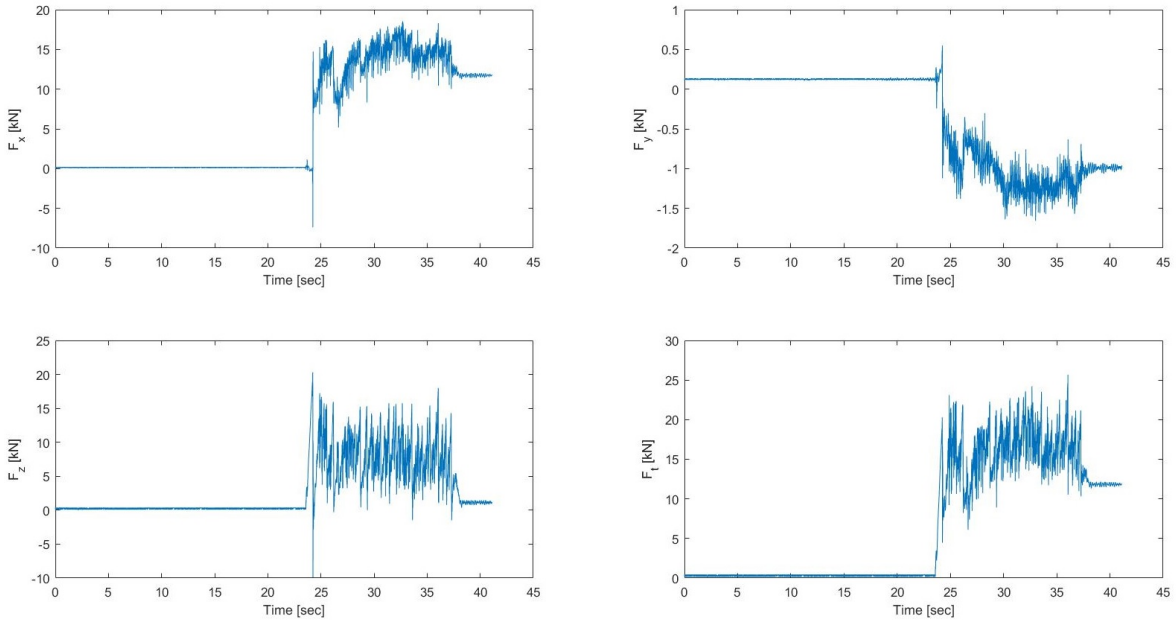

Figure 3.10: Experiment 5B: force in time

The cutting profile from experiment 5B is presented in figure 3.11. From this data an average cutting depth of 1.17cm is measured. The average width of the cut is 8.17cm. An interesting observation seen from the depth profile: even though the machine was set to a cutting depth of 1.0cm, the depth at the beginning is almost 1.5cm. This is probably due to the breaking out of a large rock piece. After cutting for 0.3m the cutting depth finally converges to the set depth of 1.0cm. Also the width of the cut is larger compared with the experiment

5A.

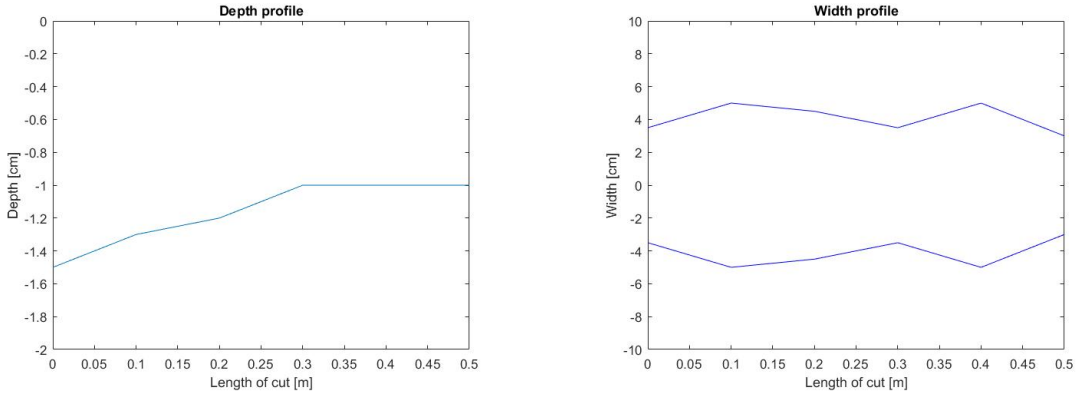

(a) Depth of cut (b) Width of cut

Figure 3.11: Depth and width of experiment 5B

The production of this cut was 0.507kg. Table 3.4 summarizes the discussed laboratory findings so far:

Table 3.4: Laboratory data of experiment 5B

	Cutting time [sec]	Average depth [cm]	Average width [cm]	Length [m]	Weight [kg]
Experiment 5B	12	1.17	8.17	0.5	0.507

EXPERIMENT 5C

For experiment 5C (sample 5, 1.5cm depth, 40 degrees), the force output is plotted in figure 3.12. The cutting process started approximately 15 seconds after the sensor was switched on. The total cutting time is about 18 seconds.

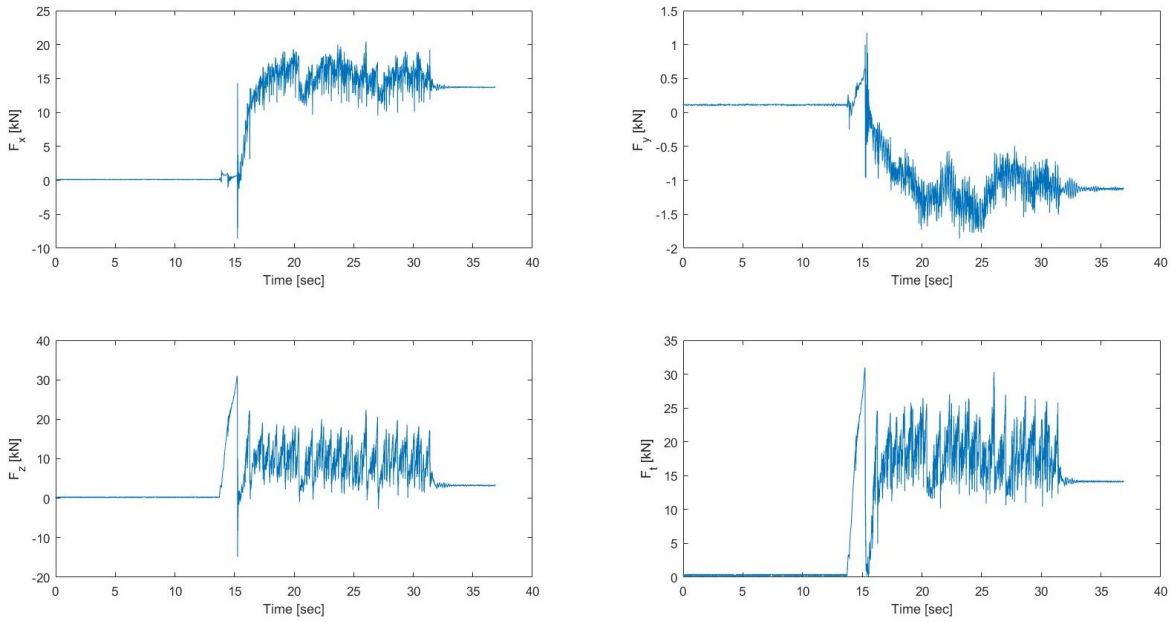

Figure 3.12: Experiment 5C: force in time

The cutting profile for experiment 5C is presented in figure 3.13. Again, a large piece of rock is cut out at the start of the cutting process. The depth converges afterwards to a value just under the 1.5cm. The width of the cut increased compared to experiments 5A and 5B to approximately 10cm. The average cutting depth was 1.39cm, while the average width was 11.38cm.

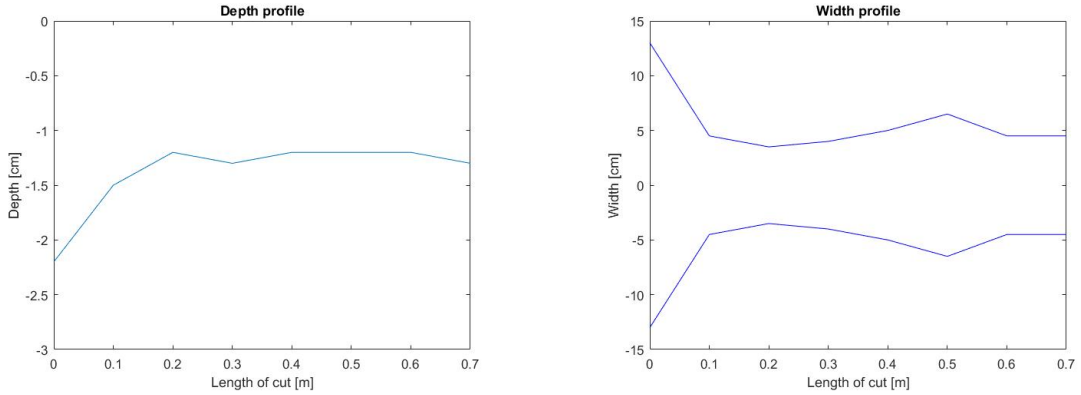

(a) Depth of cut

(b) Width of cut

Figure 3.13: Depth and width of experiment 5C

The production of this cut was 1.221kg. Table 3.5 contains the above discussed values:

Table 3.5: Laboratory data of experiment 5C

	Cutting time [sec]	Average depth [cm]	Average width [cm]	Length [m]	Weight [kg]
Experiment 5C	18	1.39	11.38	0.7	1.221

EXPERIMENT 5D

Analysing the average cutting depths of experiments 5A, 5B and 5C (table 3.6) results in the choice for the depth of experiment 5D. Increasing the cutting depth above 1.39cm risks damaging the pressure sensor. The difference in depths between 5B and 5C is only minimal and practically not doable considering the vibrations in the machine and the breaking out of rock pieces, both influencing the cutting depth. Therefore it is chosen to set the machine to 0.7-0.8cm to get another data point between 5A and 5B.

Table 3.6: Average cutting dephs of experiments 5A-5C

	Experiment 5A [cm]	Experiment 5B [cm]	Experiment 5C [cm]
Average cutting depth	0.49	1.17	1.39

Figure 3.14 shows the cutting forces plotted against time. The cuttings process started approximately 8 seconds after the pressure sensor started recording. The total cutting time is about 18 seconds.

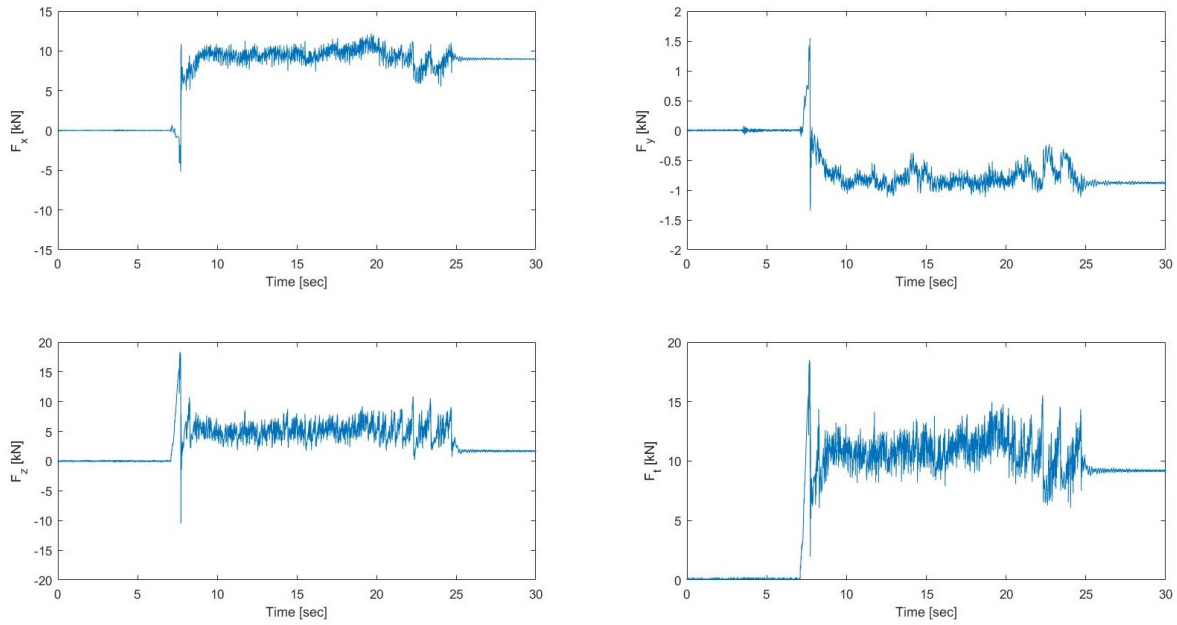

Figure 3.14: Experiment 5D: force in time

The production of this cut was 0.145kg, which is remarkable compared to experiment 5A. The machine was set to a larger depth, but this did not increase the production. The reason for this is shown in figure 3.15. The depth is indeed larger than 5A, but the width of the out breaking rock pieces is considerably smaller. The average depth was 0.66cm, while the average width is 3.2cm.

Table 3.7: Laboratory data of experiment 5D

	Cutting time [sec]	Average depth [cm]	Average width [cm]	Length [m]	Weight [kg]
Experiment 5D	18	0.66	3.2	0.9	0.145

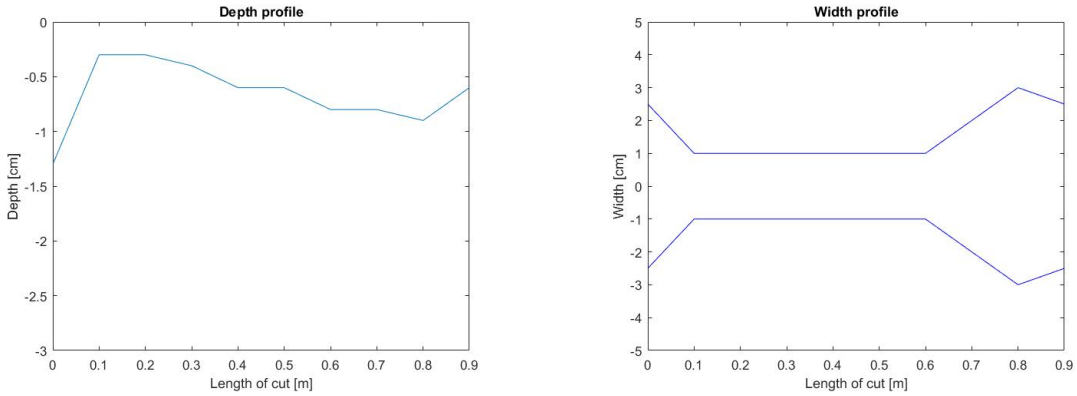

(a) Depth of cut

(b) Width of cut

Figure 3.15: Depth and width of experiment 5D

Since only the actual cutting process is of value for this research, the start and end of the data is removed from the set. To get a uniform choice for the time frame, this is based on the first derivative of the force with respect to time. If this exceeds a certain value, the data is included in the dataset (equations 3.9 until 3.11). For tests A, B and C different constants are used, because the increased cutting depth increases the peak force when the pick point hits the rock sample. This increases the slope of the force signal and thus the value of the

derivative. The values are determined with trial and error combined with the visual interpretation of the total force signal.

$$dA = \frac{dF_A}{dt} > 20[\frac{kN}{s}] \tag{3.9}$$

$$dB = \frac{dF_B}{dt} > 30[\frac{kN}{s}] \tag{3.10}$$

$$dC = \frac{dF_C}{dt} > 60[\frac{kN}{s}] \tag{3.11}$$

The value for the derivative in experiment D depends on the depth used. If the depth of experiment D lays between A and B, the value for the derivative is 25. If it lays between B and C the value is 45.

For experiment 5A this method results in figure 3.16, which contains the force data from approximately t=51 seconds to t=65 seconds. Table 3.8 contains the values of the maximum and mean forces.

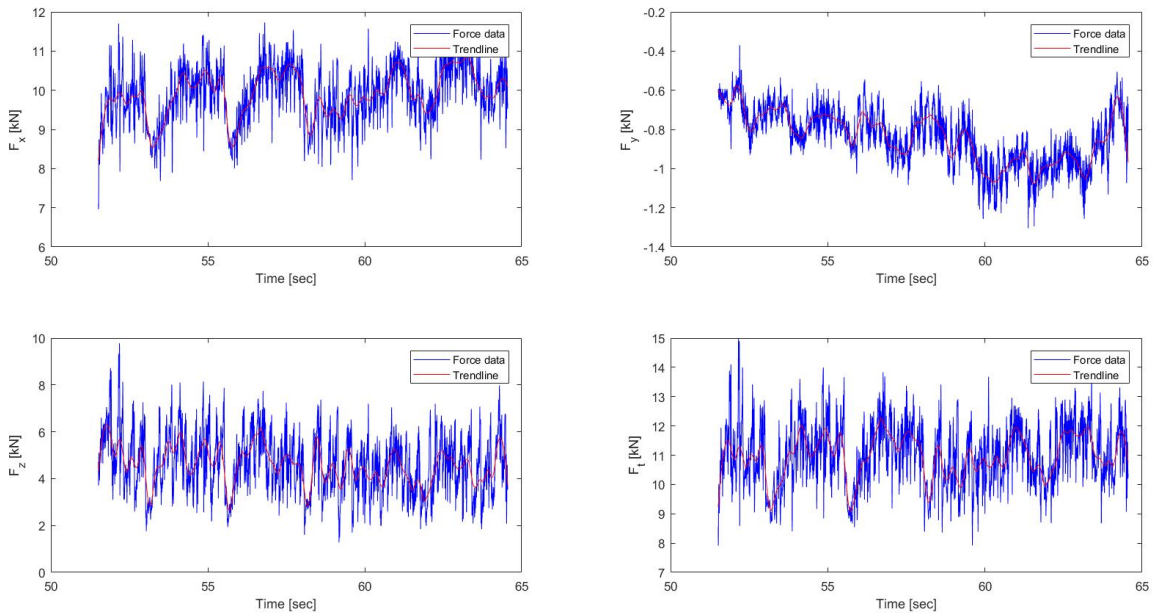

Figure 3.16: Experiment 5A: force in time

Table 3.8: Experiment 5A: cutting forces

	$F_{x,max}$ [kN]	$F_{x,mean}$ [kN]	$F_{y,max}$ [kN]	$F_{y,mean}$ [kN]	$F_{z,max}$ [kN]	$F_{z,mean}$ [kN]	$F_{t,max}$ [kN]	$F_{t,mean}$ [kN]
Experiment 5A	11.72	9.89	-0.37	-0.84	9.78	4.64	14.98	11.00

Analysing the force output from experiment 5B results in figure 3.17, which contains the force data from approximately t=25 seconds to t=36 seconds. Table 3.9 contains the cutting forces of experiment 5B.

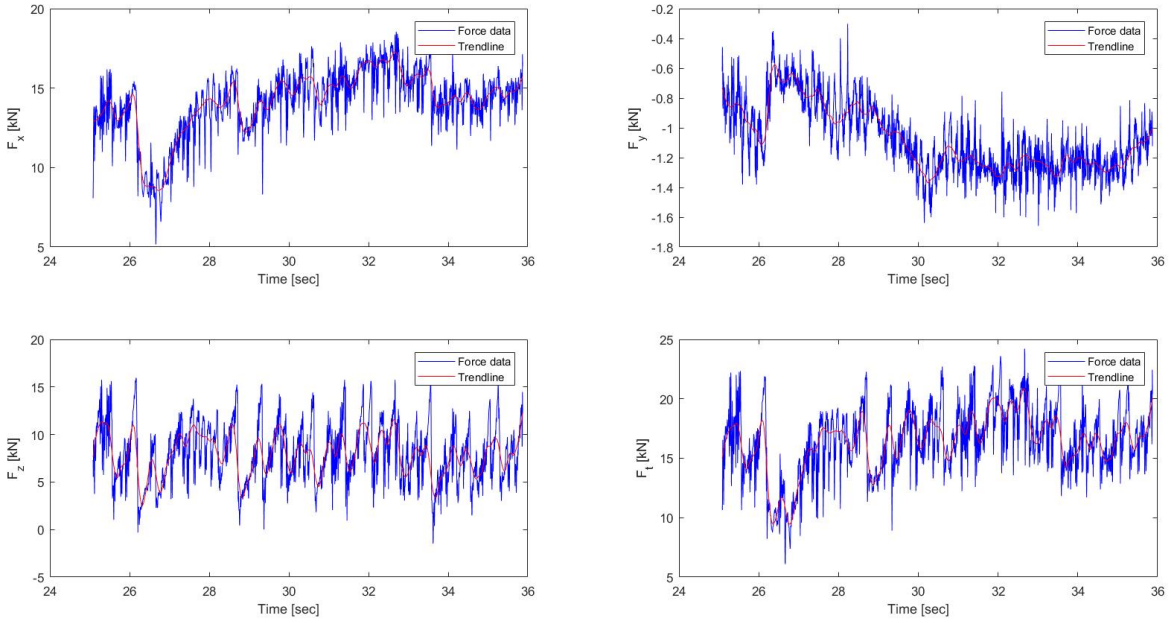

Figure 3.17: Experiment 5B: force in time

Table 3.9: Experiment 5B: cutting forces

	$F_{x,max}$ [kN]	$F_{x,mean}$ [kN]	$F_{y,max}$ [kN]	$F_{y,mean}$ [kN]	$F_{z,max}$ [kN]	$F_{z,mean}$ [kN]	$F_{t,max}$ [kN]	$F_{t,mean}$ [kN]
Experiment 5B	18.54	14.04	-0.30	-1.07	15.96	8.04	24.22	16.38

The reduced force data for experiment 5C is presented in figure 3.18.

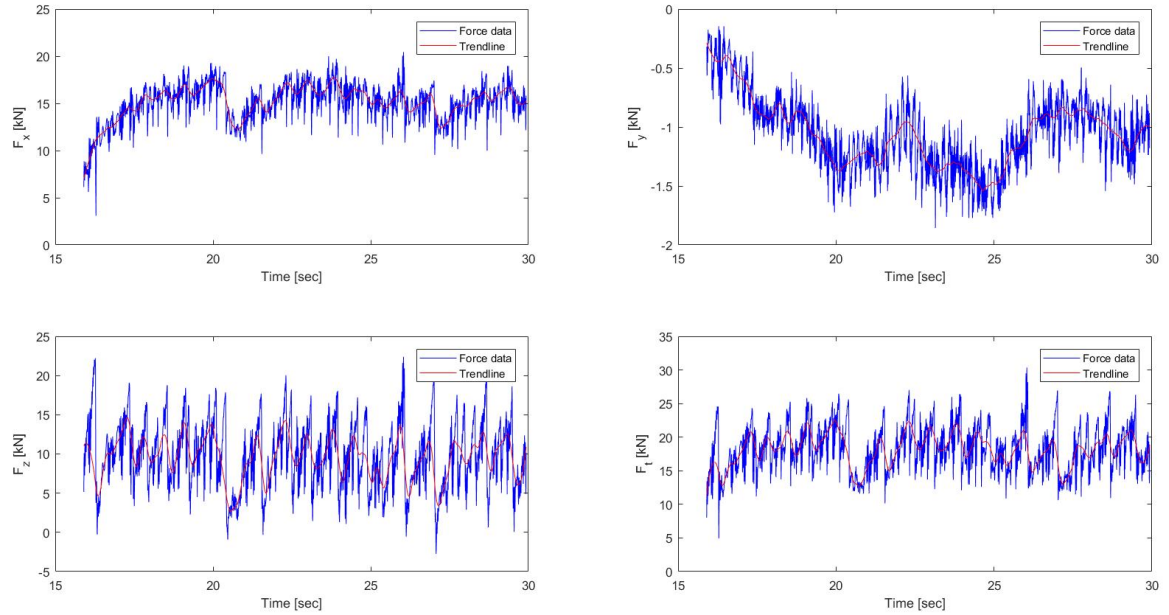

Figure 3.18: Experiment 5C: force in time

Table 3.10: Experiment 5C: cutting forces

	$F_{x,max}$ [kN]	$F_{x,mean}$ [kN]	$F_{y,max}$ [kN]	$F_{y,mean}$ [kN]	$F_{z,max}$ [kN]	$F_{z,mean}$ [kN]	$F_{t,max}$ [kN]	$F_{t,mean}$ [kN]
Experiment 5C	20.44	15.01	-0.15	-1.06	22.40	9.79	30.35	18.24

Figure 3.19 shows the force data for experiment 5D.

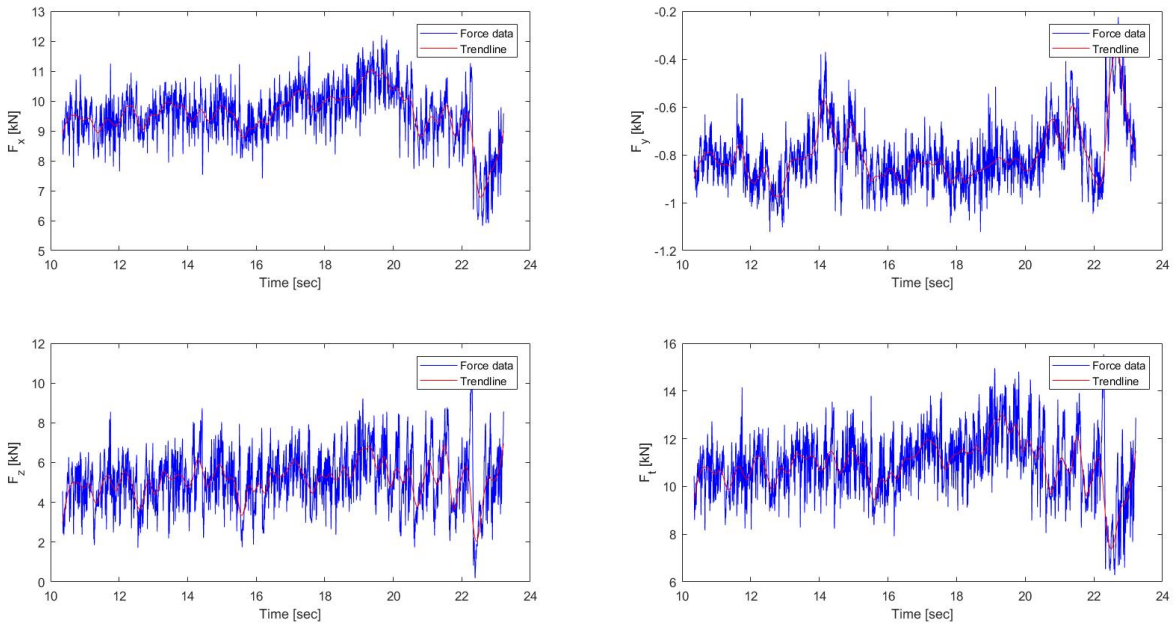

Figure 3.19: Experiment 5D: force in time

Table 3.11: Experiment 5D: cutting forces

	$F_{x,max}$ [kN]	$F_{x,mean}$ [kN]	$F_{y,max}$ [kN]	$F_{y,mean}$ [kN]	$F_{z,max}$ [kN]	$F_{z,mean}$ [kN]	$F_{t,max}$ [kN]	$F_{t,mean}$ [kN]
Experiment 5D	12.19	9.53	-0.22	-0.80	10.86	5.16	15.53	10.92

Combining the maximum forces from experiments 5A, 5B, 5C and 5D with the average depth during the experiment gives the maximum forces over the depth (figure 3.20). The circular dots represent the maximum cutting force at the average depth of the experiment. A fifth point is added at a depth of 0cm with 0 kN force. The trendline is a first degree line fitted through the five data points.

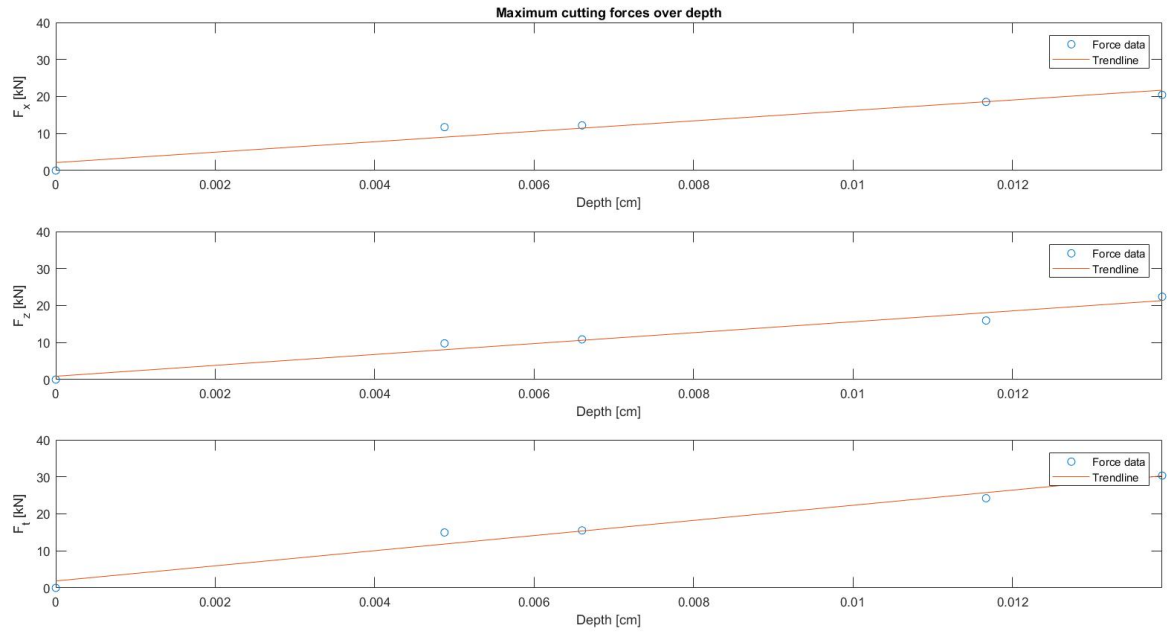

Figure 3.20: Experiment 1-4: maximum forces over depth

PARTICLE SIZE DISTRIBUTIONS

Particle size distributions have been constructed by sieving and weighing the cut out material. For experiments 1-4 the particle size distributions are presented in figure 3.21.

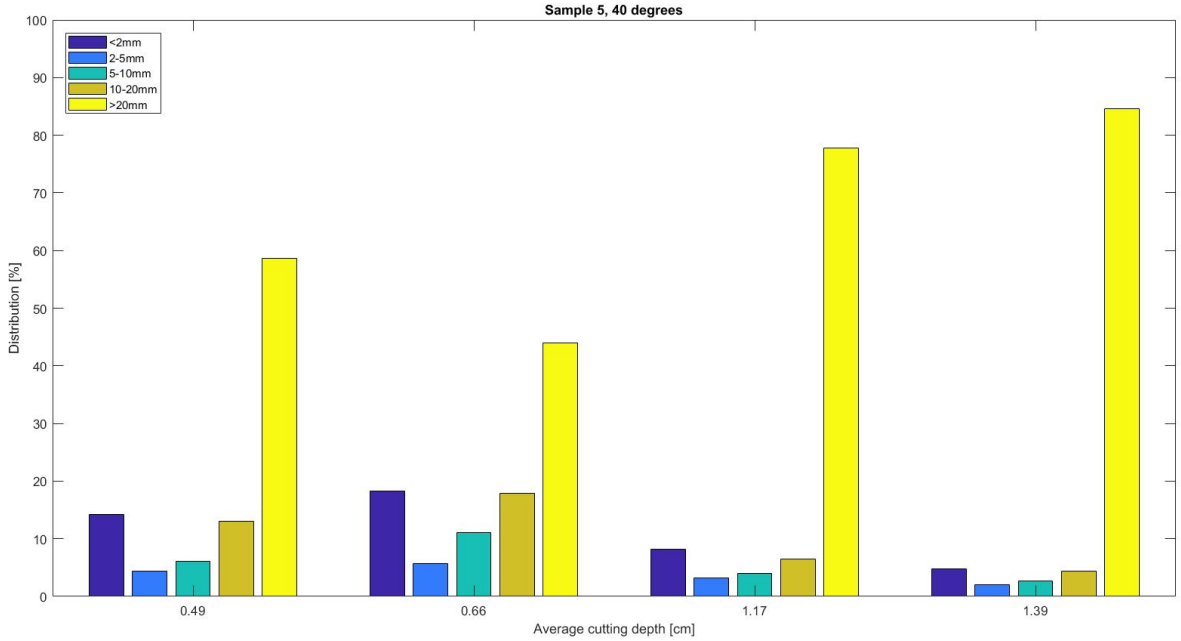

Figure 3.21: Particle size distributions experiments 1-4

3.2.2. RESULTS OF REMAINING CUTTING EXPERIMENTS

The same algorithm is used to determine the maximum cutting forces and particle size distributions of the remaining cutting experiments. This is described in appendix 5.2 until appendix .26.

4
DATA ANALYSIS

First the most suitable calculation model is chosen based on the failure mode. The measurements are then compared with the calculation models. The differences between the measurements and the models are explained and calculated. Expansions for the models are proposed to increase the accuracy of the prediction.

After determine the exact moment when the maximum forces occurred during the experiment 2 additions to a force prediction model are made. Both additions focus on assumptions made by all calculation models discussed in this research.

4.1. DETERMINATION OF FAILURE MODE AND CORRESPONDING CALCULATION MODEL

Based on the experiments described in the previous chapter, the most suitable model from chapter 2.3 is determined. Rock failure occurs in either a brittle or a ductile manner. Looking at the rock properties, the ductility number are ranging from 11.29-15.22. According to **Miedema, S.A.** [2014] samples with a ductility number below 9 fail purely in a ductile manner. Above a ductility of 15 the failure is purely brittle. In between these values the failure is a combination of brittle and ductile. So of the 5 samples used, only 1 is considered to fail purely in a brittle manner, while 4 fail in a combination of brittle and ductile. However, the cutting models require a choice in failure mechanism. Therefore the physics during the cutting process are considered.

In the rock cutting process ductile failure will only occur with large confining pressure, for example in large water depths. The experiments in this research are conducted without water, therefore ductile failure is not likely. Plastic deformation in the rock sample is also not observed after analysing the video material of the experiments. Therefore the rock failure in this research is considered to be brittle.

Since the rock failure is a brittle failure mode, it occurs either in a brittle tensile or brittle shear manner. For small cutting depths, failure is usually shear. Only after a certain cutting depth a tensile plane arises. Based on the cutting depths shear failure seems more likely to happen. Taking a look at the particle size distributions show that in every experiment particles below 2mm diameter are cut out. During most experiments these small particle sizes make up to 10-20% of the cut out material, although there are outliers of up to 40%. This indicates the existence of a crushed zone in front of the tip of the pick point. In purely tensile failure this is not likely to happen. Based on physics and measurements neither tensile nor shear failure can be excluded totally. However, the evidence points more towards a shear type. So even though it is still possible that in the top part of the rock some tensile failure might occur, the failure is assumed to be more in a brittle shear manner.

For brittle shear failure 2 cutting force prediction models are elaborated upon in this research: The Nishimatsu Model and The Tear Model. As previously described, the Nishimatsu Model is applicable for every cutting angle, while the Tear Model shows signs of unsuitability for the larger cutting angles. The mobilized cohesion c_m goes to infinitely large values for certain combinations of cutting angle α_c, internal friction angle ϕ and external friction angle δ. Also the shear angle β for the Tear Model decreases to $\beta = 7.5°$. This not only increases the cutting forces tremendously, it is also questionable in a physical sense. The small shear angle indicates a very long shear plane. Therefore The Nishimatsu Model is considered to be the most suitable

force prediction model for the cutting geometry used in this research. The expression for the cutting forces are therefore:

$$F_{h,m} = \frac{1}{n+1} \cdot \frac{2 \cdot c \cdot h_i \cdot w \cdot cos(\phi) \cdot sin(\alpha+\delta)}{1+cos(\alpha+\delta+\phi)} \tag{4.1}$$

$$F_{v,m} = \frac{1}{n+1} \cdot \frac{2 \cdot c \cdot h_i \cdot w \cdot cos(\phi) \cdot cos(\alpha+\delta)}{1+cos(\alpha+\delta+\phi)} \tag{4.2}$$

The depths measured at the point where the maximum forces occurred are substituted into the equations, together with the rock properties. This results in the values for the horizontal and vertical cutting forces for a 2D cutting process. The total cutting force $F_{t,m}$ can be calculated with the following equation:

$$F_{t,m} = \sqrt{F_{h,m}^2 + F_{v,m}^2} \tag{4.3}$$

The shear angle can be calculated by using:

$$\beta = \frac{\pi}{2} - \frac{\alpha_c + \delta + \phi}{2} \tag{4.4}$$

4.2. INDENTATION FORCE PREDICTION MODEL

In all calculation models discussed during this research, including the Nishimatsu Model, it is assumed that the tip of the pick point is sharp. Even though this appears to be reasonable, it turns out to be impractical in reality. First of all, the term sharpness is arbitrary and it depends on the scale and therefore the cutting depth. Secondly, the first cut will already induce wear on the teeth and decrease the sharpness. The force prediction models would then be inapplicable. Since the sharpness depends on the cutting depth, its influence is (probably) negligible after a certain cutting depth is reached. For the small cutting depths used in this research, the sharpness has influence on the cutting forces.

4.2.1. DETERMINATION OF THE INDENTATION FORCES

Therefore an expansion to the Nishimatsu Model, as proposed by **Zhantao Li** [2012], is applied. From experiments on a hollow circular rock sample an addition to the Nishimatsu model is composed. From figure 4.1 it is seen that the size of the bit matches the inner and outer diameter of the rock cylinder.

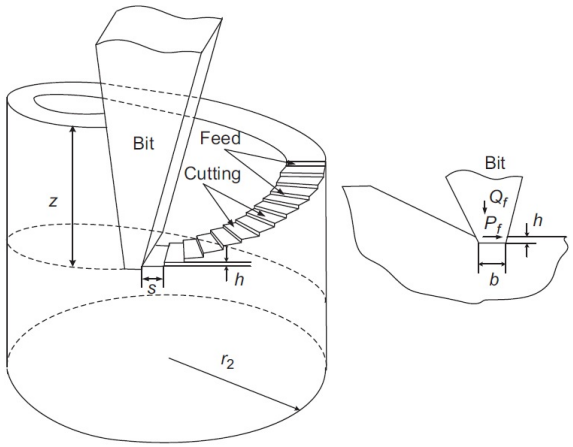

Figure 4.1: Cutting experiments from Zhantao Li (2012)

Figure 4.2 presents the differences in the cutting process between the regular Nishimatsu model and the expansion. While the regular Nishimatsu Model only considers a primary crushed zone in front of the tool, the expansion introduces a secondary crushed zone due to the blunt cutting tool.

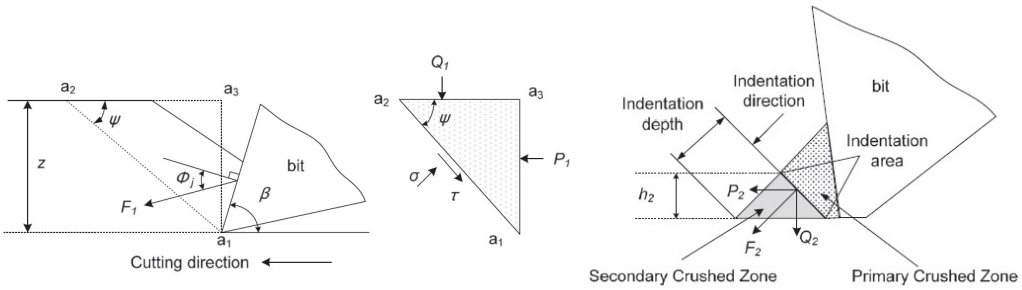

(a) Regular Nishimatsu Model by Zhantao Li(2012) (b) Expanded Nishimatsu Model by Zhantao Li(2012)

Figure 4.2: The regular and expanded Nishimatsu model by Zhantao Li(2012)

Besides the cutting force F_1, a second force F_2 arises due to the removal of the secondary crushed zone. Compared to the cutting force, the indention force F_2 is smaller and more converges to a more or less constant value over the depth. The indention force is defined in equations 4.5 and 4.6, where k_i is a coefficient determined by the size of the secondary crushed zone. For the horizontal part k_1 is used and k_2 for the vertical part. For convenience P_2 is F_{h2} and Q_2 is F_{v2}.

$$P_2 = F_{h2} = k_1 \cdot UCS \tag{4.5}$$

$$Q_2 = F_{v2} = k_2 \cdot UCS \tag{4.6}$$

In the same paper it is stated that the horizontal part of the indention force (P_2) is equivalent to the friction force between the tool and the rock. If this is approached as a dynamic friction problem, the following equation is valid, where F_N represents the normal force and μ the dynamic friction coefficient. Figure 4.3 contains a graphical representation of this assumption. To move the square object from this figure, the cutting force (directed in line with cutting velocity v_c) has to overcome the friction force F_{fric}. The value for the frictional force for the experiments in this research can be found with use of the vertical force during the cutting process. During the experiments the cutting tool is pushed out of the rock sample. However, the tool can not move upwards, so the resistance force has to be equal to the upwards force to keep the vertical forces in equilibrium. It is therefore assumed that the normal force F_N is in fact equal to the measured vertical force, but pointed downwards instead of upwards. A value for the dynamic friction coefficient μ is provided by **Defence Nuclear Agency** [1976], who conducted experiments to determine the dynamic friction coefficient between several specimen and steel. Their research determined that the dynamic friction coefficient μ for dry sandstone is 0.39. The final expression for F_{h2} becomes:

$$F_{h2} = k_1 \cdot UCS = F_N \cdot \mu = F_v \cdot 0.39 \tag{4.7}$$

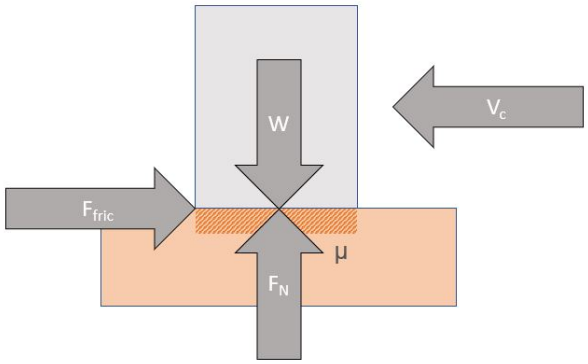

Figure 4.3: Representation of the dynamic friction assumption

The expression for the vertical component of the indention force can be found by doing a similar derivation. However, one could also use geometric relations in the cutting process. If figure 4.2b is considered again, one could argue that the indention direction will act on the shear plane created by the cut out rock pieces. With this shear angle known from the cutting model, simple geometry can be applied to rewrite the expression for F_{h2} in an expression for F_{v2}.

$$F_{v2} = \frac{F_{h2}}{tan(\beta)} \tag{4.8}$$

The horizontal and vertical components of the indention forces become:

$$F_{h2} = F_v \cdot 0.39 \tag{4.9}$$

$$F_{v2} = \frac{F_v \cdot 0.39}{tan(\beta)} \tag{4.10}$$

With shear angle β determined by the Nishimatsu Model:

$$\beta = \frac{\pi}{2} - \frac{\alpha_c + \delta + \phi}{2} \tag{4.11}$$

The total friction force can finally be calculated by using:

$$F_{t,2} = \sqrt{F_{h,2}^2 + F_{v,2}^2} \tag{4.12}$$

The values for the indentation forces due to wear of the cutting tool can be determined, but since this can only be calculated after doing experiments the applicability is limited. Therefore a relation between the rock properties, experimental settings and frictional forces is necessary. This enables an approximation these forces before any experiment is conducted. To do so, the frictional forces are plotted against the cutting depth. Next a polynomial fit is plotted through the data points. The subscript i in S_i represents the number of the sample and α_c is the cutting angle used in the experiments.

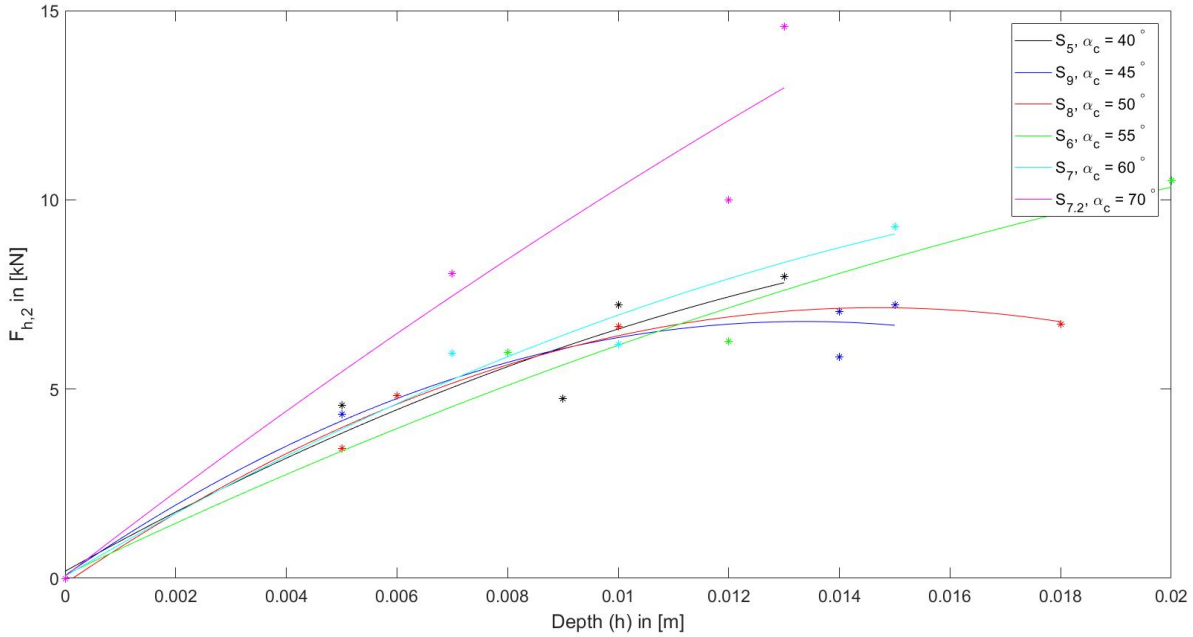

Figure 4.4: Horizontal component of the indentation force over the cutting depth

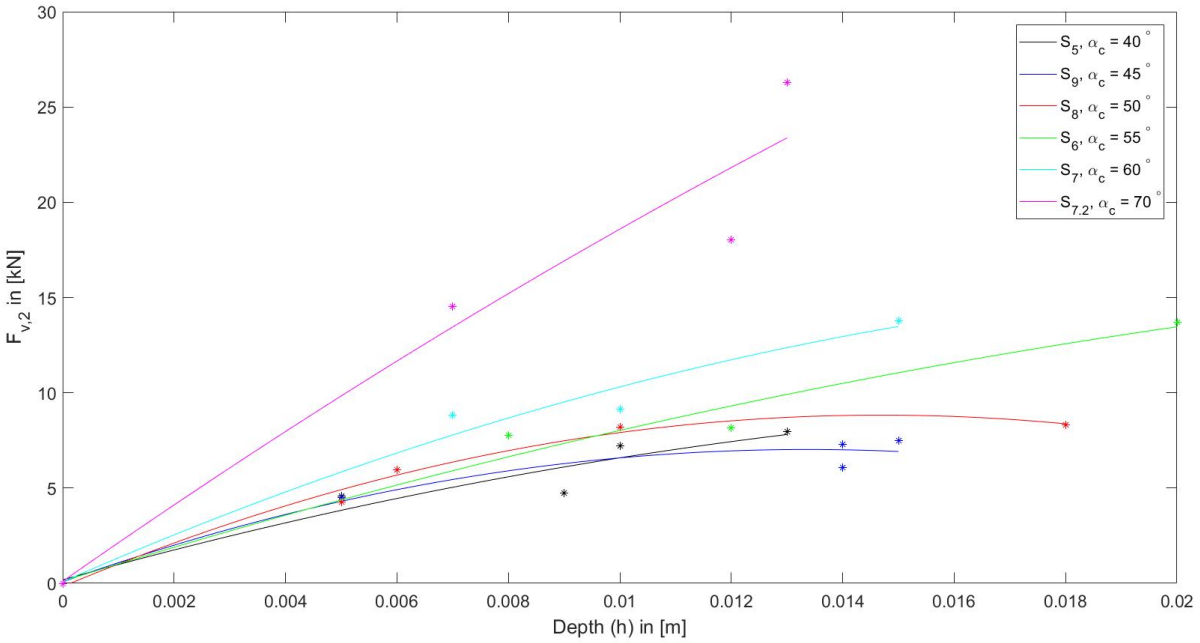

Figure 4.5: Vertical component of the indentation force over the cutting depth

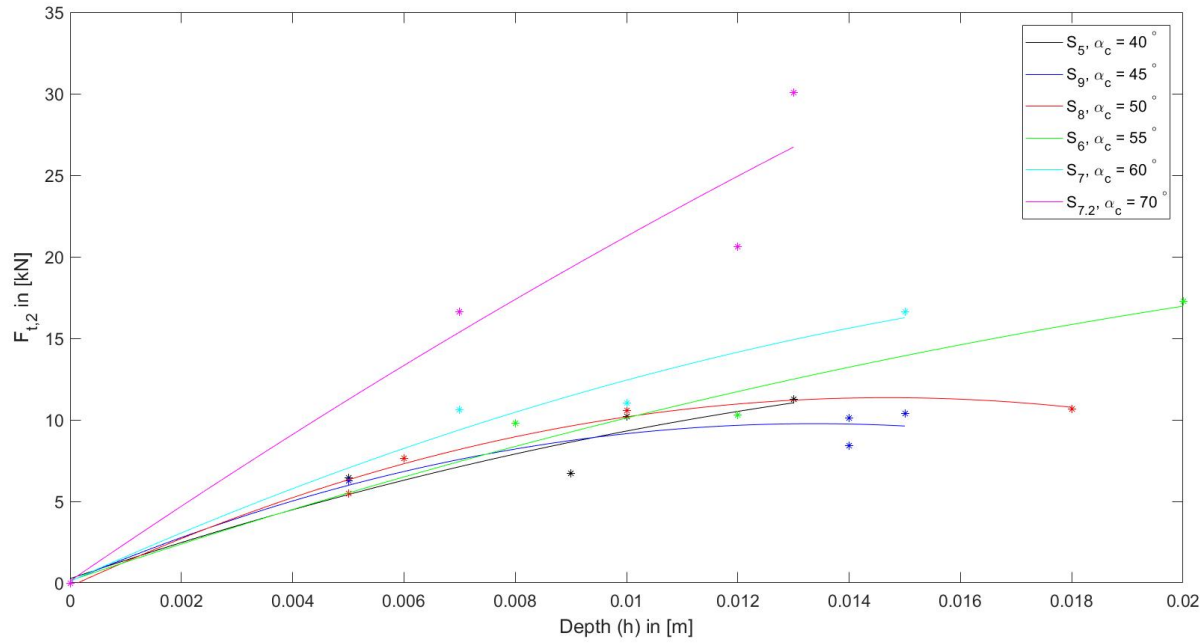

Figure 4.6: Total indentation force over the cutting depth

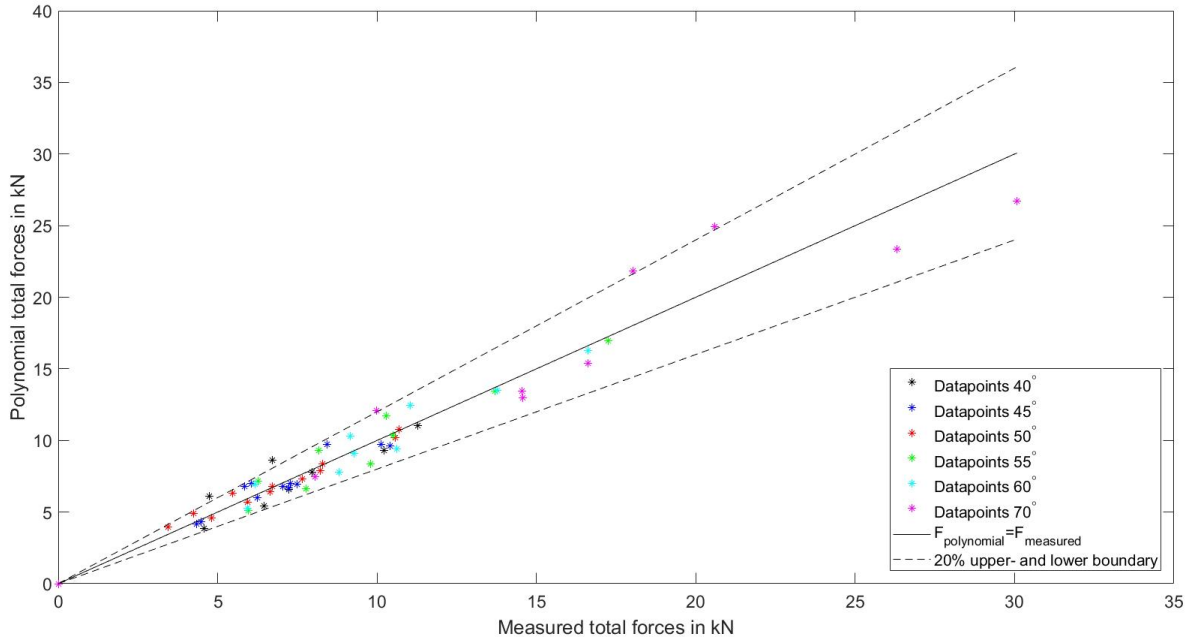

Figure 4.7: Polynomial fit compared with the measured forces

In figure 4.7 the results of the polynomial fit are compared with the measured forces. The solid line represents the values for which the polynomial fit and the measured forces are equal. The dashed lines represent the 20% upper and lower boundary. Most of the data points lay within this error margin. Some scatter is visible, however the data points follow the expected trend; a gradually declining increase until a constant value is reached, which is backed up by the earlier mentioned research by **Zhantao Li** [2012]. It is not surprising that there is some scatter, rock is a heterogeneous material where some parts might be more denser and harder than other parts of the same sample. Also the presence of pre-existing cracks through the sample is an explanation for the deviation in the values.

4.2.2. DERIVATION OF INDENTATION FORCE PREDICTION MODEL

The rock properties that determine the indention resistance are the compressive strength (UCS) and the internal friction angle. The relevant cutting variables are the cutting depth, the cutting angle and the width of the pick point. From information gathered from personal communication (**Miedema** [2018]) it is learned that a commonly used rule of thumb for calculating the indention resistance of rock is $3 \cdot UCS$ multiplied with an area. The area in this case would be the indention area, but this is unknown. However the $3 \cdot UCS$ term should be included considering its relevance (indicated with A in formula 4.13). A squared length scale is necessary to get the units correctly and since the influence of the cutting depth on the indentation force it is chosen to implement an h_i^2 term to the equation. If the cutting depth increases, the secondary crushed zone gets time to develop until a certain limit is reached. Therefore the cutting depth should be implemented in a way that an larger depth gives larger forces, hence the h_i^2 term (indicated with B in formula 4.13). The width of the cutting tool, in this case a pick point, clearly plays a role in in the indention area and must be included in the formula. To get the units correct, the width of the tool is divided by the depth of the cut $\frac{w}{h_i}$. The implementation of the h_i^2 gave the equation an exponentially growing form. To counteract this curvature the $\frac{w}{h_i}$ is given a power ($\frac{5}{4}$) (indicated with C in formula 4.13). Finally a coefficient c_f is added to calibrate the outcome of the formula. The remaining relevant properties such as cutting angle and internal friction angle are implemented within this coefficient since it is based on the shear angle (indicated with D in formula 4.13). The result of the proposed equations is shown below. Since the direction of indentation is assumed to be equal to the shear angle, geometric rules are applied to the expression for the total force to calculate the horizontal and vertical component.

$$F_{t,2} = \overbrace{3 \cdot UCS}^{A} \cdot \underbrace{h_i^2}_{B} \cdot \overbrace{\left(\frac{w}{h_i}\right)^{\frac{5}{4}}}^{C} \cdot \underbrace{c_f}_{D} \tag{4.13}$$

$$F_{h,2} = 3 \cdot UCS \cdot h_i^2 \cdot \left(\frac{w}{h_i}\right)^{\frac{5}{4}} \cdot c_f \cdot cos(\beta) \tag{4.14}$$

$$F_{v,2} = 3 \cdot UCS \cdot h_i^2 \cdot \left(\frac{w}{h_i}\right)^{\frac{5}{4}} \cdot c_f \cdot sin(\beta) \tag{4.15}$$

The six datasets (40°, 45°, 50°, 55°, 60° and 70°) each had a certain value for c_f for which the formula fitted best on the data points. In figure 4.8 the value of c_f is plotted over the tan(β). Next a 2^{nd} degree polynomial is fitted. The equation of this line gives the final expression for c_f (equation 4.16).

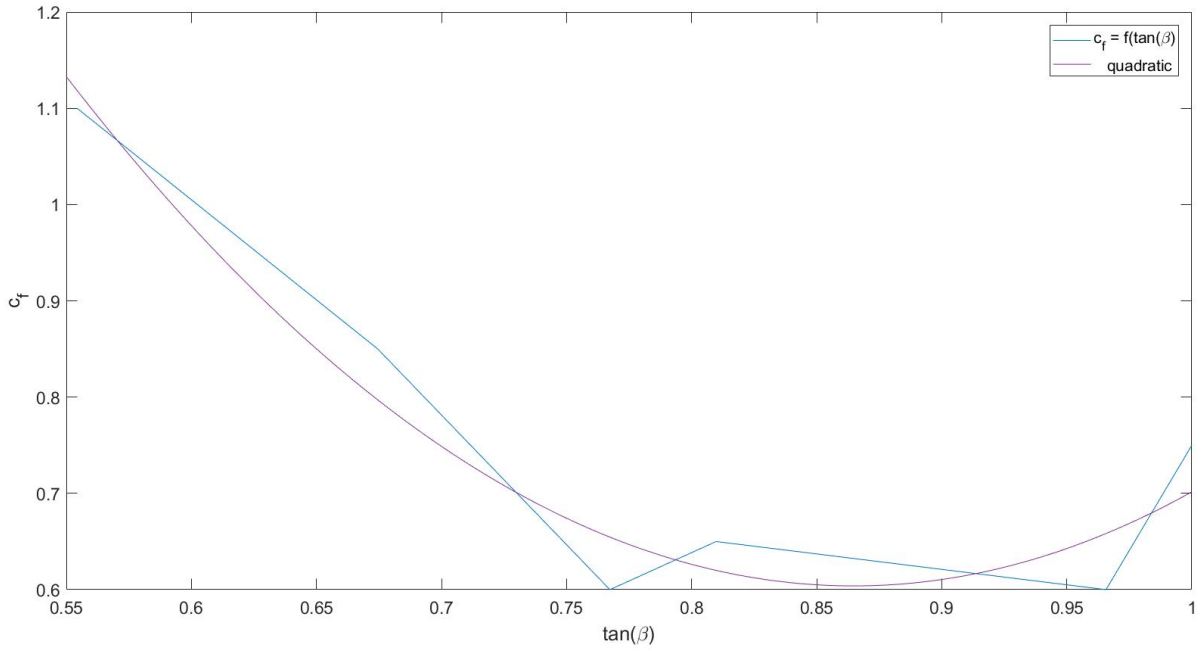

Figure 4.8: c_f over tan(β) graph including the 2^{nd} degree polynomial fit

$$c_f = 5.3 \cdot tan^2(\beta) - 9.2 \cdot tan(\beta) + 4.6 \tag{4.16}$$

The norm of residuals for the fit of the 2^{nd} degree polynomial on the data points in the c_f over tan(β) graph is 0.11294, which negligible. This shows the high accuracy of the approximation for c_f. To visualize the accuracy of the composed formula, the formula is plotted together with the measured data points. All datasets are plotted separately in appendix .32.

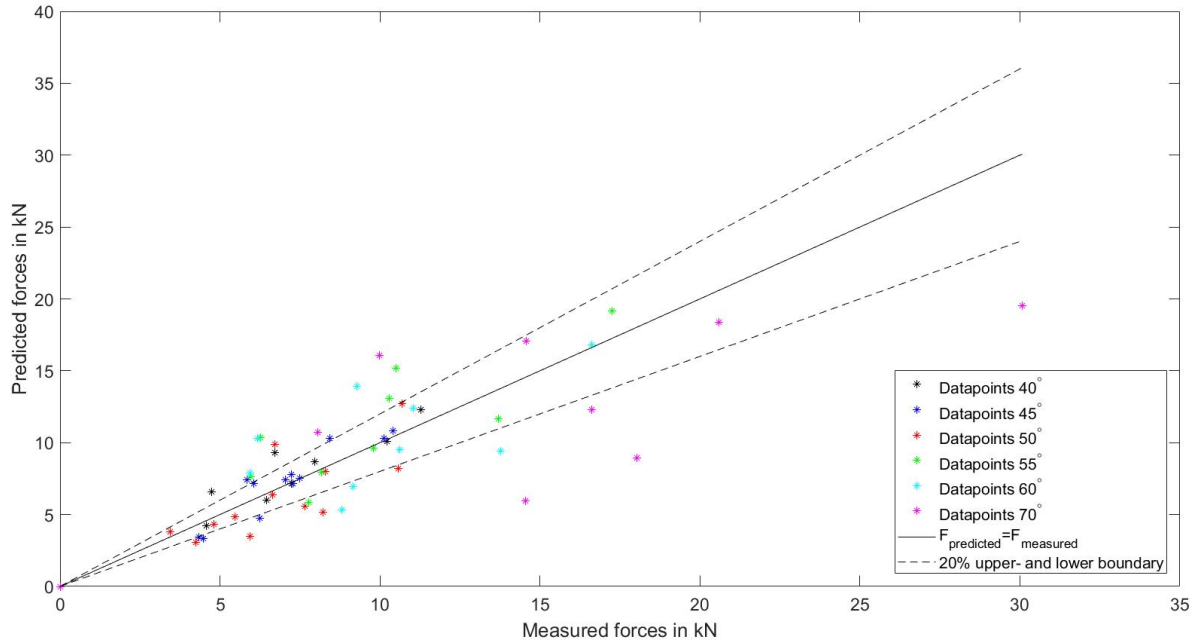

Figure 4.9: Formula compared with the measured forces

In figure 4.9 the predicted indentation force with the formula is compared with the measured indentation force. It shows that for for data points the accuracy lay within the 20% error margin. The only real exception is the data points at the 70° cutting angle. This was already noticeable in figures 4.4, 4.5 and 4.6. The best 2^{nd} degree polynomial fit differs already from the measured data. To investigate this more, the 70° dataset is plotted together with the polynomial fit and the proposed formula:

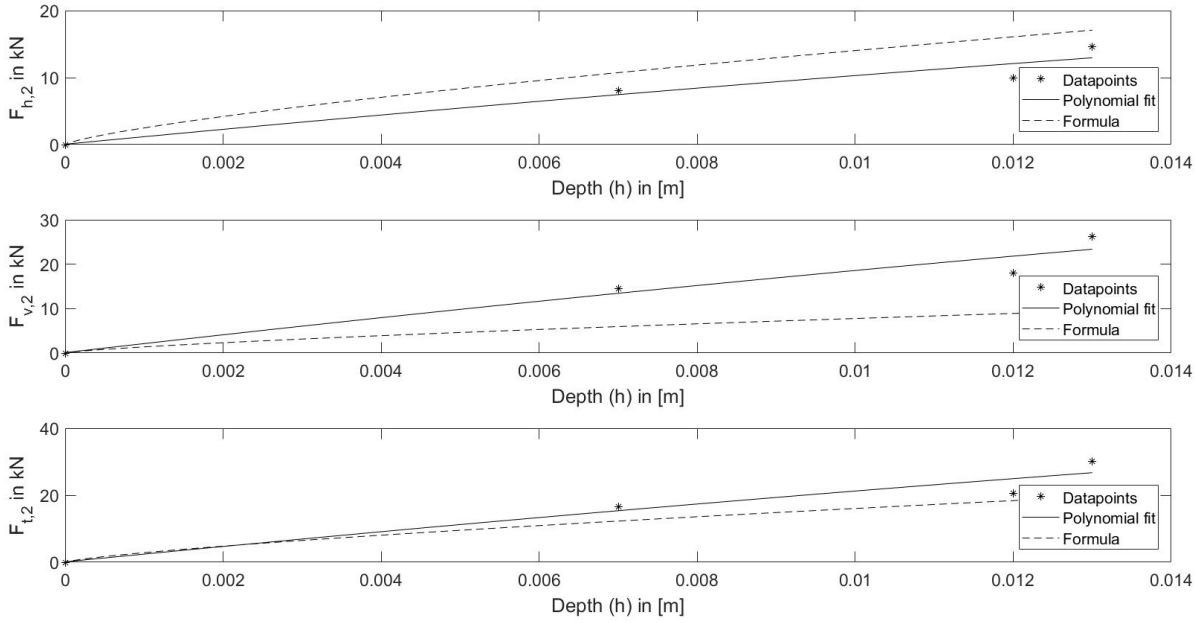

Figure 4.10: Formula compared with the 70° dataset

From figure 4.10 the differences in the formula and measured data is clearly visualized. Even though the horizontal forces are predicted pretty accurately, the vertical forces (and therefore also the total force) are underestimated heavily. This could be due to the large cutting angle. More research into this topic is therefore necessary.

A note has to be made considering the maximum indention force. As mentioned earlier, the secondary crushed zone needs some time (hence depth) to develop. At a certain moment the secondary crushed zone is fully developed and a maximum indention force is reached (as seen in figures 4.4. 4.5 and 4.6). Although the exact depth at which this occurs is uncertain, an estimation of the maximum indention force can be composed. From the rule of thumb a $3 \cdot ucs$ is definitely included. This must be multiplied with the maximum indentation area (A_{ind}) to get the maximum indentation force. The area of the indentation has a width comparable with the width of the cutting tool (w). The height of this area (h_{ind}) depends on the rock properties and cutting settings and is limited to a certain maximum $h_{ind,max}$.

$$F_{t,2,max} = 3 \cdot UCS \cdot A_{ind} = 3 \cdot UCS \cdot w \cdot h_{ind,max} \tag{4.17}$$

$$F_{h,2,max} = F_{t,2,max} \cdot cos(\beta) \tag{4.18}$$

$$F_{v,2,max} = F_{t,2,max} \cdot sin(\beta) \tag{4.19}$$

An expression for the height of the indentation area h_{ind} can be derived based on the proposed formula:

$$F_{t,2} = F_{t,2,max} \tag{4.20}$$

$$3 \cdot UCS \cdot h_i^2 \cdot \left(\frac{w}{h_i}\right)^{\frac{5}{4}} \cdot c_f = 3 \cdot UCS \cdot w \cdot h_{ind} \tag{4.21}$$

$$h_{ind} = c_f \cdot h_i^2 \cdot \left(\frac{w^{\frac{1}{4}}}{h_i^{\frac{5}{4}}}\right) < h_{ind,max} \tag{4.22}$$

4.3. SHEAR FORCE PREDICTION MODEL

To thoroughly understand the 3D components in the linear cutting process, the assumption of a 2D process is analysed first. In 2D only the horizontal and vertical direction are included. The model assumes that the width of the cut is equal to the width of the pick point and remains constant throughout the experiment. The main failure mode is brittle shear failure, which implies the existence of a shear plane over which the rock pieces break out. Figure 4.11a presents the side view where the shear plane is portrayed, where β is the shear angle and L the shear length. From the front view in figure 4.11b the 2D assumption is clearly visible. The cut has a width equal to the width of the pick point w and h is the depth of the cut. The top view shows again the length of the shear plane and the width of the cut. In this case the shear plane is portrayed at the start of the experiment. One should keep in mind that the shear plane travels in front of the tip of the pick point through the rock sample. Since the cutting force prediction models calculate the maximum forces, the shear plane of interest is the one that occurs at that moment. Therefore the position of the shear plane can be anywhere in the rock sample.

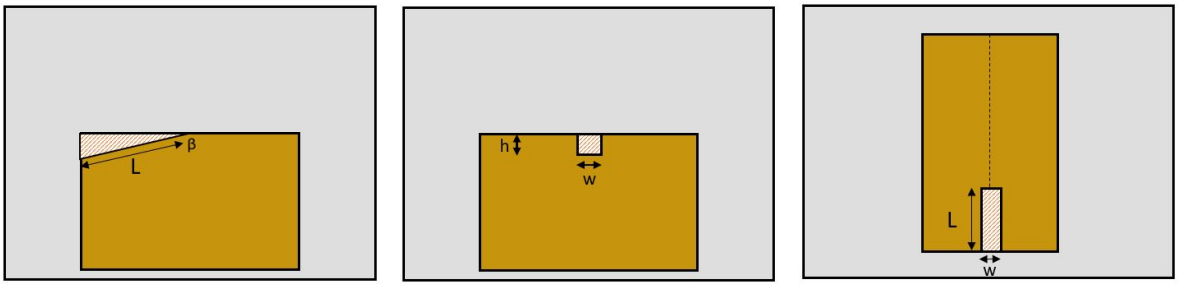

(a) Side view (b) Front view (c) Top view

Figure 4.11: Geometry of the shear plane as assumed by Nishimatsu model

4.3.1. DETERMINATION OF THE SHEAR FORCES

In reality however, the 2D assumption is not valid since sideways out breaking of rock pieces is observed, which makes it a 3D problem. The Nishimatsu model calculates the force required to initiate the shear plane, but the additional shearing due to the sideways out breaking is not included. Figure 4.12a shows the side view of the shear plane as observed during the experiments. From this point of view there is no difference with the 2D case. The front view of the rock sample in figure 4.12b illustrates the sideways out breaking: the width of the cut w_c is wider than the width of the pick point w. The shearing of the created chip over the area on both sides of the gully created by the pick point is responsible for the extra shearing forces. Figure 4.12c portrays the top view of the shear plane. In the case the width of the cut $w_{c1} < w_{c2}$, but this is in fact arbitrary. This differed per experiment.

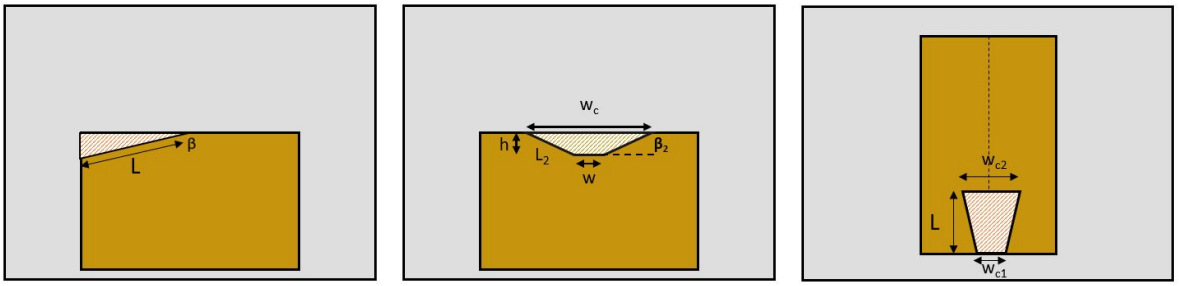

(a) Side view (b) Front view (c) Top view

Figure 4.12: Geometry of the shear plane during experiments

With use of figure 4.12b the expressions for outbreaking angles β_1 and β_2 are derived:

$$\beta_1 = \arctan\left(\frac{h}{\frac{w_{c1}-w}{2}}\right) \tag{4.23}$$

$$\beta_2 = \arctan\left(\frac{h}{\frac{w_{c2}-w}{2}}\right) \tag{4.24}$$

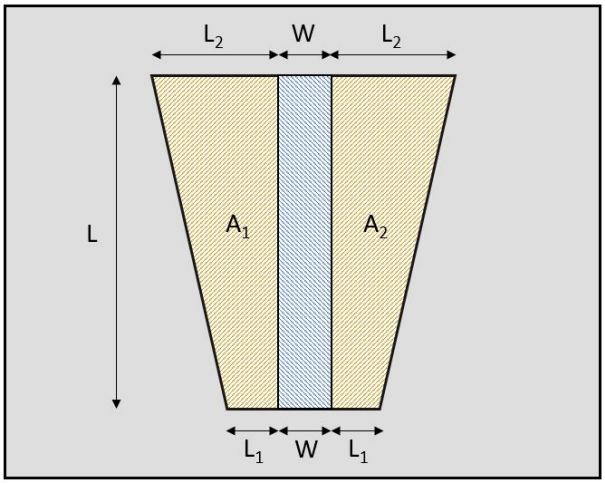

Figure 4.13: Detailed schematization of shear area

Combining figure 4.12b and 4.13 gives expressions for the length of length of the shear area L_1 and L_2, which are then used to calculate the total shear area.

$$L_1 = \sqrt{h^2 + \left(\frac{w_{c1}-w}{2}\right)^2} \tag{4.25}$$

$$L_2 = \sqrt{h^2 + \left(\frac{w_{c2}-w}{2}\right)^2} \tag{4.26}$$

$$A = A_1 + A_2 = 2 \cdot \left(L_1 \cdot L + \frac{L \cdot (L_2 - L_1)}{2}\right) \tag{4.27}$$

Finally the expression for the total force $F_{t,3}$ is found. Since the failure mechanism is shearing, the total area of the shear plane is multiplied with the cohesion of the material. Cohesion is the property that delivers the shearing resistance within the rock.

$$F_{t,3} = A \cdot c \tag{4.28}$$

The shear force depends only on the area of the shear plane and the cohesion of the material. The cohesion can usually be approximated pretty accurately, so the area of the shear plane is the only variable. From the depth and width profiles the area of the cut is calcuated and it is observed that the area increases over depth and therefore the forces increase as well. So the hypothesis is that the shear area depends on the cutting depth. To examine this more closely, the areas are plotted over the depth, where the sets of experiments are separated by cutting angle (figure 4.14). Next a polynomial is fitted through the data points.

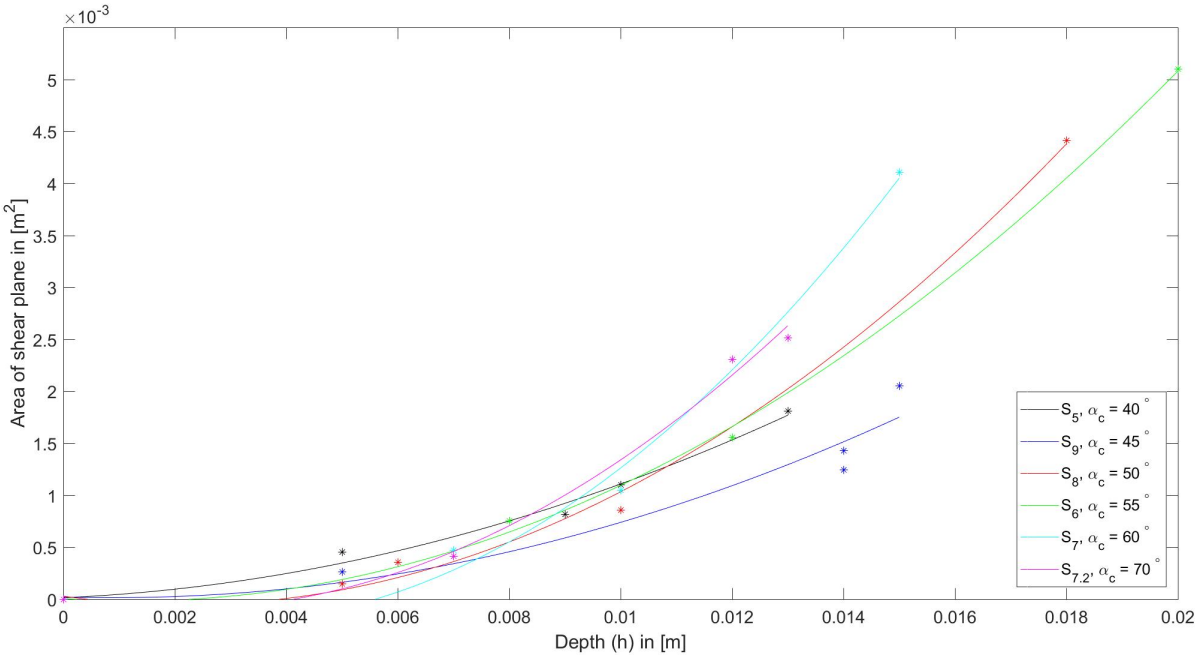

Figure 4.14: Area of the shear plane over the cutting depth

All graphs from figure 4.14 show quadratic behaviour. It seems safe to assume that the area of the shear plane increases quadratically with the depth. Since the internal friction angle and external friction angle of the used rock samples are all equal, the differences in the graphs are due to the varying cutting angles. Before any prediction formula is constructed, the accuracy of the 2^{nd} degree polynomial is checked.

From figure 4.15 it is clearly seen that the polynomial fits the data points with a 20% error margin. This indicates that a $2^n d$ degree formula is potentially accurate enough to predict the area of the shear plane.

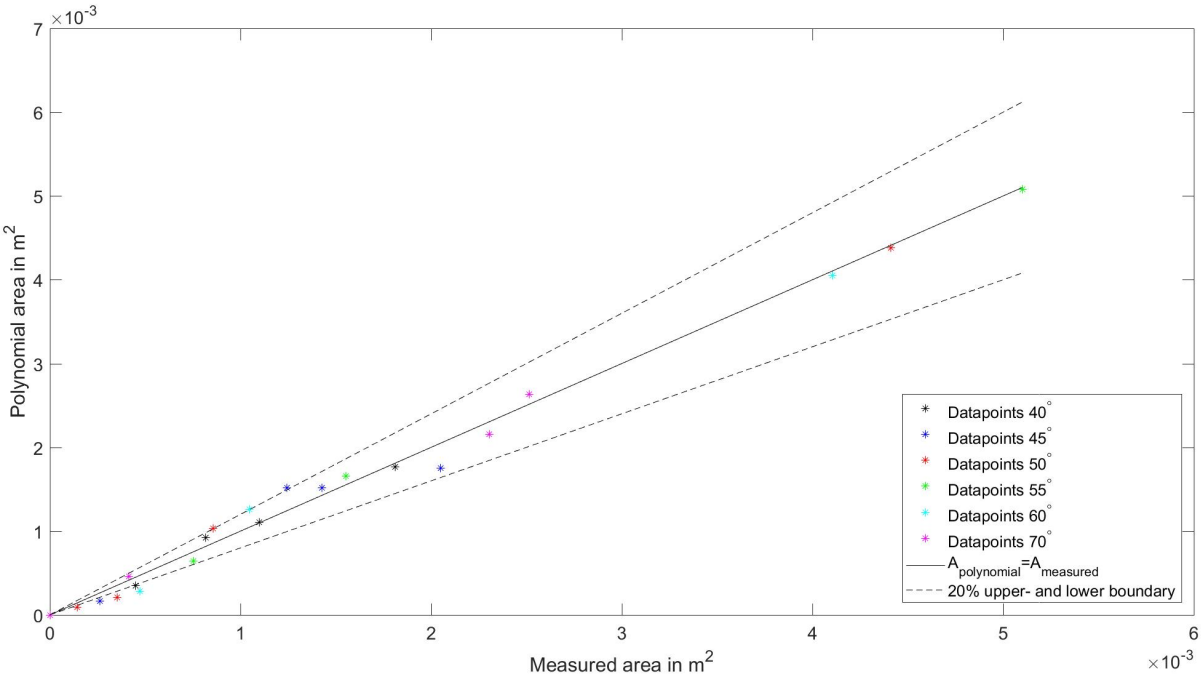

Figure 4.15: Polynomial fit compared with the measured area of the shear plane

4.3.2. DERIVATION OF SHEAR FORCE PREDICTION MODEL

The relevant properties for the shear area (A) are identified to be the cutting depth and the cutting angle. To include the internal friction angle as well (even though every sample has a similar internal friction angle), the shear angle is implemented in the formula. From figure 4.15 it is shown that the shear area increases quadratically with the depth (indicated with A in formula 4.29). Figure 4.15 further shows that the shear area increases stronger with a higher cutting angle, hence a lower shear angle. The lower the angle, the stronger the increase with depth: so the cosine of the shear angle needs to be included (indicated with B in formula 4.29). Finally a coefficient c_a is implemented. C_a is determined empirically and is indicated with C in formula 4.29.

$$A = \overbrace{c_a}^{C} \cdot \underbrace{cos(\beta)}_{B} \cdot \overbrace{h_i^2}^{A} \tag{4.29}$$

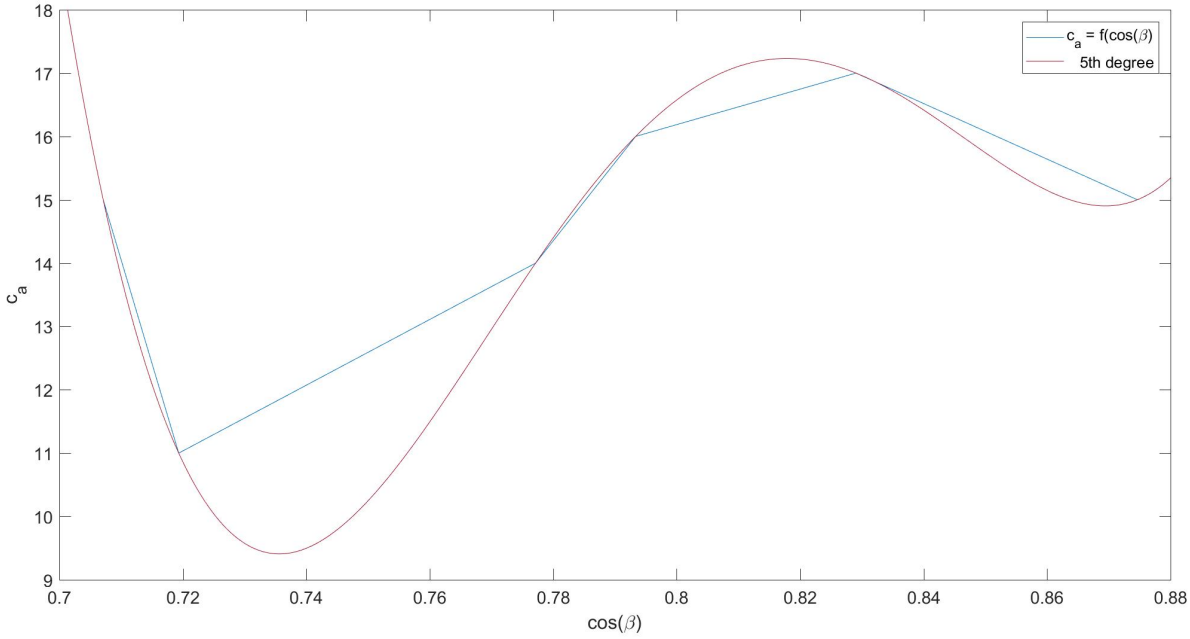

Figure 4.16: c_a over cos(β) graph including the 5^{th} degree polynomial fit

The 5^{th} degree polynomial to determine coefficient c_a based on $cos(\beta)$ is given by the formula below. The norm of residuals is $1.627 \cdot 10^{-10}$.

$$c_a = 87759 \cdot cos^5(\beta) - 1.2287 \cdot 10^5 \cdot cos^4(\beta) - 1.7617 \cdot 10^5 \cdot cos^3(\beta) + 4.4329 \cdot 10^5 \cdot cos^2(\beta) - 2.9904 \cdot 10^5 \cdot cos(\beta) + 67313 \tag{4.30}$$

To examine the accuracy of the proposed formula, the formula, polynomial fit and data points are plotted together in appendix .32. The accuracy of the formula is presented in figure 4.17.It is seen that the prediction for the shear area has an error margin of around 20%. The final expression for the force due to the 3D shearing effects becomes:

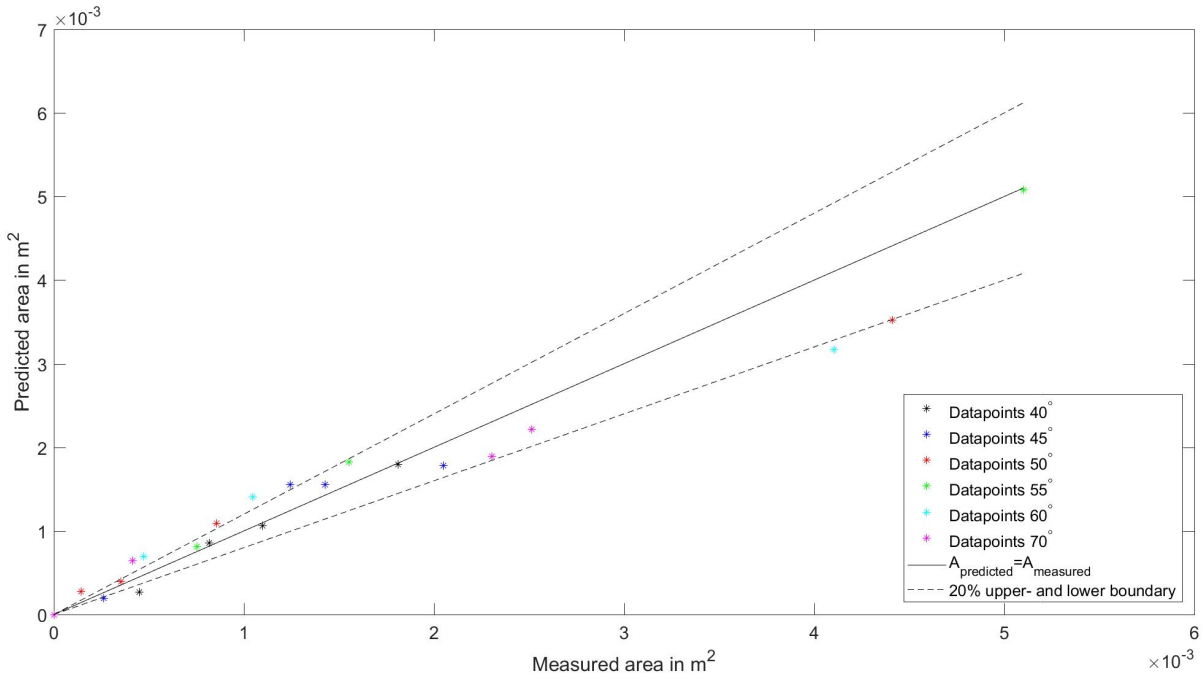

Figure 4.17: Formula compared with the measured area of the shear plane

$$F_{t,3} = A \cdot c = c_a \cdot cos(\beta) \cdot h_i^2 \cdot c \tag{4.31}$$

$$F_{h,3} = c_a \cdot cos(\beta) \cdot h_i^2 \cdot c \cdot cos(\beta) \tag{4.32}$$

$$F_{v,3} = c_a \cdot cos(\beta) \cdot h_i^2 \cdot c \cdot sin(\beta) \tag{4.33}$$

Where c is the cohesion of the rock and c_a is given by:

$$c_a = 87759 \cdot cos^5(\beta) - 1.2287 \cdot 10^5 \cdot cos^4(\beta) - 1.7617 \cdot 10^5 \cdot cos^3(\beta) + 4.4329 \cdot 10^5 \cdot cos^2(\beta) - 2.9904 \cdot 10^5 \cdot cos(\beta) + 67313 \tag{4.34}$$

4.4. COMPARE PREDICTIONS WITH MEASURED CUTTING FORCES

Substituting all rock - and cutting properties into the proposed formula's give the predicted cutting forces. Tables 4.1, 4.2 and 4.3 contain all predicted forces and the actual measured forces. The forces calculated by the Nishimatsu model are indicated with $F_{h,m}$, $F_{v,m}$ and $F_{t,m}$ for the horizontal, vertical and total force component. The expansion for the indentation forces are denoted with $F_{h,2}$, $F_{v,2}$ and $F_{t,2}$, while $F_{h,3}$, $F_{v,3}$ and $F_{t,3}$ refer to the shear force expansions. The combined horizontal, vertical and total cutting forces (F_h, F_v and F_t) are calculated with equations 4.35, 4.36 and 4.37. These values are then compared to the actual measured forces. An extra remark for the total forces: to calculate these, one should take the square root of the horizontal force squared plus the vertical force squared instead of adding up all total force components. These total force components are acting in a different direction and therefore can not be added up.

$$F_h = F_{h,m} + F_{h,2} + F_{h,3} \tag{4.35}$$

$$F_v = F_{v,m} + F_{v,2} + F_{v,3} \tag{4.36}$$

$$F_t = \sqrt{F_h^2 + F_v^2} \tag{4.37}$$

After adding the indentation force and the shear force to the Nishimatsu model, the total expressions for the horizontal, vertical and total cutting force become:

$$F_h = \overbrace{\frac{1}{n+1} \cdot \frac{2 \cdot c \cdot h_i \cdot w \cdot cos(\phi) \cdot sin(\alpha_c + \delta)}{1 + cos(\alpha_c + \delta + \phi)}}^{F_{h,m}} + \overbrace{3 \cdot UCS \cdot h_i^2 \cdot \left(\frac{w}{h_i}\right)^{\frac{5}{4}} \cdot c_f \cdot cos(\beta)}^{F_{h,2}}$$

$$\overbrace{+c_a \cdot cos(\beta) \cdot h_i^2 \cdot c \cdot cos(\beta)}^{F_{h,3}} \tag{4.38}$$

$$F_v = \overbrace{\frac{1}{n+1} \cdot \frac{2 \cdot c \cdot h_i \cdot w \cdot cos(\phi) \cdot cos(\alpha_c + \delta)}{1 + cos(\alpha_c + \delta + \phi)}}^{F_{v,m}} + \overbrace{3 \cdot UCS \cdot h_i^2 \cdot \left(\frac{w}{h_i}\right)^{\frac{5}{4}} \cdot c_f \cdot sin(\beta)}^{F_{v,2}}$$

$$\overbrace{+c_a \cdot cos(\beta) \cdot h_i^2 \cdot c \cdot sin(\beta)}^{F_{v,3}} \tag{4.39}$$

$$F_t = \sqrt{F_h^2 + F_v^2} \tag{4.40}$$

With:

$$c_f = 5.3 \cdot tan^2(\beta) - 9.2 \cdot tan(\beta) + 4.6 \tag{4.41}$$

$$c_a = 87759 \cdot cos^5(\beta) - 1.2287 \cdot 10^5 \cdot cos^4(\beta) - 1.7617 \cdot 10^5 \cdot cos^3(\beta) + 4.4329 \cdot 10^5 \cdot cos^2(\beta)$$

$$-2.9904 \cdot 10^5 \cdot cos(\beta) + 67313 \tag{4.42}$$

After substituting all values in the proposed formulas, the predicted horizontal forces can be compared with the measured horizontal forces.

Table 4.1: Calculated horizontal force components compared with the measured horizontal forces

	$F_{h,m}$ [kN]	$F_{h,2}$ [kN]	$F_{h,3}$ [kN]	F_h [kN]	$F_{h,measured}$ [kN]
Experiment 5A	0.46	4.24	1.03	5.73	9.78
Experiment 5B	0.91	7.13	4.12	12.16	15.96
Experiment 5C	1.19	8.69	6.96	16.84	22.40
Experiment 5D	0.82	6.59	3.33	10.74	10.86
Experiment 9A	0.51	3.42	0.80	4.73	10.05
Experiment 9B	1.44	7.41	6.26	15.11	19.18
Experiment 9C	1.44	7.41	6.26	15.11	21.46
Experiment 9D	1.54	7.79	7.19	16.52	19.46
Experiment 8A	0.58	3.78	1.08	5.44	6.91
Experiment 8B	1.16	6.36	4.31	11.83	16.91
Experiment 8C	2.08	9.88	13.95	25.91	22.07
Experiment 8D	0.70	4.34	1.55	6.59	10.95
Experiment 6A	0.98	7.65	3.14	11.77	14.87
Experiment 6B	1.47	10.36	7.08	18.91	17.81
Experiment 6C	2.45	15.20	19.68	37.33	28.31
Experiment 7A	1.22	7.87	3.31	12.40	13.58
Experiment 7B	1.74	10.28	6.76	18.78	13.63
Experiment 7C	2.61	13.93	15.21	31.75	24.49
Experiment 7.2A	1.64	10.74	3.25	15.63	14.34
Experiment 7.2B	2.81	16.09	9.55	28.45	24.04
Experiment 7.2C	3.05	17.09	11.22	31.36	32.54

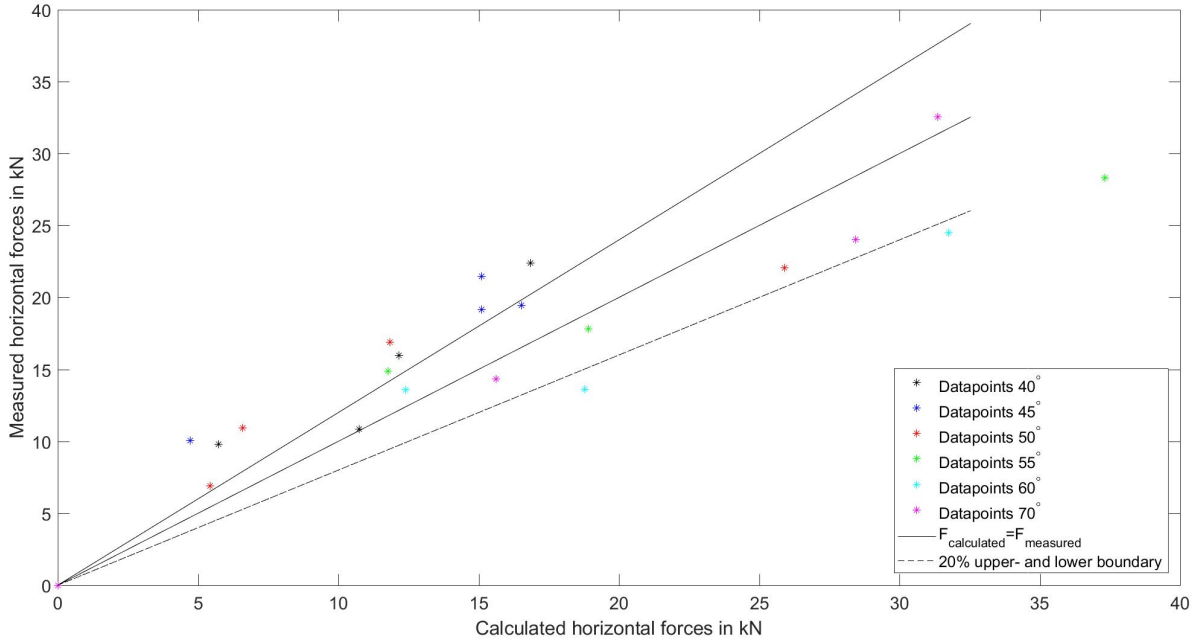

Figure 4.18: Predicted horizontal forces compared with measured horizontal forces

Also the vertical component of the predicted forces is compared with the measured vertical forces.

Table 4.2: Calculated vertical force components compared with the measured vertical forces

	$F_{v,m}$ [kN]	$F_{v,2}$ [kN]	$F_{v,3}$ [kN]	F_v [kN]	$F_{v,measured}$ [kN]
Experiment 5A	0.26	4.24	1.03	5.53	11.72
Experiment 5B	0.53	7.13	4.11	11.77	18.54
Experiment 5C	0.69	8.69	6.95	16.33	20.44
Experiment 5D	0.48	6.59	3.33	10.40	12.19
Experiment 9A	0.25	3.30	0.77	4.32	11.12
Experiment 9B	0.70	7.15	6.05	13.90	18.04
Experiment 9C	0.70	7.15	6.05	13.90	18.53
Experiment 9D	0.75	7.53	6.94	15.22	15.01
Experiment 8A	0.20	3.06	0.87	4.13	8.81
Experiment 8B	0.40	5.11	3.48	8.99	17.05
Experiment 8C	0.72	8.00	11.30	20.02	17.35
Experiment 8D	0.24	3.51	1.26	5.01	12.37
Experiment 6A	0.26	5.87	2.41	8.54	15.32
Experiment 6B	0.39	7.95	5.43	13.77	16.08
Experiment 6C	0.66	11.66	15.10	27.42	26.95
Experiment 7A	0.19	5.30	2.23	7.72	15.84
Experiment 7B	0.28	6.93	4.56	11.77	15.23
Experiment 7C	0.41	9.40	10.25	11.06	23.83
Experiment 7.2A	-0.03	5.95	1.80	7.72	20.67
Experiment 7.2B	-0.05	8.92	5.30	14.17	25.61
Experiment 7.2C	-0.05	9.47	6.22	15.64	37.39

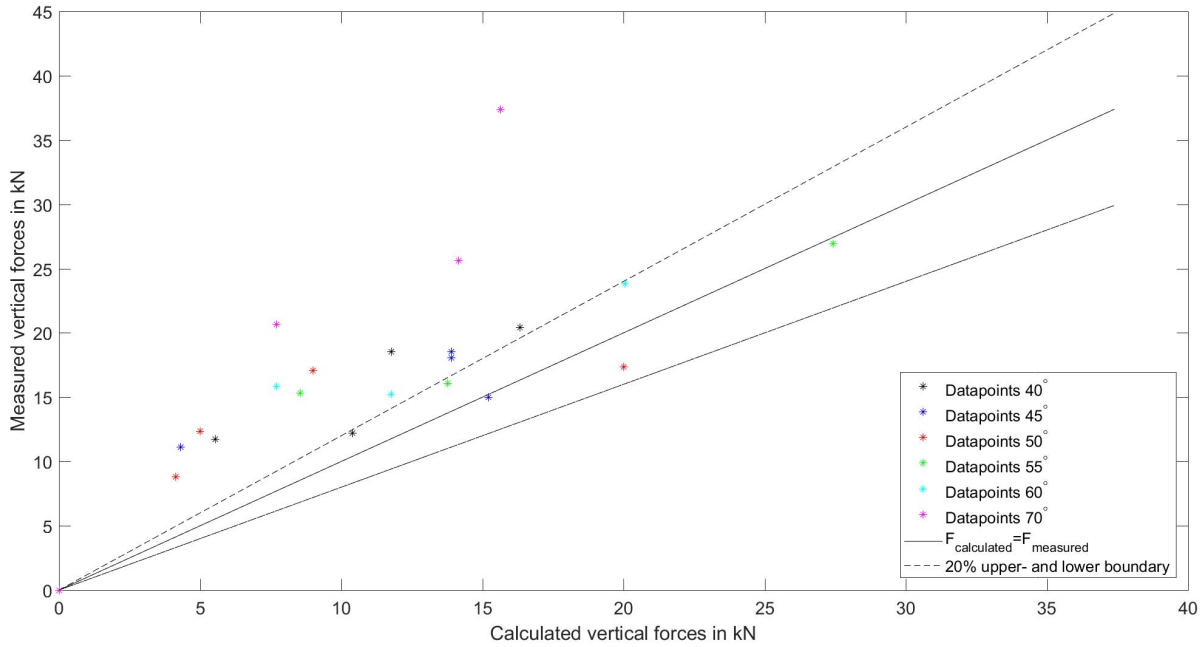

Figure 4.19: Predicted vertical forces compared with measured vertical forces

Finally the total forces are calculated with use of formula 4.37 and compared with the measured total forces.

Table 4.3: Calculated total forces compared with the measured total forces

	F_t [kN]	$F_{t,measured}$ [kN]
Experiment 5A	7.97	14.98
Experiment 5B	16.92	24.22
Experiment 5C	23.45	30.35
Experiment 5D	14.95	15.53
Experiment 9A	6.40	14.81
Experiment 9B	20.53	25.58
Experiment 9C	20.53	26.59
Experiment 9D	22.46	23.58
Experiment 8A	6.83	10.81
Experiment 8B	14.86	24.01
Experiment 8C	32.74	28.08
Experiment 8D	8.28	15.88
Experiment 6A	14.54	17.54
Experiment 6B	23.39	20.98
Experiment 6C	46.31	34.02
Experiment 7A	14.61	19.60
Experiment 7B	22.16	18.62
Experiment 7C	37.56	28.00
Experiment 7.2A	17.43	22.80
Experiment 7.2B	31.78	27.25
Experiment 7.2C	35.04	37.81

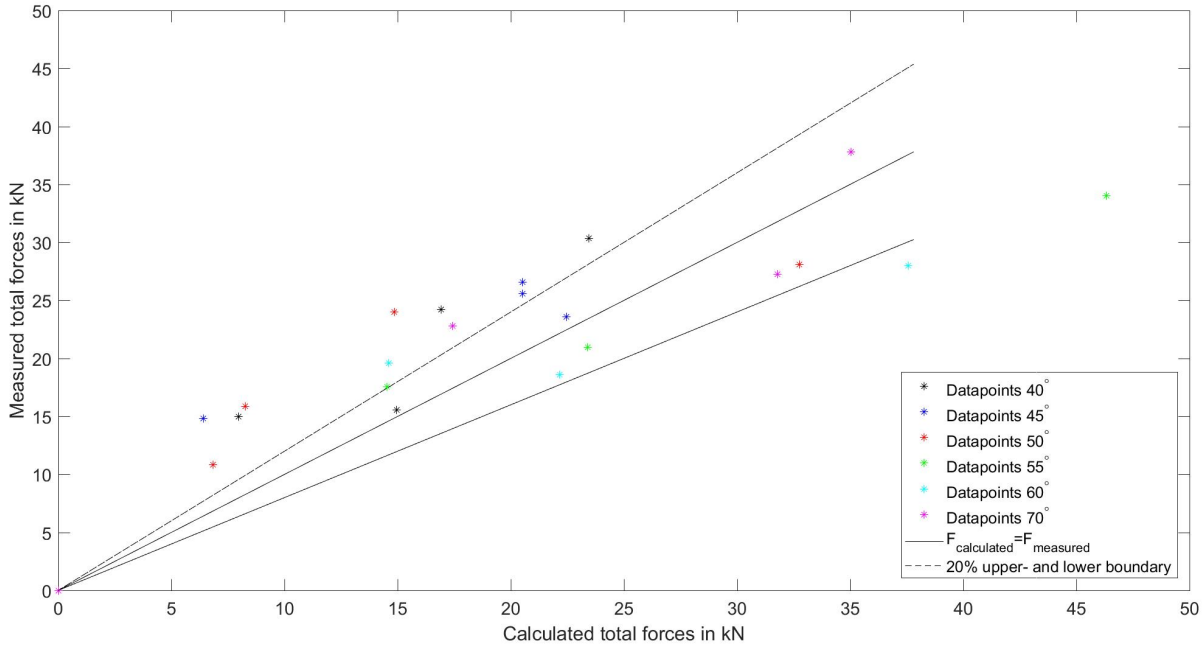

Figure 4.20: Predicted total forces compared with measured total forces

Comparing the total results of the Nishimatsu models including both expansions reveals that although it improved tremendously, it is still not perfect. The horizontal part seems to predict the forces better than the vertical part. Especially the larger cutting forces are predicted well. While the differences with the smaller cutting forces are larger. However the vertical force predictions are definitely not accurate enough. The deviations seem to increase with the cutting angle.

To further analyse the force predictions, the contributions of the expansions are calculated percentage wise and visualized in figures 4.21 and 4.22.

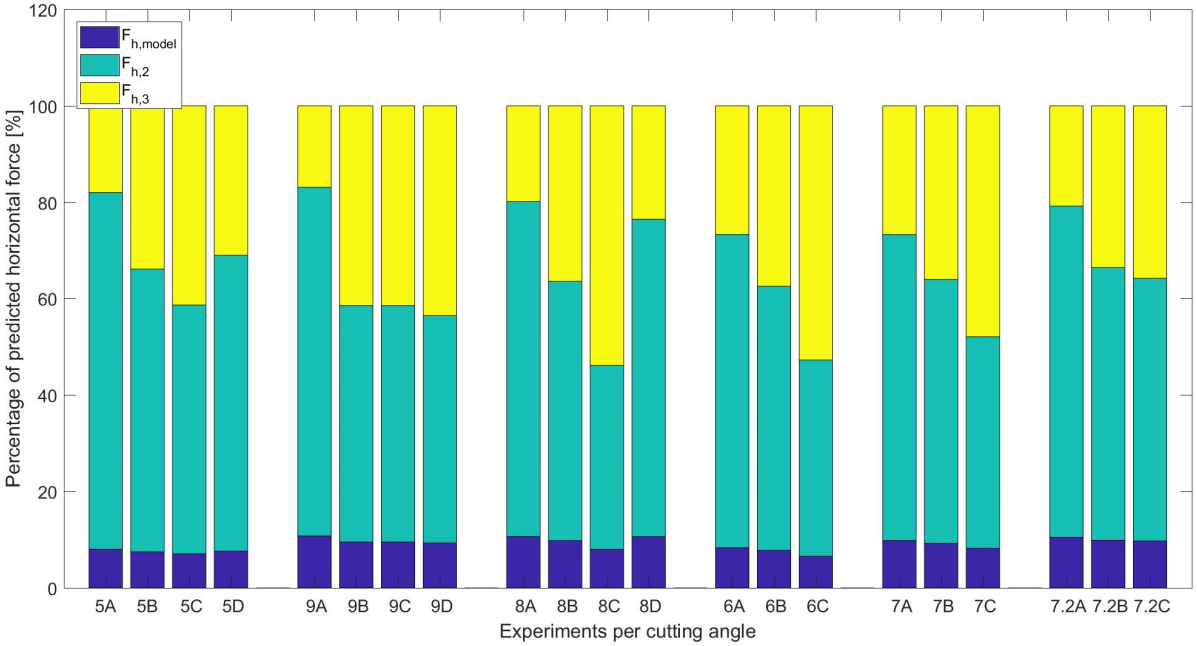

Figure 4.21: Contributions of the different force components to the predicted horizontal cutting force

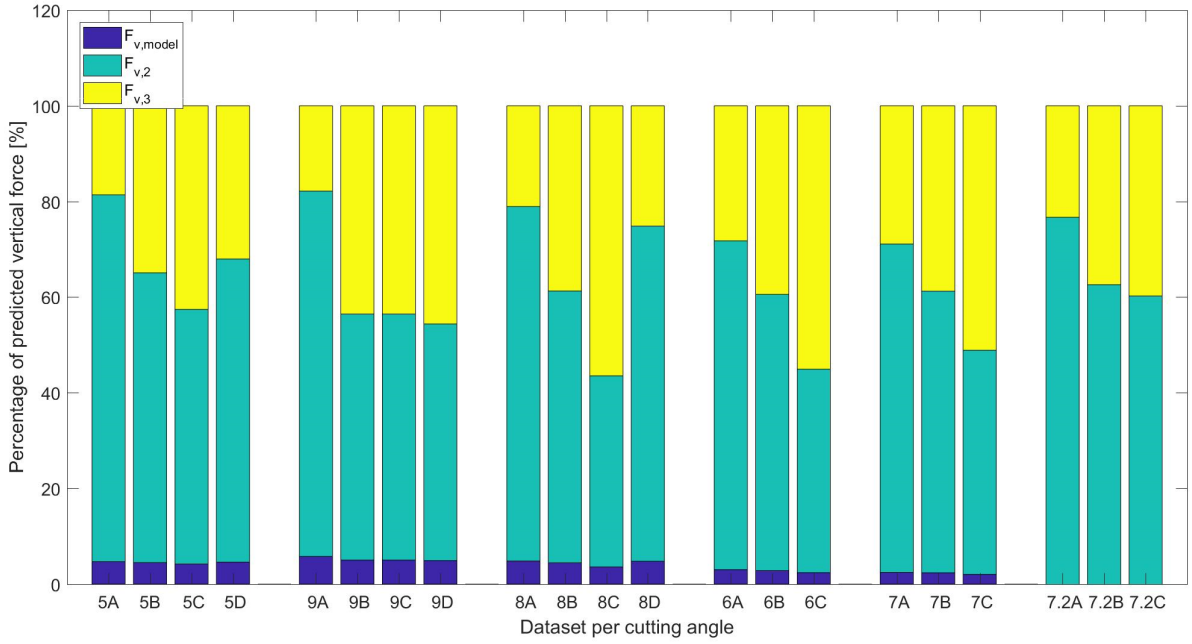

Figure 4.22: Contributions of the different force components to the predicted vertical cutting force

Examining the contributions of the shear expansion reveal that, of course, its contributions increases with an increasing cutting depth. But another interesting observation is the optimum contributions with datasets 8, 6 and 7 (cutting angles 50-60°). Apparently with these angles the sideways out breaking of rock is at its maximum. So cutting in this range of angles can lead to an exponential increase of the cutting force. The shear force increases quadratically dependent with the depth. Therefore the total cutting force increase could become quadratically increasing as well, especially with large cutting depths.

Where the contributions of the shear expansions are minimum, the indentation forces becomes more dominant. This happens with a 40-45° cutting angle (dataset 5 and 9), or with a cutting angle large than 60° (dataset 7.2). Especially with small cutting depths the indentation forces are dominant and one could expect an negatively increase in cutting force. As the depth gets larger, the shear forces become more dominant again and the indentation force contributions decrease.

Finally, the contributions of the 2D calculation model remain more or less constant with the horizontal cutting force. However, they seem to disappear in the vertical forces when the cutting angle increases. This is an remarkable phenomena, considering the fact that larger cutting angles cause larger vertical cutting forces.

5

CONCLUSIONS AND RECOMMENDATIONS

The cutting of rock is a process with a lot of uncertainties. Rock is assumed to be a homogeneous material, but in fact the internal structure within the same sample can differ significantly. Another contribution to the challenges to predict the rock cutting forces accurately is the fact that small deviations in the cutting geometry can lead to large differences in between the predicted and measured cutting forces. After conducting research into the failure of rock and the occurring cutting forces several conclusions and recommendations are made by the author.

5.1. CONCLUSIONS

After conducting the linear cutting experiments the failure is assumed to be brittle shear based on the presence of crushed material (which indicates a crushed zone) and the limited cutting depth (so not enough depth to develop a tensile crack). However, comparing the predicted cutting forces from the Nishimatsu model with the measured cutting forces show tremendous differences. It is therefore concluded that both the 2D assumption and the assumption of a sharp cutting tool are limiting factors in predicting the forces accurately. However other factors might also play a role (more in the recommendations) this research focussed on these 2 topics.

The measured cutting forces during the experiments confirm the linear relationship between cutting force and cutting depth. After separating the indentation forces and shearing forces from the cutting force, an interesting addition to this claim can be made: the indentation part of the cutting force increase with a root of the depth, while the shear part of the cutting force increase quadratically with the depth. As a consequence the forces in a cutting process dominated by the shearing would increase quadratically. While in a indentation dominated cutting process, which could occur while scraping, the force would increase with a root of the depth.

Analysing the contributions of the expansions to the predicted cutting forces show a maximum contribution of the shear component of the cutting force while cutting with a 50-60° cutting angle. Apparently this range in cutting angles results in more sideways out breaking, which implicates that cutting at a larger depth could result in a quadratically increasing cutting force. Cutting with a 40-45° or 70° cutting angle results in a failure mode where the indentation force becomes very dominant. Especially while cutting at a shallow depth. Since the indentation force increases with a root of the depth, the total cutting force could show this behaviour as well.

Analysing the results from the proposed formulas it is clear that even though it increases the accuracy of the cutting models drastically, it is still far from perfect. The fact that the calculation model including both expansions still underestimates the cutting forces indicates that there are other processes involved as well. The horizontal part of the proposed expanded formulas produces results that are definitely a step in the right direction and increases the accuracy tremendously. The vertical part however still shows significant differences. The reason for the poor predictions of the vertical force are not clear. The calculation models and the proposed expansions have difficulties predicting the vertical force components correctly.

5.2. RECOMMENDATIONS

A first recommendation is to conduct indentation experiments on rock samples to precisely determine the indentation resistance of rock. During this research the value 3 is used, but the absence of clear research in this direction makes it uncertain. When the exact value is known, it can be substituted into the formula for the indentation force and the coefficient can be empirically determined again.

Secondly the influence of the shear angle on the indentation and shear part of the cutting forces is an interesting research topic. The lack of data on this topic made it difficult to establish a relation and finding this relation increases the applicability of these expanded models. This would probably also increase the physical interpretation of the coefficients used for both the indentation force and the shear force components.

During this research both indentation forces and shearing forces occurred, but this is (probably) not always valid. This research shows a more shear dominant process with a 50-60° cutting angle, while especially the 70° angle is more indentation force dominant. However, there could be situations in which only one of these phenomena occur. More understanding on this topic would not only increase the accuracy of the force predictions, but also give more knowledge and insight in the physics of the rock cutting process. If the boundary conditions for both the shear - and indentation force component are established, one could conduct cutting experiments with larger cutting depths. The hypothesis of a shear dominant and therefore quadratically increasing cutting force could be demonstrated.

One of the aspects that might play a role, in particular with the horizontal component of the cutting force, is the friction between the cutting tool and the rock. When a crushed zone is formed around the tip of the pick point a wear flat develops. This wear flat is responsible for another resistance force, which is however not included in this research. More research on this topic, especially a friction force calculation model, would increase the predictions of the cutting forces even more.

The experiments were conducted on only 1 type of rock. Each sample had similar characteristics. An interesting research topic would be to conduct these experiments on different types of rock to check whether the formula produces results with a similar accuracy.

NOMENCLATURE

Abbreviations

BTS	Brazilian Tensile Strength	MPa
CCCC	China Communication Construction Company	
NERCD	National Engineer Research Center of Dredging Technology and Equipment	
UCS	Unconfined Compressive Strength	MPa
USBR	United States Bureau of Reclamation	

Greek symbols

α, α_c	Cutting angle	$^\circ$
β	Basic friction angle, Shear angle	$^\circ$, $^\circ$
β_1	Out breaking angle	$^\circ$
β_2	Out breaking angle	$^\circ$
δ	External friction angle	$^\circ$
λ	Strengthening factor	-
μ	Dynamic friction coefficient	-
ρ	Density	$\frac{kg}{m^3}$
τ	Shear stress	MPa
ϕ	Internal friction angle	$^\circ$
σ_h	Principal horizontal stress	MPa
α_i	Initial angle of plane in Mohr's circle	$^\circ$
α_p	Pick point angle	$^\circ$
σ_t	Tensile strength	MPa
σ_v	Principal vertical stress	MPa

Roman symbols

A	Area	m^2
B	Brittleness	-
c	Cohesion	MPa
c_a	Emperical shear force coefficient	-
c_f	Emperical indentation force coefficient	-
c_m	Mobilized cohesion	MPa
c_{xn}	Calibration coefficient negative x-axis	-
c_{xp}	Calibration coefficient positive x-axis	-
c_{yn}	Calibration coefficient negative y-axis	-
c_{yp}	Calibration coefficient positive y-axis	-
c_{zn}	Calibration coefficient negative z-axis	-
c_{zp}	Calibration coefficient positive z-axis	-
D	Diameter	m
E	Young's Modulus	GPa
F_h	Horizontal force component	kN
F_{h2}	Horizontal part of indentation force	kN
F_{h3}	Horizontal part of shear force	kN
$F_{h,m}$	Horizontal force by calculation model	kN
F_t	Total cutting force	kN
F_{t2}	Total indentation force	kN
F_{t3}	Total shear force	kN
F_U	Force during UCS test	m

F_v	Horizontal force component	kN
F_{v2}	Vertical part of indentation force	kN
F_{v3}	Vertical part of shear force	kN
$F_{v,m}$	Vertical force by calculation model	kN
F_x	Measured vertical cutting force	kN
$F_{x,max}$	Maximum measured vertical cutting force	kN
$F_{x,mean}$	Mean measured vertical cutting force	kN
F_y	Measured horizontal cutting force perpendicular to cutting direction	kN
$F_{y,max}$	Maximum measured horizontal cutting force perpendicular to cutting direction	kN
$F_{y,mean}$	Mean measured horizontal cutting force perpendicular to cutting direction	kN
F_z	Measured horizontal cutting force in cutting direction	kN
$F_{z,max}$	Measured horizontal cutting force in cutting direction	kN
$F_{z,mean}$	Measured horizontal cutting force in cutting direction	kN
g	Gravitation	$\frac{m}{s^2}$
h, h_i	Depth of cut	m
K_1, K_2	Force equilibrium coefficients	-
L_B	Length of sample for BTS tests	m
L_p	Pick point length	m
L_t	Pick point tip length	m
L_U	Length of sample for UCS tests	m
m	Mass	kg
n	Stress distribution factor	-
P	Polynomial	-
P_2	Horizontal part of indentation force	kN
Q_2	Vertical part of indentation force	kN
R_R	Rock resistance	kN
S_i	Sample number i	kN
uV	Microvolt output pressure sensor	μV
V	Volume	m^3
w, w_p	Width of cutting tool, Pick point width	m
w_c	Width of cut	m

REFERENCES

Blasio, F.V. de. 2011. *Introduction to the Physics of Landslides, Lecture notes on the dynamics of mass wasting.*

Defence Nuclear Agency, *MEASUREMENTS OF DYNAMIC FRICTION BETWEEN ROCK AND STEEL, Washington D.C., 25-10-1976.* 1976. title.

Evans, I. 1964. *The force required to cut coal with blunt wedges, International Journal of Rock Mechanics and Mining Sciences, Volume 2, 1965.*

Forster, S.W. 1991. *Rock and Mineral Identification for Engineers, U.S. Department of Transportation, November 1991.*

Helmons, R. 2017. *Excavation of hard deposits and rocks: On the cutting of saturated rock.*

Hucka, V. and Das, B. 1974. *Brittleness determination of rocks by different methods, International Journal of Rock Mechanics and Mining Sciences, Volume 11.*

Merchant, M.E. 1945. *Mechanics of the metal cutting process. I. Orthogonal cutting and a type 2 chip, Journal of Applied Physics, Volume 16, Number 5, May, 1945.*

Miedema. 2018. *Personal communication.*

Miedema, S.A. 2014. *The Delft Sand, Clay and Rock Cutting Model.*

Nishimatsu, Y. 1971. *The mechanics of rock cutting, International Journal of Rock Mechanics and Mining Sciences, Volume 9, 1972.*

USBR. 2009. *Procedure for Determining the Angle of Basic Friction Using a Tilting Table Test, United States Bureau of Reclamation, Materials Engineering and Research Laboratory, Technical Service Center, Denver, Colorado.*

Vlasblom, W.J. 2007. *Cutting of rock, Lecture WB3413/OE4626 Dredging Processes.*

Zhantao Li. 2012. *An analytical drilling model of drag bits for evaluation of rock strength, The Japanese Geotechnical Society, Soils and Foundations.*

BIBLIOGRAPHY

Altindag R., *The evaluation of brittleness concept on rotary blast hole drills*, 2002

Altindag R., *Correlation of specific energy with rock brittleness concepts on rock cutting*, 2003

Alvarez Grima M., Miedema S.A., van de Ketterij R.G., Yenigül N.B., van Rhee C., *Effect on high hyperbaric pressure on rock cutting process*, 2015

Bilgin N., Demircin M.A., Copur H., Balci C., Tuncdemir H., Akcin N., *Dominant rock properties affecting the performance of conical picks and the comparison of some experimental and theoretical results*, 2006

Chen, X., Miedema, S.A., van Rhee, C., *Numerical methods for modeling the rock cutting process in deep sea mining*, 2014

Cools, P.M.C.B.M., *Temperature Measurements Upon the Chisel Surface During Rock Cutting*, 1993

Deketh, H.J.R., *Wear of Rock Cutting Tools, Laboratory Experiments on the Abrasivity Of Rock*, 1995

Evans I., *The force required to cut coal with blunt wedges*, 1964

Forster S.W., *Rock and mineral identification for engineers*, jaartal

Franklin, John A., Hoek, Evert, *Developments in Triaxial Testing Technique*, 1970

Gaffney E.S., *Measurements of dynamic friction between rock and steel*, 1976

Goktan, R.M., Gunes, N., *A semi-empirical approach to cutting force prediction for point-attack picks*, 2005

Goktan, R.M., *Brittleness and micro-scale rock cutting efficiency*, 1991

Hartlieb, P., Grafe, B., Shepel, T., Malovyk, A., Akbari, B., *Experimental study on artificially induced crack patterns and their consequences on mechanical excavation processes*, 2017

Hartlieb, P., Grafe, B., *Experimental Study on Microwave Assisted Hard Rock Cutting of Granite*, 2017

Helmons R., Miedema S.A., van Rhee C., *Modeling the Effect of Water Depth on Rock Cutting Processes with the use of Discrete Element Method*, 2015

Helmons, R., *Excavation of hard deposits and rocks: On the cutting of saturated rock*, 2017

Huang, H., Detournay, E., *Discrete element modeling of tool-rock interaction II: rock indentation*, 2012

Huang H., Lecampion B., Detournay, E., *Discrete element modeling of tool-rock interaction I: rock cutting*, 2012

Hucka, V., Das, B., *Brittleness Determination of Rocks by Different Methods*, 1974

van Kesteren, W.G.M., *Numerical Simulations of Crack Bifurcation in the Chip Forming Cutting Process in Rock*, 1995

Leandro, R.A., González, J., *Comparison of different techniques of tilt testing and basic friction angle variablility assessment*, 2012

Malkowski, Piotr, *Behaviour of joints in sandstones during the shear test*, 2015

Merchant, M.E., *Mechanics of the Metal Cutting Process*, 1945

Miedema, S.A., *Dredging Processes: The Cutting of Sand, Clay & Rock Excavating Equipment*, 2012

Miedema, S.A., *The Delft Sand, Clay & Rock Cutting Model*, 2014

Nishimatsu, Y., *The mechanics of rock cutting*, 1972

Potyondy D.O., Cundall P.A., *A bonded-particle model for rock*, 2004

Prasad, U., *Drillability of a rock in terms of its physico-mechanical and micro-structural properties*, 2009

Richard, T., Dagrain F., Poyol E., Detournay, E., *Rock strength determination from scratch tests*, 2012

Rojek J., Labra C., Okan Su O., Oñate E., *Comparative study of different discrete element models and evaluation of equivalent micromechanical parameters*, 2012

Tiryaki B.,Cagatay Dikmen A., *Effects of Rock Properties on Specific Cutting Energy in Linear Cutting of Sandstones by Picks*, 2006

Ulusay, R., *The ISRM suggested methods for rock characterization, testing and monitoring*, 2007-2014

Vlasblom, W.J., *Cutting of Rock*, 2007

Zhantao Li, Ken-ichi Itakura, *An analytical drilling model of drag bits for evaluation of rock strength*, 2012

LIST OF FIGURES

LIST OF TABLES

PICTURES OF CUTTING TOOL


0.5mm
1 2 3 4 5 6
mm

3D SCHEMATIZATION OF CUTTING TOOL

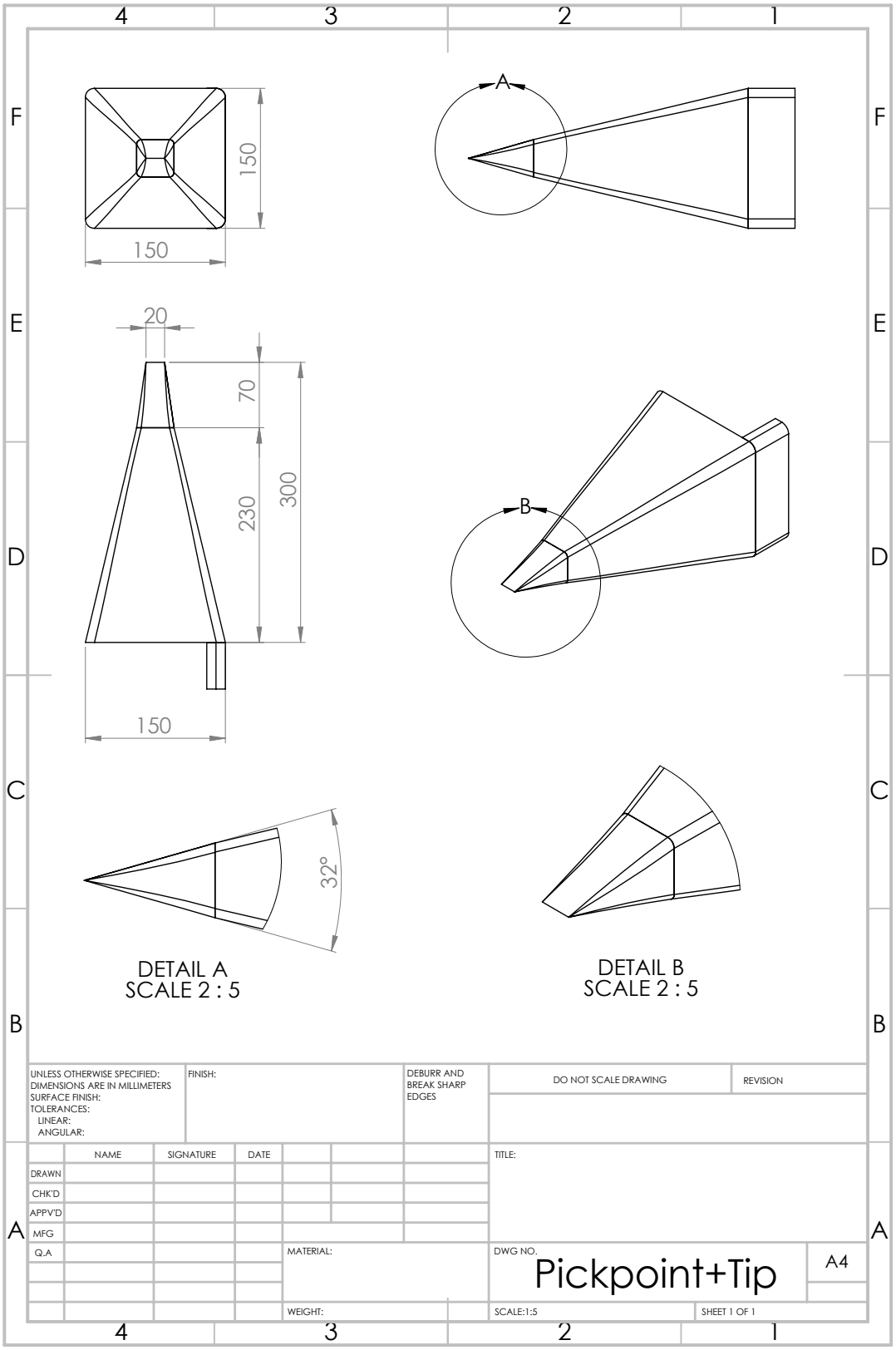
4
3
2
1
F
E
D
C
B
A
150
150
A
20
70
230
300
150
B
32°
DETAIL A
SCALE 2 : 5
DETAIL B
SCALE 2 : 5
UNLESS OTHERWISE SPECIFIED:
DIMENSIONS ARE IN MILLIMETERS
SURFACE FINISH:
TOLERANCES:
LINEAR:
ANGULAR:
FINISH:
DEBURR AND BREAK SHARP EDGES
DO NOT SCALE DRAWING
REVISION
NAME
SIGNATURE
DATE
DRAWN
CHK'D
APPV'D
MFG
Q.A
TITLE:
MATERIAL:
DWG NO.
Pickpoint+Tip
A4
WEIGHT:
SCALE:1:5
SHEET 1 OF 1

TEST REPORT ROCK SAMPLES


云南YZJ质检
检验报告
TEST REPORT
YUNNAN
INSTITUTE OF PRODUCT
QUALITY
SUPERVISION & INSPECTION
云南省产品质量监督检验研究院
国家热带农副产品质量监督检验中心
国家有色金属产品质量监督检验中心(云南)
国家磷化工产品质量监督检验中心(云南)

162520110030

(2016)滇质监验字001号

云南YQSi质检

云南省产品质量监督检验研究院

检 验 报 告

№: QG201701970

共2页第1页

产品名称	天然砂岩（黄）	商标	/	规格型号	50×50×50(mm) 300×100×25(mm)
生产日期/批号	2017-10-31 /				
受检单位名称及联系电话	云南隆辉石材有限公司 （13629677278）				
生产单位名称及联系电话	云南隆辉石材有限公司 （13629677278）				
任务来源	昆明市质量技术监督局 昆质监局通〔2017〕160号			检验类型	州市监督抽查
抽样日期	2017年11月1日	抽样人员	李振岩 邱峰	样品到达日期	2017年11月8日
样品数量	50×50×50(mm) 42块、300×100×25(mm) 30块	抽样等数	2000m²	检查封样人员	云梦
样品等级	合格品	样品/抽样单编号	（昆）质技监抽字[2017]第石禄01-2号	封样状态	外封条完好。
检验依据	KMCCGF 07-2017《天然石材产品质量监督抽查实施规范》、GB/T 23452-2009《天然砂岩建筑板材》、GB 6566-2010《建筑材料放射性核素限量》				
检验地点	昆明经济技术开发区出口加工区玉缘路金海国际b2栋				
检验结论	经按KMCCGF 07-2017《天然石材产品质量监督抽查实施规范》、GB/T 23452-2009《天然砂岩建筑板材》、GB 6566-2010《建筑材料放射性核素限量》检验，判定该批产品实物质量合格。 签发日期：2017年11月29日				
备注	杂砂岩。				

批准： 刘川 Approved by:　　审核： 谢波 Checked by:　　主检： 马宏伟 Tested by:

云南省产品质量监督检验研究院

检验报告附页

No: QG201701970 共2页第2页

序号	检测项目		单位	标准要求	检测结果	单项判定
1	体积密度		g/cm^3	≥2.00	2.34	合 格
2	吸水率		%	≤8	2.8	合 格
3	压缩强度	干燥	MPa	≥12.6	36	合 格
		水饱和	MPa	≥12.6	49	合 格
4	弯曲强度	干燥	MPa	≥2.4	5.4	合 格
		水饱和	MPa	≥2.4	3.9	合 格
5	耐磨性		1/cm^3	≥2	10	合 格
6	放射性核素限量		——	A类装饰装修材料 内照射指数I_{Ra}≤1.0 外照射指数I_r≤1.3 产销与使用范围不受限制	I_{Ra}: 0.31 I_r: 1.07	合 格
以 下 空 白						

UCS ROCK SAMPLES

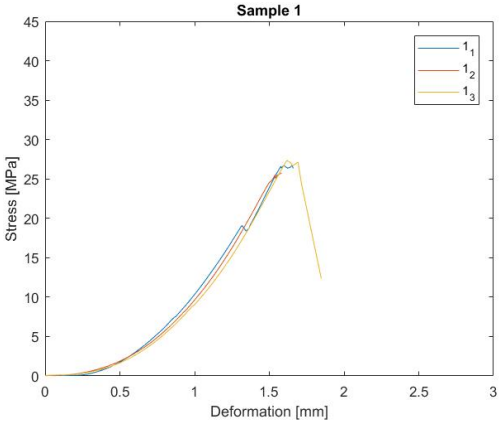

(a) $UCS_{1_1} = 26.721$ MPa, $UCS_{1_2} = 25.775$ MPa
$UCS_{1_3} = 27.349$ MPa

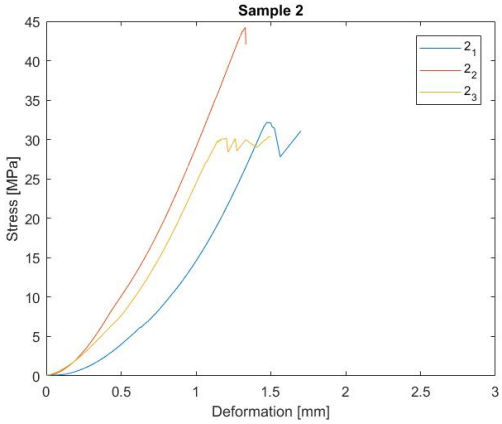

(b) $UCS_{2_1} = 32.168$ MPa, $UCS_{2_2} = 44.208$ MPa
$UCS_{2_3} = 30.448$ MPa

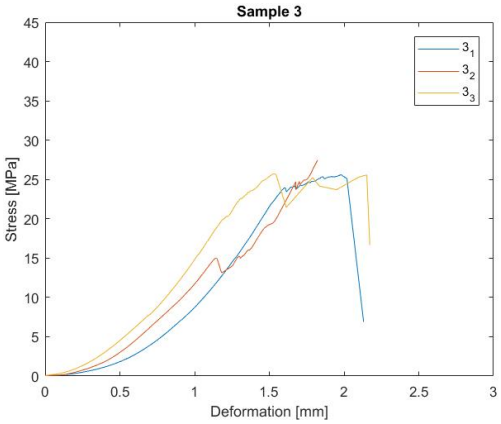

(c) $UCS_{3_1} = 25.608$ MPa, $UCS_{3_2} = 27.578$ MPa
$UCS_{3_3} = 25.726$ MPa

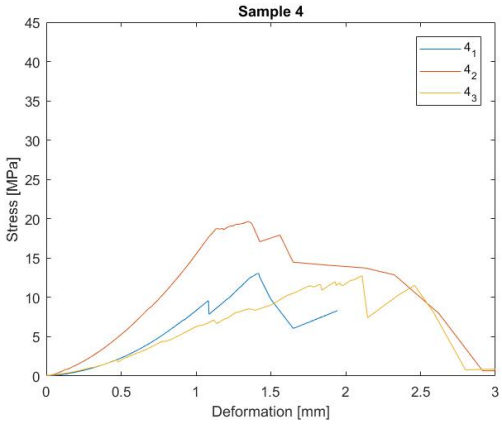

(d) $UCS_{4_1} = 13.047$ MPa, $UCS_{4_2} = 19.639$ MPa
$UCS_{4_3} = 12.755$ MPa

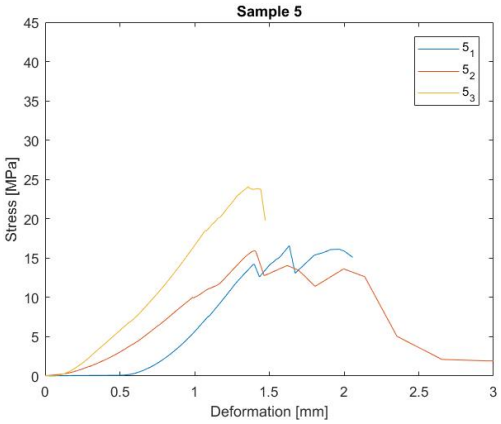

(e) $UCS_{5_1} = 16.560$ MPa, $UCS_{5_2} = 15.932$ MPa
$UCS_{5_3} = 24.072$ MPa

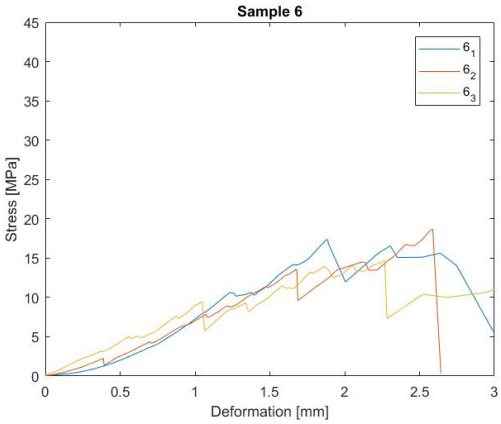

(f) $UCS_{6_1} = 17.384$ MPa, $UCS_{6_2} = 18.680$ MPa
$UCS_{6_3} = 14.706$ MPa

Figure 3: UCS of rock samples 1-6

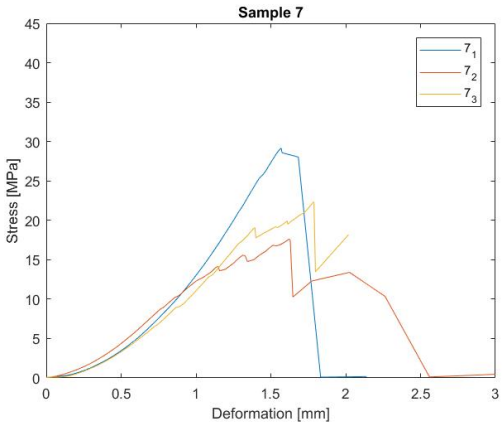

(a) UCS_{7_1} = 29.146 MPa, UCS_{7_2} = 17.615 MPa
UCS_{7_3} =22.320 MPa

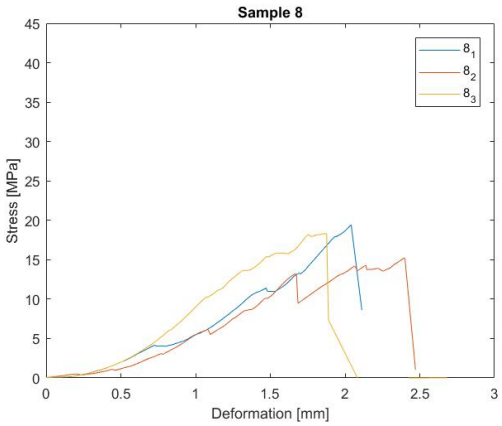

(b) UCS_{8_1} = 19.396 MPa, UCS_{8_2} = 14.223 MPa
UCS_{8_3} = 18.318 MPa

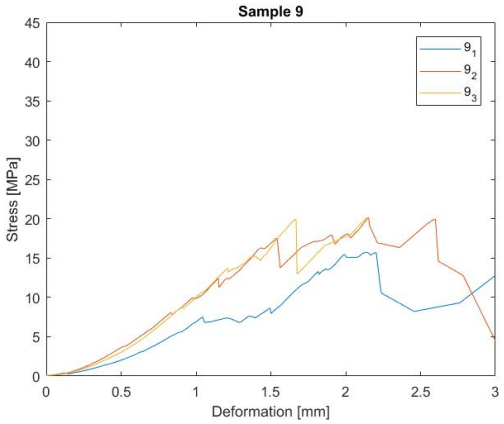

(c) UCS_{9_1} = 15.748 MPa, UCS_{9_2} = 20.104 MPa
UCS_{9_3} = 20.207 MPa

Figure 4: UCS of rock samples 7-9

BTS ROCK SAMPLES

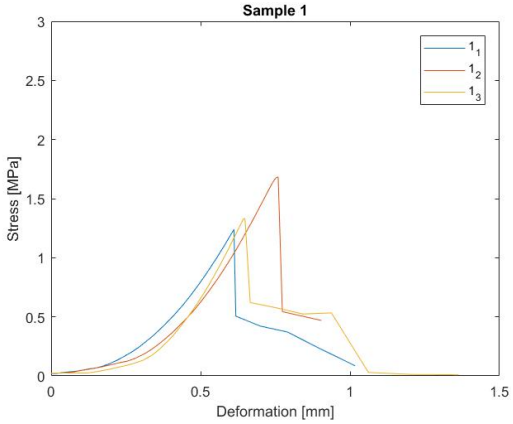

(a) $BTS_{1_1} = 1.239$ MPa, $BTS_{1_2} = 1.684$ MPa
$BTS_{1_3} = 1.331$ MPa

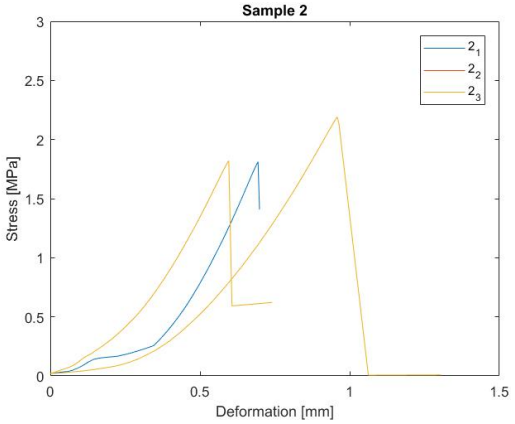

(b) $BTS_{2_1} = 1.811$ MPa, $BTS_{2_2} = 2.191$ MPa
$BTS_{2_3} = 1.821$ MPa

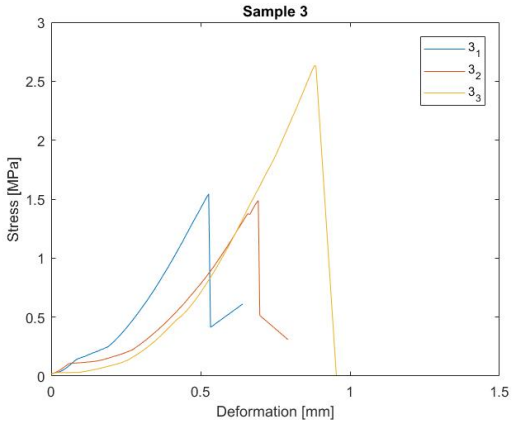

(c) $BTS_{3_1} = 1.543$ MPa, $BTS_{3_2} = 1.488$ MPa
$BTS_{3_3} = 2.633$ MPa

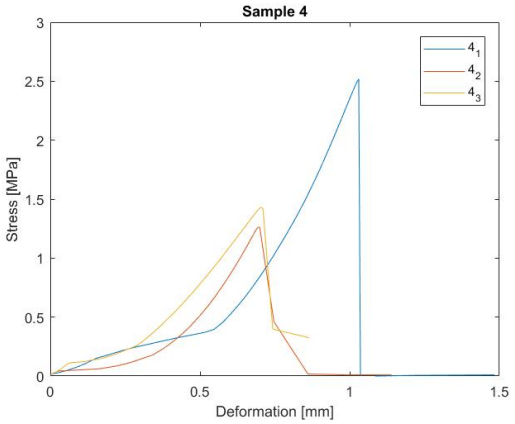

(d) $BTS_{4_1} = 2.518$ MPa, $BTS_{4_2} = 1.261$ MPa
$BTS_{4_3} = 1.430$ MPa

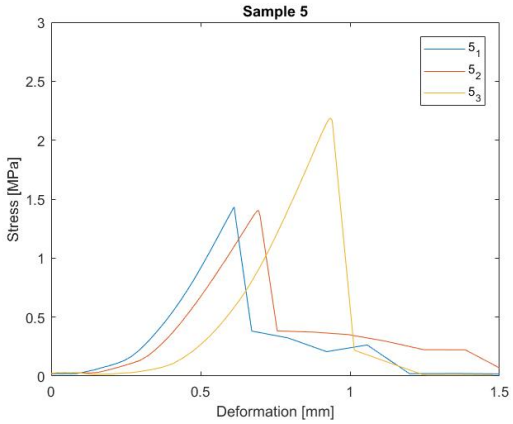

(e) $BTS_{5_1} = 1.434$ MPa, $BTS_{5_2} = 1.406$ MPa
$BTS_{5_3} = 2.188$ MPa

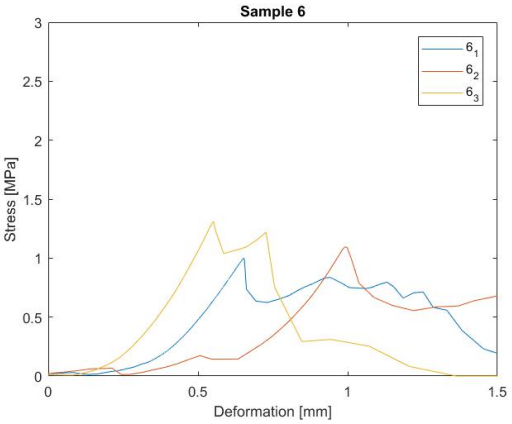

(f) $BTS_{6_1} = 1.000$ MPa, $BTS_{6_2} = 1.095$ MPa
$BTS_{6_3} = 1.311$ MPa

Figure 5: BTS of rock samples 1-6

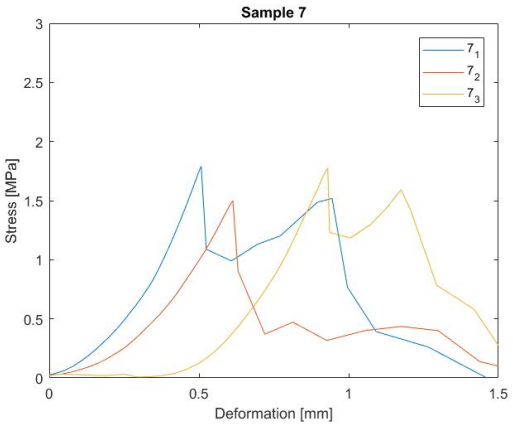

(a) $BTS_{7_1} = 1.789$ MPa, $BTS_{7_2} = 1.499$ MPa
$BTS_{7_3} = 1.776$ MPa

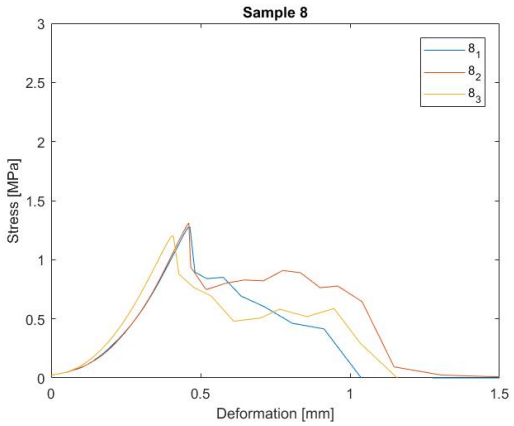

(b) $BTS_{8_1} = 1.278$ MPa, $BTS_{8_2} = 1.311$ MPa
$BTS_{8_3} = 1.201$ MPa

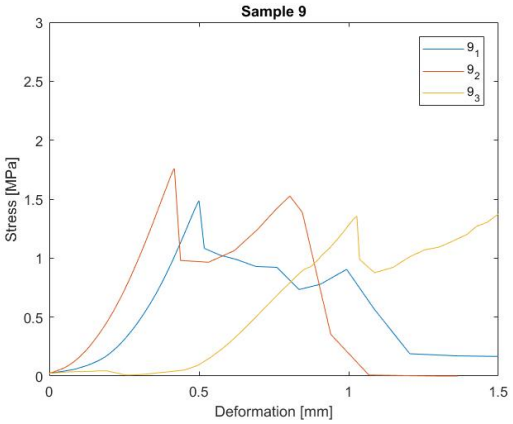

(c) $BTS_{9_1} = 1.487$ MPa, $BTS_{9_2} = 1.760$ MPa
$BTS_{9_3} = 1.449$ MPa

Figure 6: BTS of rock samples 7-9

3D SCHEMATIZATION OF ROCK SAMPLES

Overview experiments

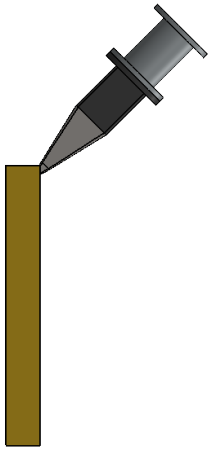

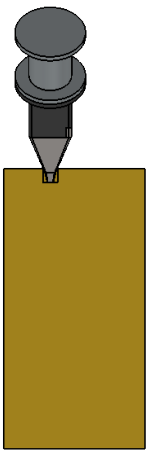

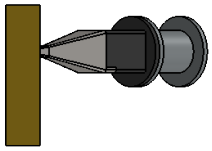

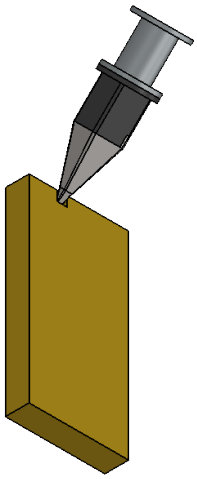

UNLESS OTHERWISE SPECIFIED: DIMENSIONS ARE IN MILLIMETERS SURFACE FINISH: TOLERANCES: LINEAR: ANGULAR:		FINISH:		DEBURR AND BREAK SHARP EDGES		DO NOT SCALE DRAWING	REVISION
	NAME	SIGNATURE	DATE				TITLE:
DRAWN							
CHK'D							
APPV'D							
MFG							
Q.A				MATERIAL:		DWG NO. Sample_pick	A4
				WEIGHT:		SCALE:1:20	SHEET 1 OF 1

PICTURES OF BROKEN PRESSURE SENSOR

PLANNING EXPERIMENTS

#	Notes:	Sample nr	Exp. Name	Date	Length of cut	Width pick	Angle	Velocity	Weight cut out	Depth0
1	Fail	5	502	15-8-2018	0.6	0.02	50	0.05		0.015
2	Fail	5	502	15-8-2018	0.6	0.02	50	0.05		0.01
3		5	503	15-8-2018	0.5	0.02	50	0.05	0.29916	0.01
4	Pit	5	504_pit	16-8-2018	0.45	0.02	50	0.05	0.31297	0.01
5	No pit	5	504	17-8-2018	0.5	0.02	50	0.05	0.38302	0.01
	Fail	5	5A	17-8-2018	0.9	0.02	40	0.05		0.005
1		5	5A	28-8-2018	0.7	0.02	40	0.05	0.22932	0.005
2		5	5B	28-8-2018	0.5	0.02	40	0.05	0.50743	0.015
3		5	5C	28-8-2018	0.7	0.02	40	0.05	1.22137	0.022
4		5	5D	19-9-2018	0.9	0.02	40	0.05	0.14528	0.013
5		9	9A	31-8-2018	0.9	0.02	45	0.05	0.12248	0.005
6		9	9B	31-8-2018	0.7	0.02	45	0.05	0.70301	0.015
7		9	9C	31-8-2018	0.8	0.02	45	0.05	1.16191	0.025
8		9	9D	19-9-2018	0.9	0.02	45	0.05	0.85062	0.015
9		8	8A	10-9-2018	1	0.02	50	0.05	0.04337	0.001
10		8	8B	10-9-2018	0.9	0.02	50	0.05	0.50823	0.015
11		8	8C	10-9-2018	0.9	0.02	50	0.05	1.5153	0.02
12		8	8D	19-9-2018	0.9	0.02	50	0.05	0.37372	0.014
13		6	6A	11-9-2018	1	0.02	55	0.05	0.61802	0.008
14		6	6B	11-9-2018	1	0.02	55	0.05	0.86821	0.01
15		6	6C	11-9-2018	1	0.02	55	0.05	1.55271	0.02
16		6	6extra							
17		7	7A	11-9-2018	1	0.02	60	0.05	0.23701	0.005
18		7	7B	11-9-2018	1	0.02	60	0.05	0.39144	0.01
19		7	7C	11-9-2018	0.9	0.02	60	0.05	1.29833	0.018
20		7	7extra							
21		7.2	7.2A	19-9-2018	0.9	0.02	70	0.05	0.2115	0.007
22		7.2	7.2B	19-9-2018	1	0.02	70	0.05	0.43798	0.021
23		7.2	7.2C	19-9-2018	0.9	0.02	70	0.05	0.9697	0.015
24		7.2	7.2extra							

Width0	Depth1	Width1	Depth2	Width2	Depth3	Width3	Depth4	Width4	Depth5	Width5
0.08	0.008	0.07	0.006	0.06	0.007	0.07	0.006	0.04	0.007	0.05
0.07	0.008	0.07	0.01	0.06	0.008	0.04	0.01	0.06		
0.1	0.01	0.09	0.008	0.08	0.008	0.06	0.009	0.08		
0.15	0.005	0.02	0.005	0.02	0.005	0.02	0.004	0.02	0.004	0.02
0.07	0.013	0.1	0.012	0.09	0.01	0.07	0.01	0.1	0.01	0.06
0.26	0.015	0.09	0.012	0.07	0.013	0.08	0.012	0.1	0.012	0.13
0.05	0.003	0.02	0.003	0.02	0.004	0.02	0.006	0.02	0.006	0.02
0.03	0.001	0.01	0.001	0.01	0.001	0.01	0.002	0.015	0.003	0.02
0.08	0.007	0.04	0.009	0.05	0.008	0.07	0.008	0.05	0.01	0.1
0.11	0.015	0.14	0.012	0.1	0.011	0.11	0.012	0.06	0.013	0.08
0.08	0.005	0.06	0.008	0.05	0.008	0.05	0.006	0.06	0.006	0.06
0.01	0.001	0.01	0.001	0.01	0.001	0.01	0.001	0.01	0.001	0.015
0.1	0.006	0.05	0.005	0.04	0.01	0.09	0.008	0.05	0.008	0.05
0.08	0.01	0.12	0.012	0.1	0.012	0.09	0.013	0.1	0.014	0.12
0.07	0.005	0.06	0.004	0.04	0.004	0.03	0.005	0.04	0.004	0.04
0.08	0.004	0.03	0.006	0.06	0.005	0.08	0.006	0.07	0.006	0.06
0.04	0.008	0.05	0.007	0.08	0.013	0.15	0.01	0.06	0.008	0.08
0.12	0.015	0.08	0.016	0.11	0.016	0.12	0.015	0.1	0.013	0.08
0.04	0.003	0.02	0.006	0.05	0.003	0.03	0.005	0.03	0.004	0.04
0.04	0.006	0.08	0.005	0.07	0.004	0.04	0.006	0.07	0.006	0.05
0.07	0.012	0.04	0.014	0.08	0.012	0.06	0.015	0.13	0.01	0.13
0.03	0.004	0.02	0.004	0.04	0.003	0.03	0.005	0.03	0.003	0.05
0.1	0.011	0.13	0.011	0.11	0.01	0.11	0.011	0.12	0.009	0.08
0.08	0.01	0.11	0.012	0.07	0.008	0.14	0.012	0.11	0.01	0.1

Depth6	Width6	Depth7	Width7	Depth8	Width8	Depth9	Width9	Depth10	Width10	Av depth	
-	-	-	-	-	-	-	-	-	-		
0.006	0.025	0.005	0.025							0.004875	
										0.011667	
0.012	0.09	0.013	0.09							0.013875	
0.008	0.02	0.008	0.04	0.009	0.06	0.006	0.05			0.0066	
0.003	0.02	0.003	0.02	0.005	0.05	0.005	0.03			0.0029	
0.012	0.06	0.013	0.07							0.01025	
0.012	0.09	0.012	0.07	0.01	0.06					0.013556	
0.006	0.08	0.01	0.05	0.015	0.1	0.014	0.08			0.0093	
0.001	0.015	0.001	0.015	0.002	0.02	0.003	0.02	0.004	0.02	0.001545	
0.008	0.03	0.01	0.06	0.008	0.05	0.008	0.05			0.0086	
0.017	0.2	0.014	0.1	0.015	0.13	0.015	0.15			0.0142	
0.005	0.05	0.005	0.05	0.005	0.05	0.005	0.05			0.0056	
0.005	0.04	0.006	0.05	0.008	0.07	0.008	0.08	0.006	0.07	0.006182	
0.009	0.07	0.009	0.06	0.012	0.11	0.009	0.06	0.012	0.08	0.009727	
0.012	0.09	0.012	0.1	0.016	0.09	0.015	0.17	0.015	0.09	0.015	
											2cm
0.005	0.03	0.006	0.06	0.006	0.05	0.007	0.05	0.005	0.06	0.005	
0.008	0.05	0.009	0.06	0.006	0.05	0.01	0.07	0.008	0.06	0.007091	
0.015	0.17	0.012	0.08	0.012	0.09	0.016	0.19			0.0136	
											1cm
0.005	0.04	0.006	0.05	0.007	0.03	0.006	0.03			0.005	
0.009	0.09	0.01	0.18	0.008	0.07	0.009	0.06	0.008	0.06	0.010636	
0.011	0.17	0.013	0.09	0.013	0.11	0.014	0.14			0.0118	
											1.5cm

CALIBRATION TABLE PRESSURE SENSOR

X 向加载（正向+）

加载力（Kg）	X（uV）	Y（uV）	Z（uV）
0	1	1	1
200	227	-5	-9
400	456	-13	-19
600	686	-21	-29
800	913	-26	-39
1000	1150	-32	-49
1200	1380	-39	-60
1400	1621	-48	-70
1600	1846	-52	-80
1800	2092	-62	-91
2000	2326	-71	-102
2200	2572	-80	-111
2400	2792	-91	-120
2600	3039	-98	-131
2800	3273	-109	-139
3000	3490	-120	-148
3200	3733	-128	-160

Positive x-direction

X 向加载（负向-）

加载力（Kg）	X（uV）	Y（uV）	Z（uV）
0	1	1	1
200	-222	11	12
400	-446	20	23
600	-669	26	34
800	-896	37	45
1000	-1122	46	56
1200	-1350	52	67
1400	-1575	62	78
1600	-1800	67	88
1800	-2020	75	99
2000	-2242	79	109
2200	-2466	85	120
2400	-2690	93	128
2600	-2915	100	139
2800	-3139	106	150
3000	-3364	110	157
3200	-3622	114	165

Negative x-direction

Y 向加载（正向+）

加载力（Kg）	X（uV）	Y（uV）	Z（uV）
0	-1	0	1
200	12	202	4
400	19	404	7
600	23	608	10
800	28	815	13
1000	35	1024	16
1200	43	1236	19
1400	52	1445	22
1600	57	1659	25
1800	64	1865	28
2000	70	2070	31
2200	76	2266	34
2400	83	2485	36
2600	89	2701	40
2800	94	2899	43
3000	100	3105	45
3200	105	3312	49

Positive y-direction

Y 向加载（负向-）

加载力（Kg）	X（uV）	Y（uV）	Z（uV）
0	1	1	1
200	-24	-202	-3
400	-45	-417	-7
600	-65	-630	-11
800	-87	-847	-15
1000	-106	-1054	-19
1200	-130	-1269	-23
1400	-149	-1486	-26
1600	-170	-1698	-30
1800	-184	-1908	-35
2000	-205	-2125	-38
2200	-220	-2345	-43
2400	-240	-2557	-46
2600	-255	-2771	-50
2800	-271	-2984	-54
3000	-290	-3200	-60
3200	-308	-3411	-65

Negative y-direction

Z 向加载

加载力（Kg）	X（uV）	Y（uV）	Z（uV）
0	0	0	0
200	10	5	18
400	20	8	36
600	29	10	54
800	39	11	72
1000	49	12	90
1200	59	12	107
1400	69	12	125
1600	79	11	142
1800	90	11	160
2000	101	10	179
2200	111	9	196
2400	121	9	213
2600	131	7	231
2800	140	12	248
3000	149	11	264
3200	158	10	285

Positive z-direction

RESULTS OF CUTTING EXPERIMENTS 9A-9D

EXPERIMENTS 9A-9D

For the remaining experiments, the same algorithm as described in chapter 3 is used: for every sample the rock characteristics are listed again first. Afterwards, the force output, together with other relevant data, is given per experiment. Next, the maximum forces are plotted to get an overview of the maximum forces over the depth. Then the cutting profiles are shown together with the particle size distributions.

Table 1: Sample 9: rock characteristics

	F_U	F_B	UCS	BTS	B	E	C	ϕ	δ	ρ
	kN	kN	MPa	MPa	[-]	GPa	MPa	°	°	kg/m^3
Sample 9	44.395	7.437	18.686	1.565	11.986	1.211	5.614	28	19	2312.681

.1. EXPERIMENT 9A

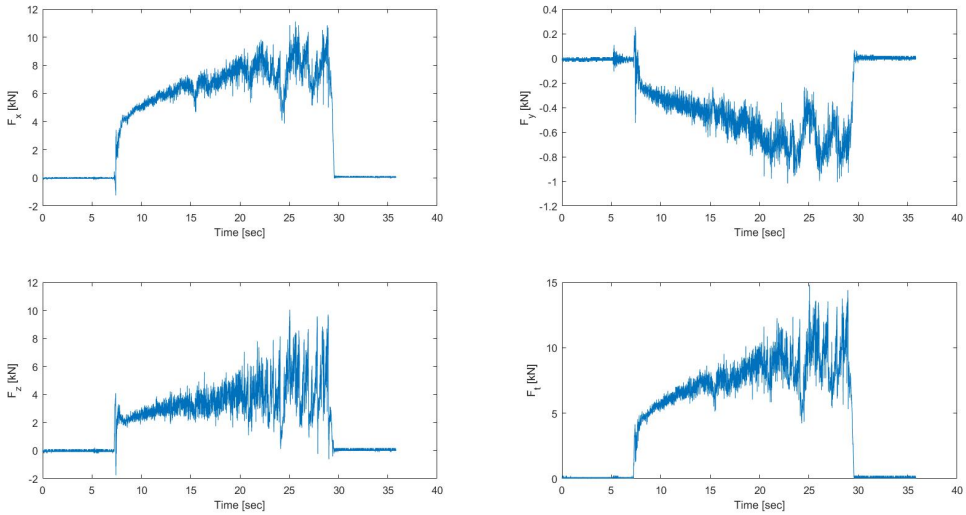

Figure 8: Experiment 9A: force in time

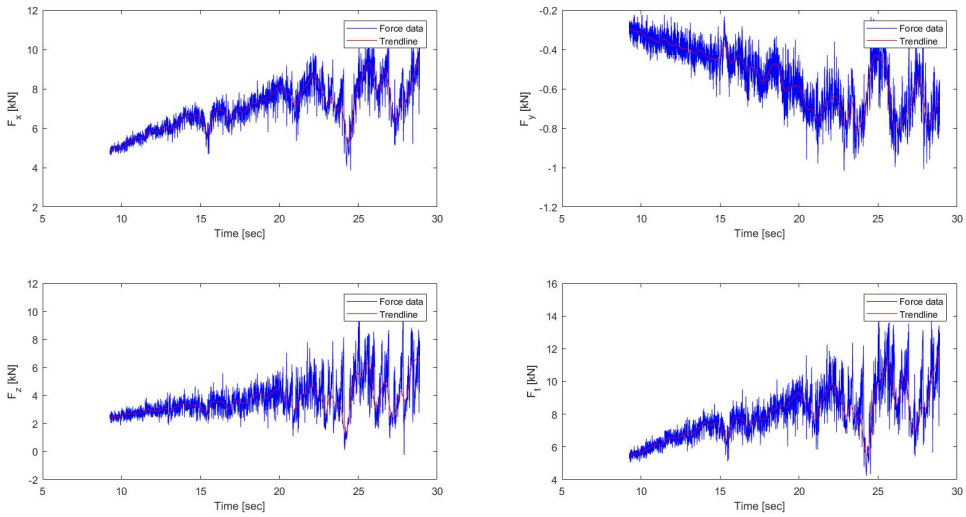

Figure 9: Experiment 9A: force in time

Table 2: Laboratory data of experiment 9A

	Cutting time [sec]	Average depth [cm]	Average width [cm]	Length [m]	Weight [kg]
Experiment 9A	18	0.29	2.15	0.9	0.122

Table 3: Cutting forces of experiment 9A

	$F_{x,max}$ [kN]	$F_{x,mean}$ [kN]	$F_{y,max}$ [kN]	$F_{y,mean}$ [kN]	$F_{z,max}$ [kN]	$F_{z,mean}$ [kN]	$F_{t,max}$ [kN]	$F_{t,mean}$ [kN]
Experiment 9A	11.12	7.01	-0.22	-0.54	10.05	3.78	14.81	8.02

.2. EXPERIMENT 9B

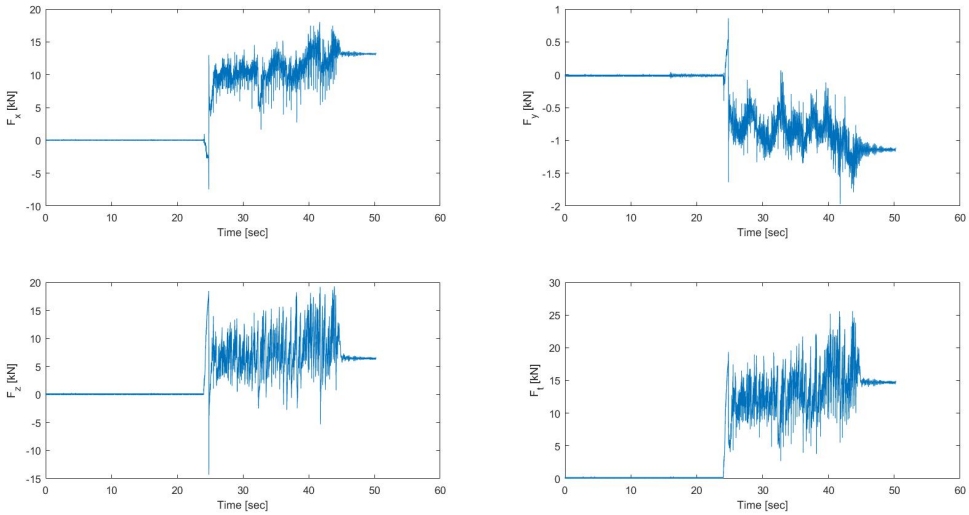

Figure 10: Experiment 9B: force in time

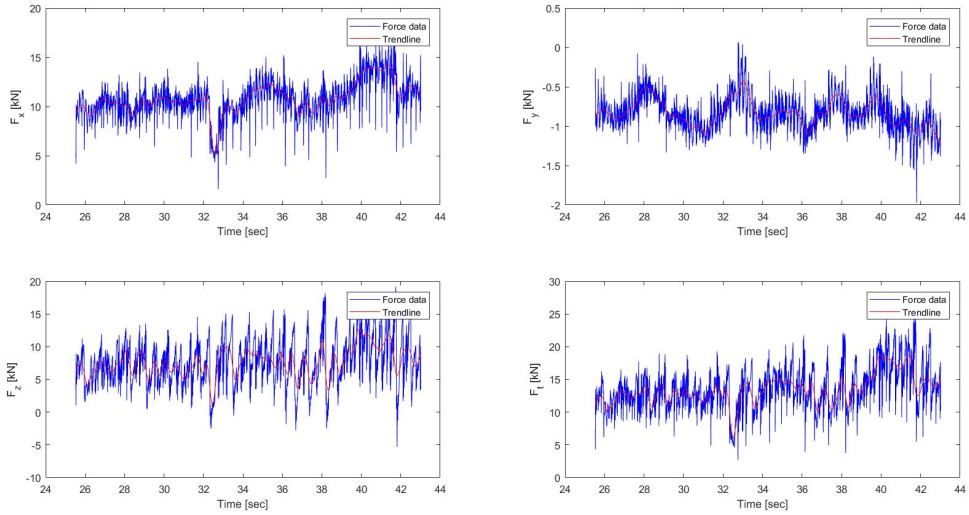

Figure 11: Experiment 9B: force in time

Table 4: Laboratory data of experiment 9B

	Cutting time [sec]	Average depth [cm]	Average width [cm]	Length [m]	Weight [kg]
Experiment 9B	14	1.03	6.50	0.7	0.703

Table 5: Cutting forces of experiment 9B

	$F_{x,max}$ [kN]	$F_{x,mean}$ [kN]	$F_{y,max}$ [kN]	$F_{y,mean}$ [kN]	$F_{z,max}$ [kN]	$F_{z,mean}$ [kN]	$F_{t,max}$ [kN]	$F_{t,mean}$ [kN]
Experiment 9B	18.04	10.70	0.07	-0.83	19.18	7.77	25.58	13.49

.3. EXPERIMENT 9C

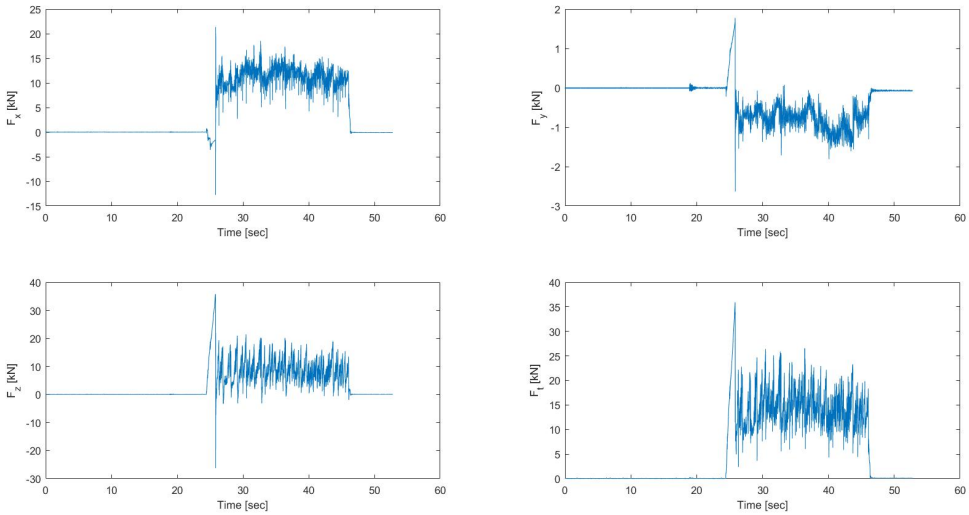

Figure 12: Experiment 9C: force in time

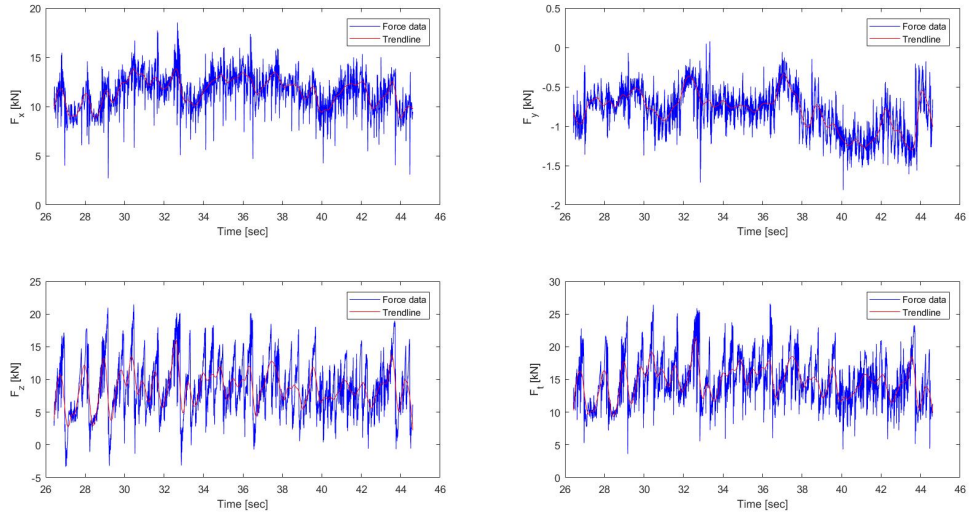

Figure 13: Experiment 9C: force in time

Table 6: Laboratory data of experiment 9C

	Cutting time [sec]	Average depth [cm]	Average width [cm]	Length [m]	Weight [kg]
Experiment 9C	16	1.36	9.11	0.8	1.162

Table 7: Cutting forces of experiment 9C

	$F_{x,max}$ [kN]	$F_{x,mean}$ [kN]	$F_{y,max}$ [kN]	$F_{y,mean}$ [kN]	$F_{z,max}$ [kN]	$F_{z,mean}$ [kN]	$F_{t,max}$ [kN]	$F_{t,mean}$ [kN]
Experiment 9C	18.53	11.45	0.08	-0.81	21.46	8.83	26.59	14.77

.4. EXPERIMENT 9D

Table 8: Average cutting dephs of experiments 9A-9C

	Experiment 9A [cm]	Experiment 9B [cm]	Experiment 9C [cm]
Average cutting depth	0.29	1.03	1.36

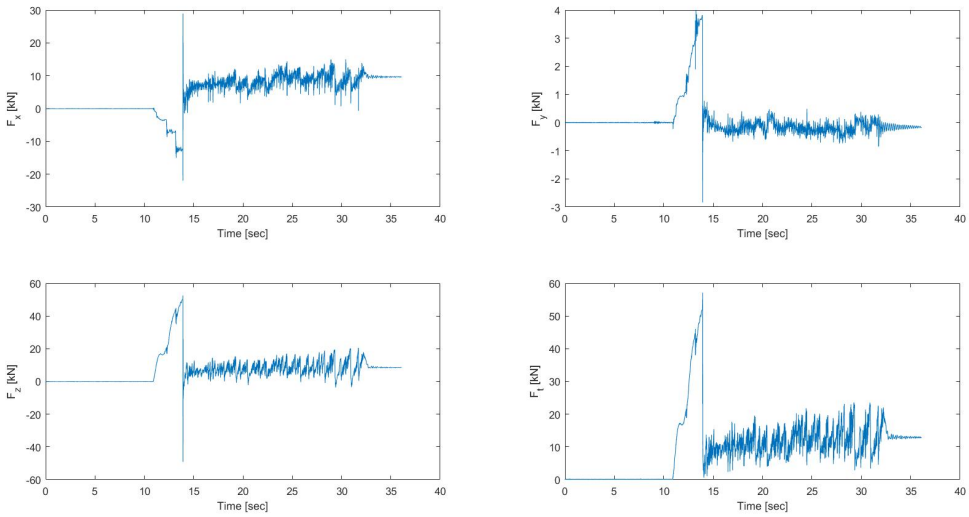

Figure 14: Experiment 9D: force in time

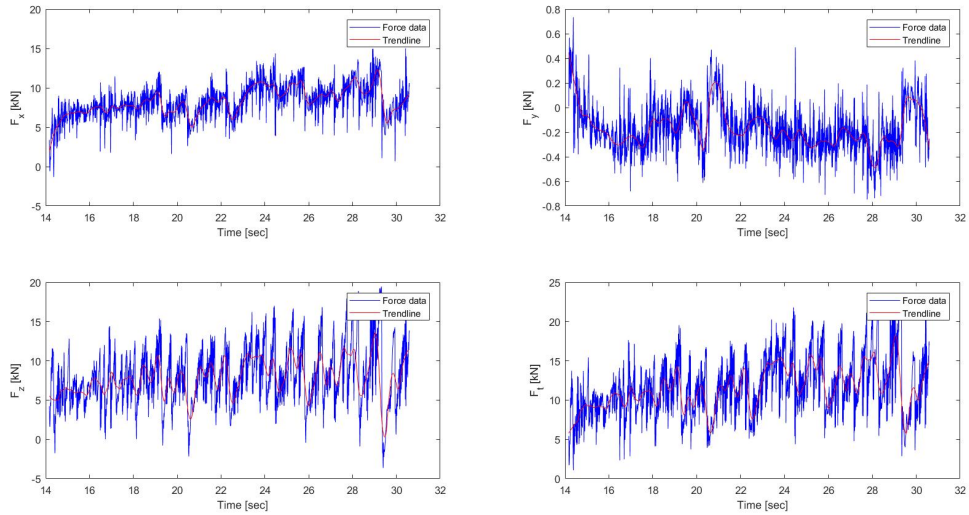

Figure 15: Experiment 9D: force in time

Table 9: Laboratory data of experiment 9D

	Cutting time [sec]	Average depth [cm]	Average width [cm]	Length [m]	Weight [kg]
Experiment 9D	18	0.93	6.55	0.9	0.851

Table 10: Cutting forces of experiment 9D

	$F_{x,max}$ [kN]	$F_{x,mean}$ [kN]	$F_{y,max}$ [kN]	$F_{y,mean}$ [kN]	$F_{z,max}$ [kN]	$F_{z,mean}$ [kN]	$F_{t,max}$ [kN]	$F_{t,mean}$ [kN]
Experiment 9D	15.01	8.18	0.73	-0.16	19.46	7.99	23.58	11.61

.5. EXPERIMENTS 9A-9D: MAXIMUM FORCES OVER DEPTH

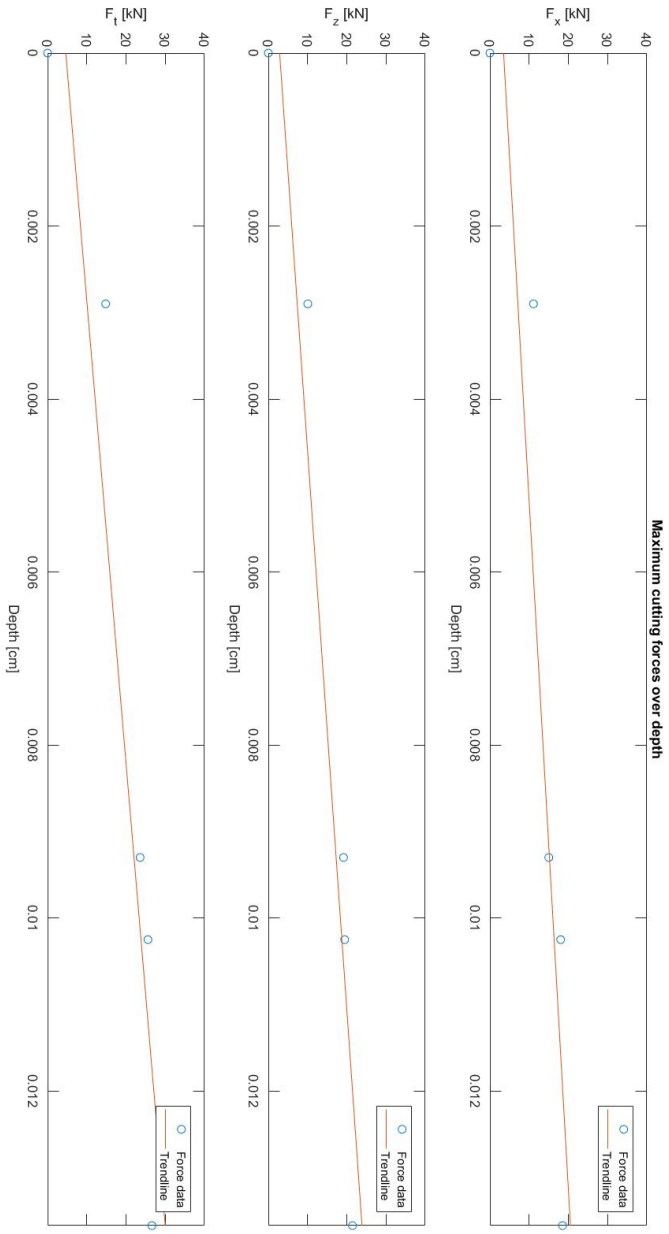

Figure 16: Experiment 5-8: maximum forces over depth

.6. EXPERIMENTS 9A-9D: CUTTING PROFILES

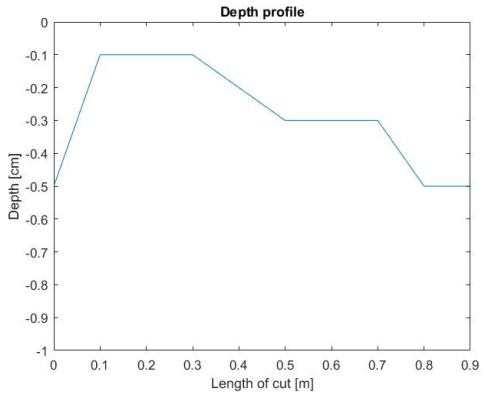

(a) Depth of cut

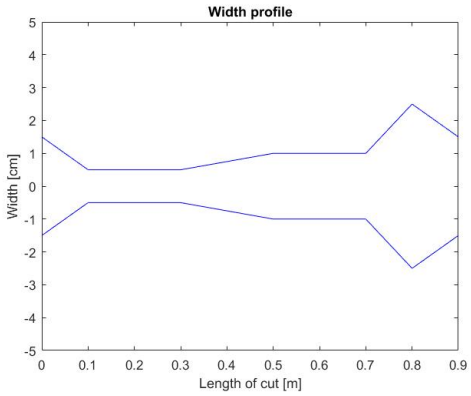

(b) Width of cut

Figure 17: Depth and width of experiment 9A

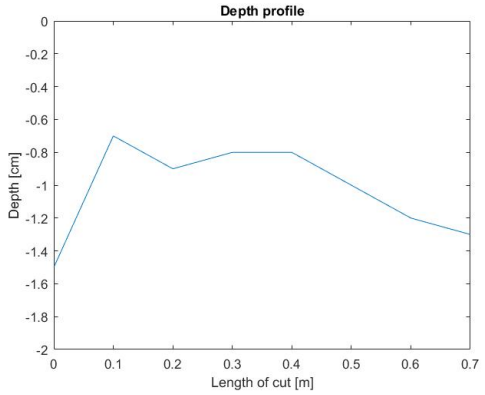

(a) Depth of cut

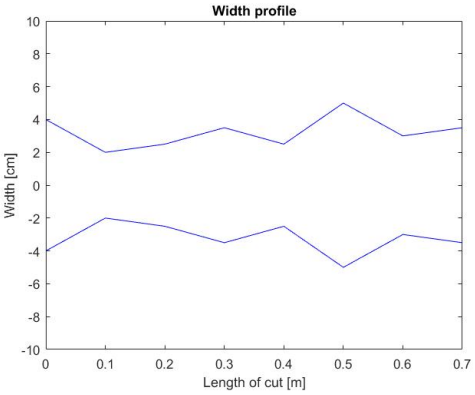

(b) Width of cut

Figure 18: Depth and width of experiment 9B

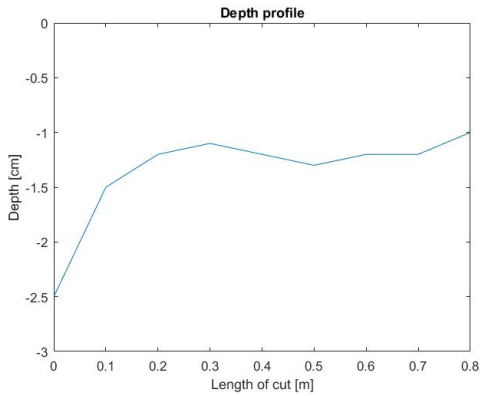

(a) Depth of cut

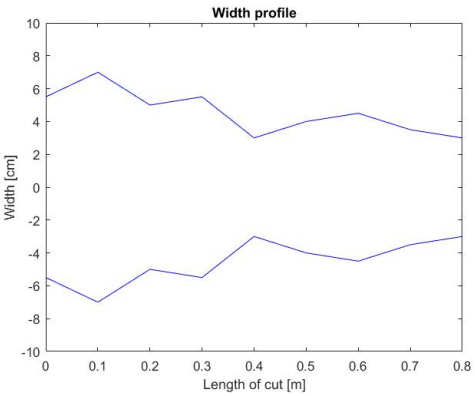

(b) Width of cut

Figure 19: Depth and width of experiment 9C

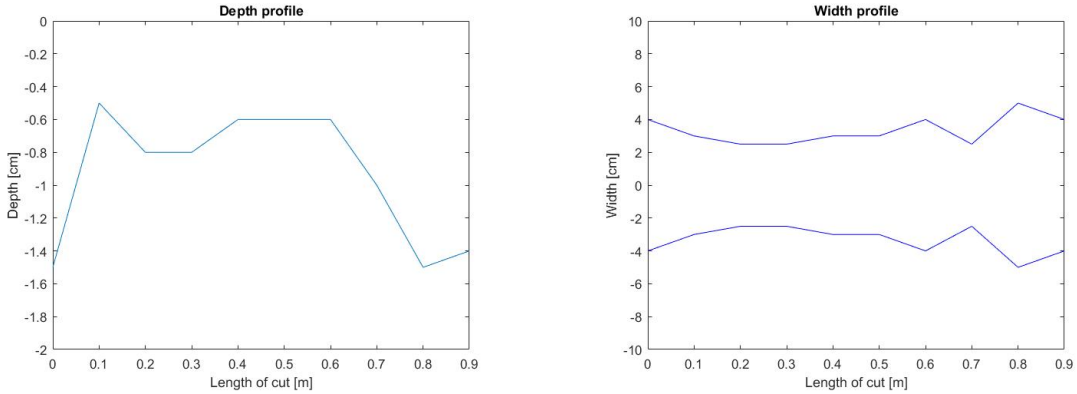

(a) Depth of cut

(b) Width of cut

Figure 20: Depth and width of experiment 9D

.7. EXPERIMENTS 9A-D: PARTICLE SIZE DISTRIBUTIONS

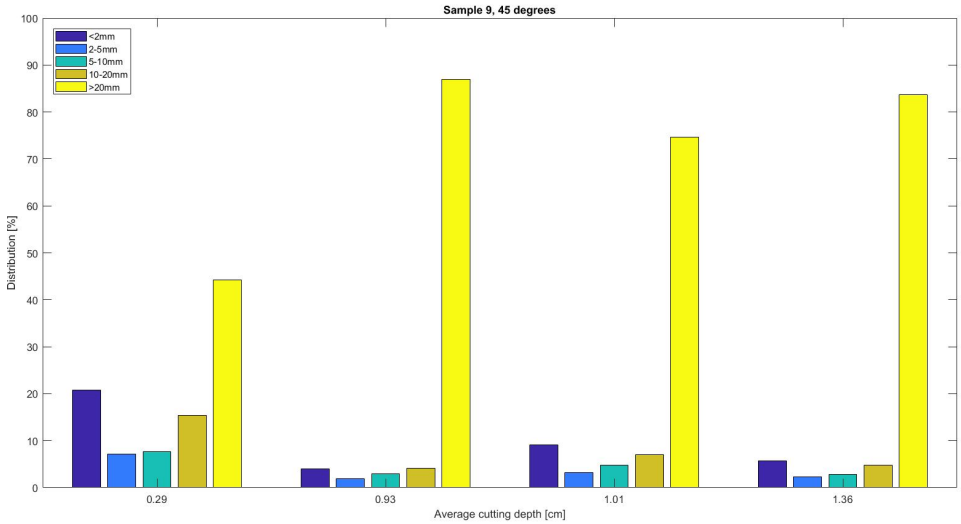

Figure 21: Particle size distributions experiments 5-8

RESULTS OF CUTTING EXPERIMENTS 8A-8D

EXPERIMENTS 8A-8D

For the remaining experiments, the same algorithm as described in chapter 3 is used: for every sample the rock characteristics are listed again first. Afterwards, the force output, together with other relevant data, is given per experiment. Next, the maximum forces are plotted to get an overview of the maximum forces over the depth. Then the cutting profiles are shown together with the particle size distributions.

Table 11: Sample 8: rock characteristics

	F_U	F_B	UCS	BTS	B	E	C	ϕ	δ	ρ
	kN	kN	MPa	MPa	[-]	GPa	MPa	°	°	kg/m^3
Sample 8	41.923	6.004	17.646	1.264	14.014	1.076	5.094	30	21	2302.390

.8. EXPERIMENT 8A

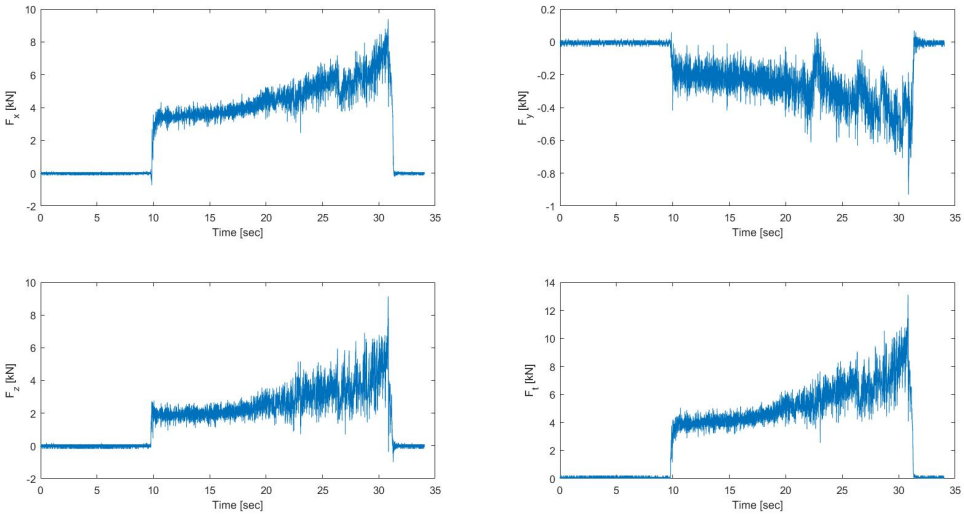

Figure 22: Experiment 8A: force in time

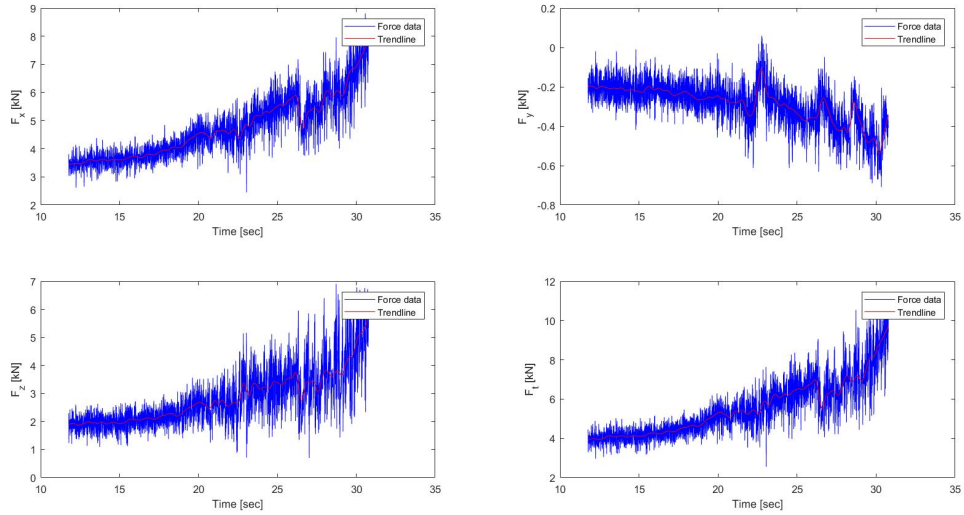

Figure 23: Experiment 8A: force in time

Table 12: Laboratory data of experiment 8A

	Cutting time [sec]	Average depth [cm]	Average width [cm]	Length [m]	Weight [kg]
Experiment 8A	20	0.15	1.41	1	0.043

Table 13: Cutting forces of experiment 8A

	$F_{x,max}$ [kN]	$F_{x,mean}$ [kN]	$F_{y,max}$ [kN]	$F_{y,mean}$ [kN]	$F_{z,max}$ [kN]	$F_{z,mean}$ [kN]	$F_{t,max}$ [kN]	$F_{t,mean}$ [kN]
Experiment 8A	8.81	4.71	0.06	-0.29	6.91	2.85	10.81	5.53

.9. EXPERIMENT 8B

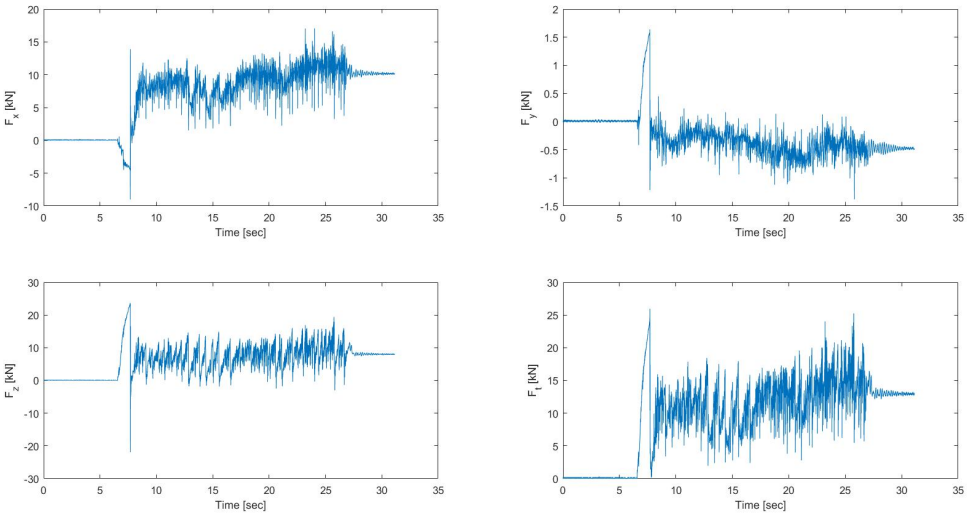

Figure 24: Experiment 8B: force in time

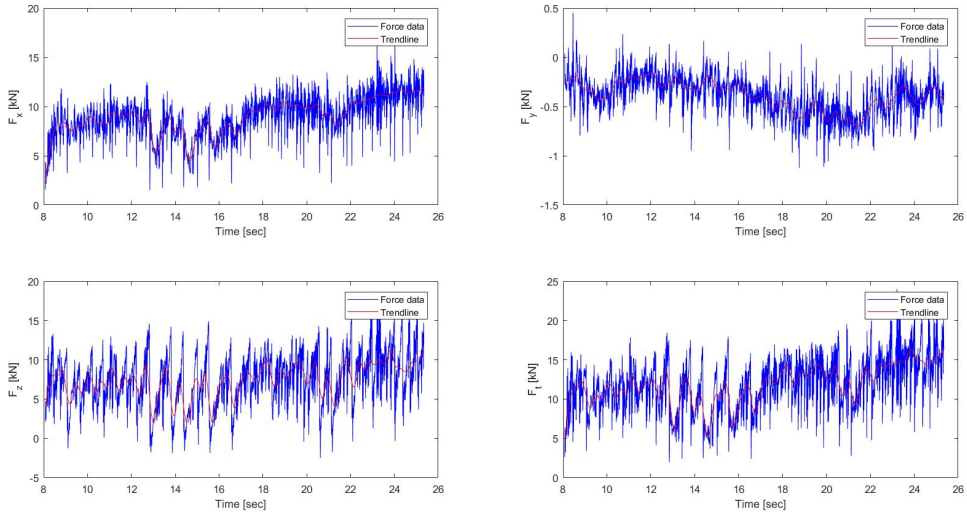

Figure 25: Experiment 8B: force in time

Table 14: Laboratory data of experiment 8B

	Cutting time [sec]	Average depth [cm]	Average width [cm]	Length [m]	Weight [kg]
Experiment 8B	18	0.86	5.70	0.9	0.508

Table 15: Cutting forces of experiment 8B

	$F_{x,max}$ [kN]	$F_{x,mean}$ [kN]	$F_{y,max}$ [kN]	$F_{y,mean}$ [kN]	$F_{z,max}$ [kN]	$F_{z,mean}$ [kN]	$F_{t,max}$ [kN]	$F_{t,mean}$ [kN]
Experiment 8B	17.05	8.84	0.45	-0.39	16.91	7.46	24.01	11.76

.10. EXPERIMENT 8C

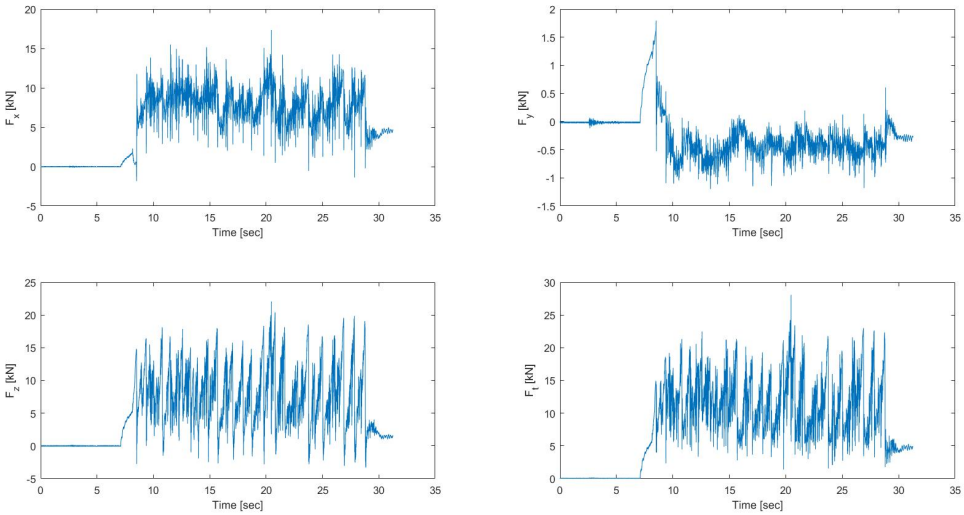

Figure 26: Experiment 8C: force in time

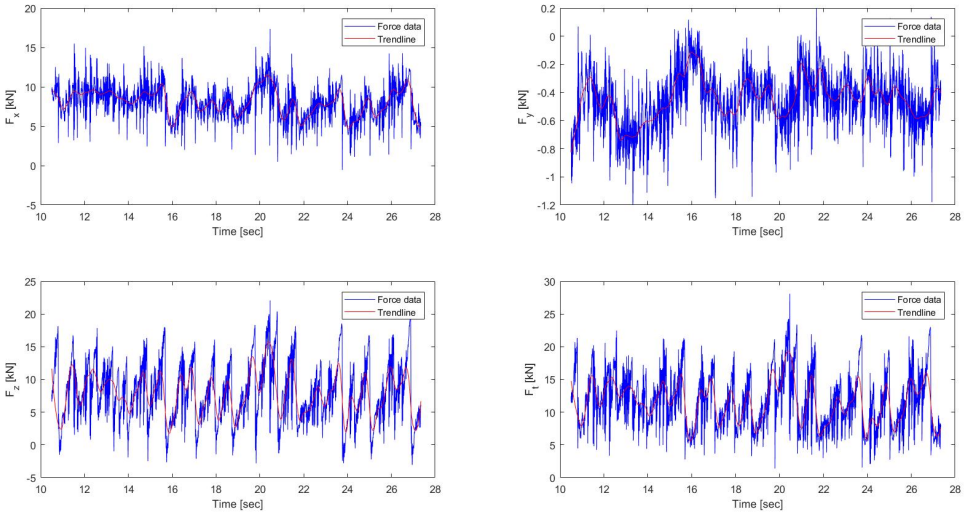

Figure 27: Experiment 8C: force in time

Table 16: Laboratory data of experiment 8C

	Cutting time [sec]	Average depth [cm]	Average width [cm]	Length [m]	Weight [kg]
Experiment 8C	18	1.42	11.90	0.9	1.515

Table 17: Cutting forces of experiment 8C

	$F_{x,max}$ [kN]	$F_{x,mean}$ [kN]	$F_{y,max}$ [kN]	$F_{y,mean}$ [kN]	$F_{z,max}$ [kN]	$F_{z,mean}$ [kN]	$F_{t,max}$ [kN]	$F_{t,mean}$ [kN]
Experiment 8C	17.35	7.99	0.20	-0.45	22.07	7.95	28.08	11.60

.11. EXPERIMENT 8D

Table 18: Average cutting dephs of experiments 8A-8C

	Experiment 8A [cm]	Experiment 8B [cm]	Experiment 8C [cm]
Average cutting depth	0.15	0.86	1.42

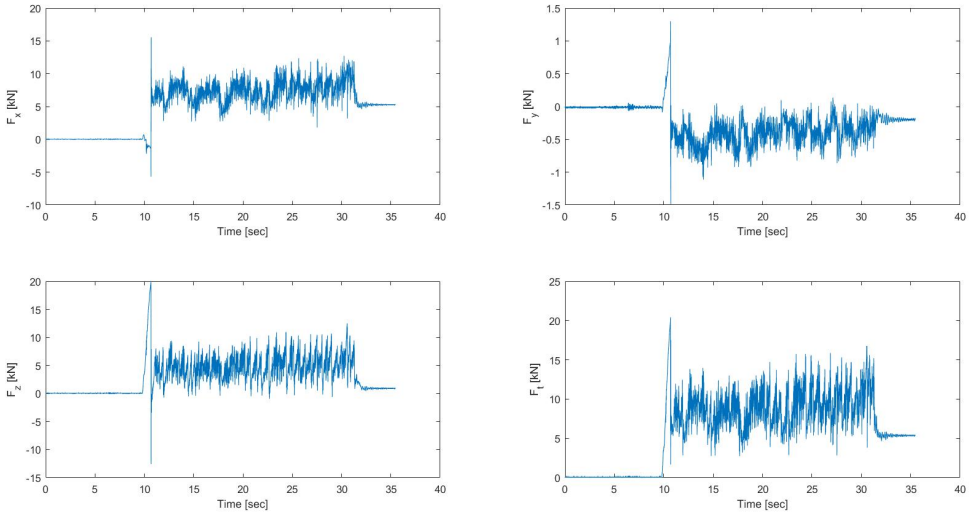

Figure 28: Experiment 8D: force in time

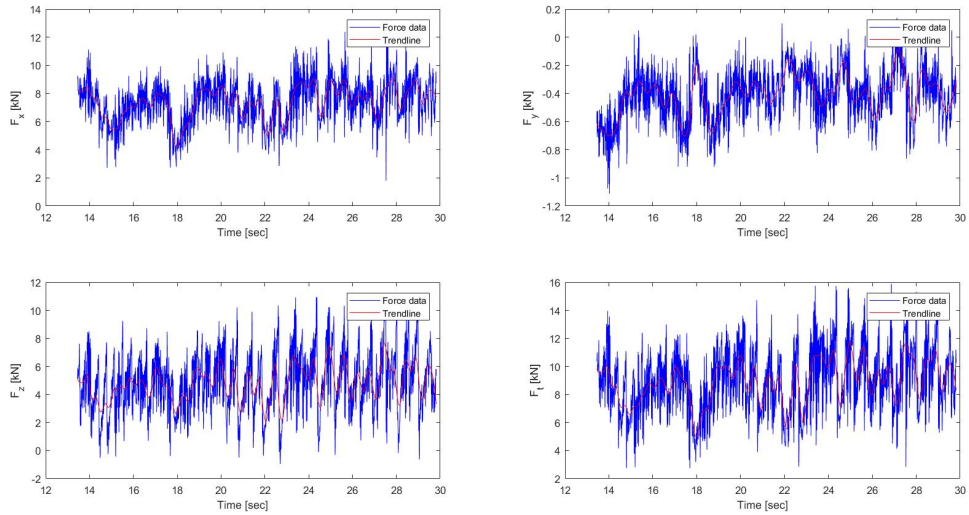

Figure 29: Experiment 8D: force in time

Table 19: Laboratory data of experiment 8D

	Cutting time [sec]	Average depth [cm]	Average width [cm]	Length [m]	Weight [kg]
Experiment 8D	18	0.56	4.80	0.9	0.374

Table 20: Cutting forces of experiment 8D

	$F_{x,max}$ [kN]	$F_{x,mean}$ [kN]	$F_{y,max}$ [kN]	$F_{y,mean}$ [kN]	$F_{z,max}$ [kN]	$F_{z,mean}$ [kN]	$F_{t,max}$ [kN]	$F_{t,mean}$ [kN]
Experiment 8D	12.37	7.34	0.14	-0.41	10.95	4.83	15.88	8.90

.12. EXPERIMENTS 8A-8D: MAXIMUM FORCES OVER DEPTH

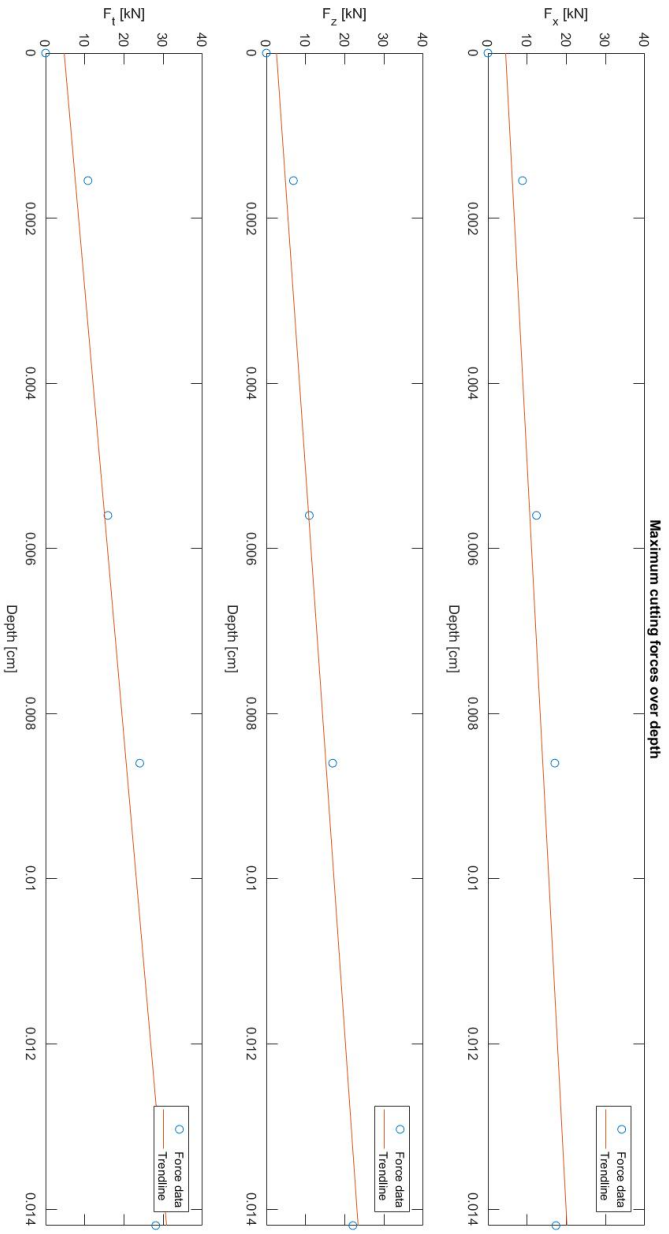

Figure 30: Experiment 9-12: maximum forces over depth

.13. EXPERIMENTS 8A-8D: CUTTING PROFILES

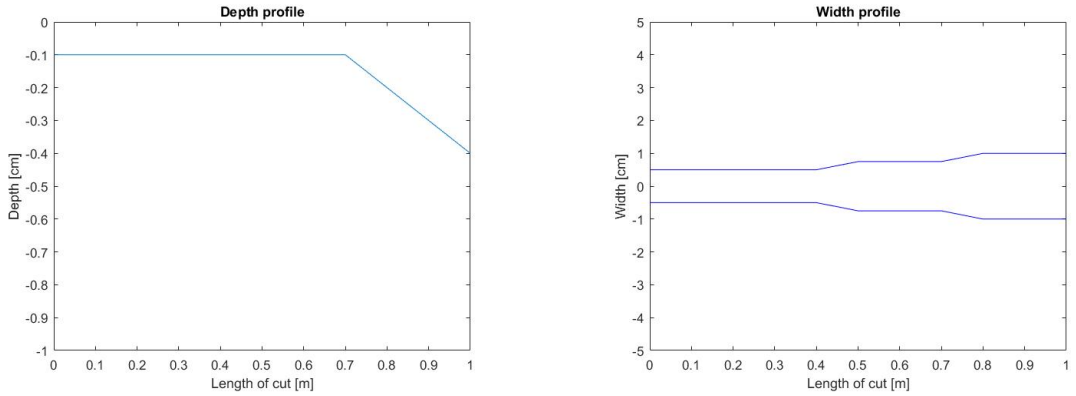

(a) Depth of cut (b) Width of cut

Figure 31: Depth and width of experiment 8A

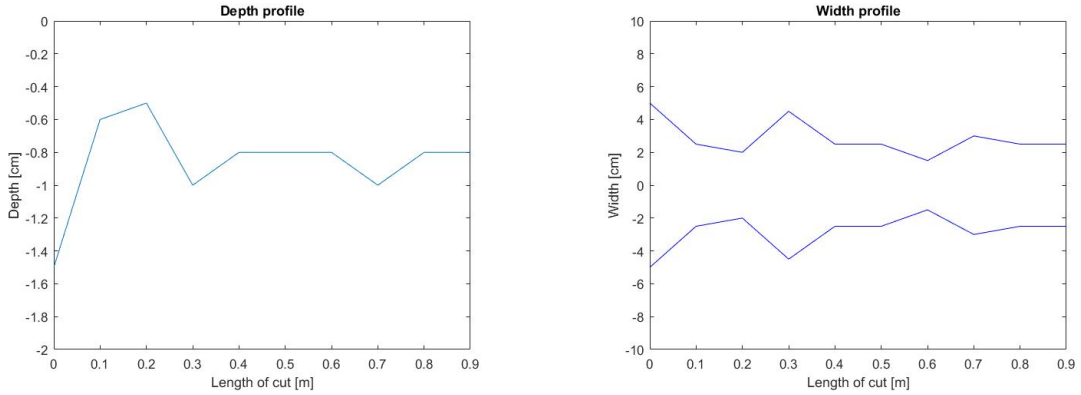

(a) Depth of cut (b) Width of cut

Figure 32: Depth and width of experiment 8B

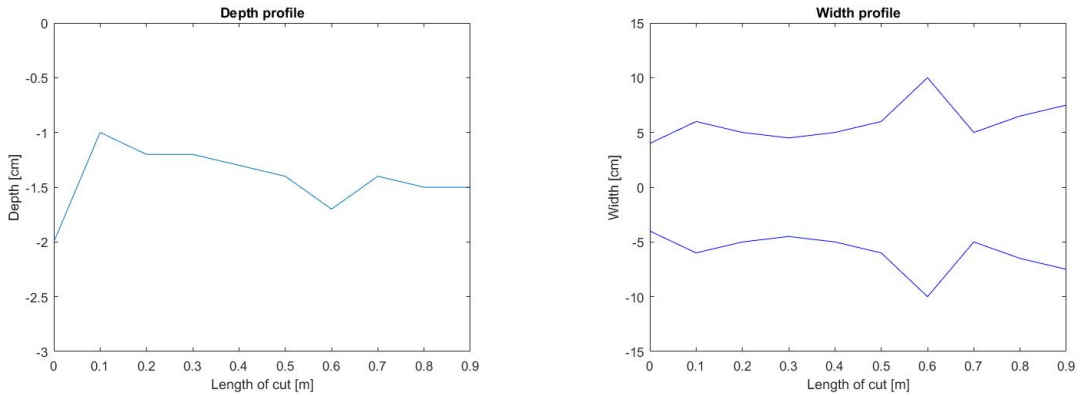

(a) Depth of cut (b) Width of cut

Figure 33: Depth and width of experiment 8C

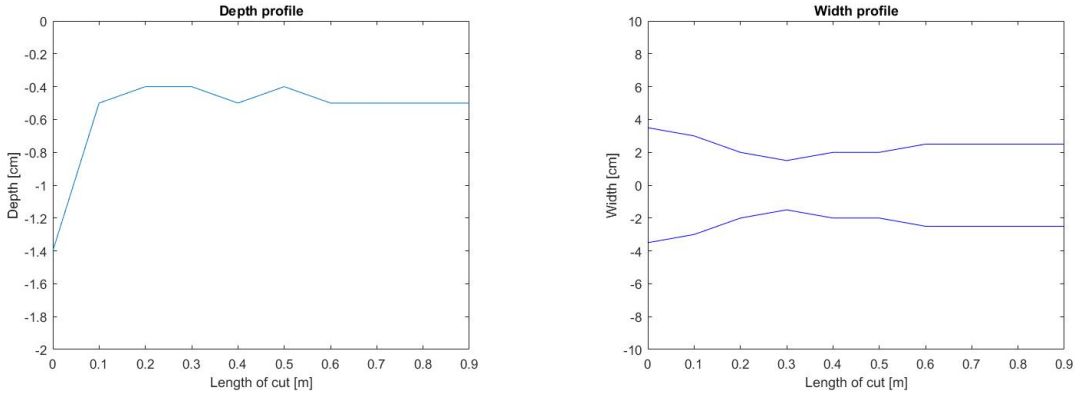

(a) Depth of cut

(b) Width of cut

Figure 34: Depth and width of experiment 8D

.14. EXPERIMENTS 8A-8D: PARTICLE SIZE DISTRIBUTIONS

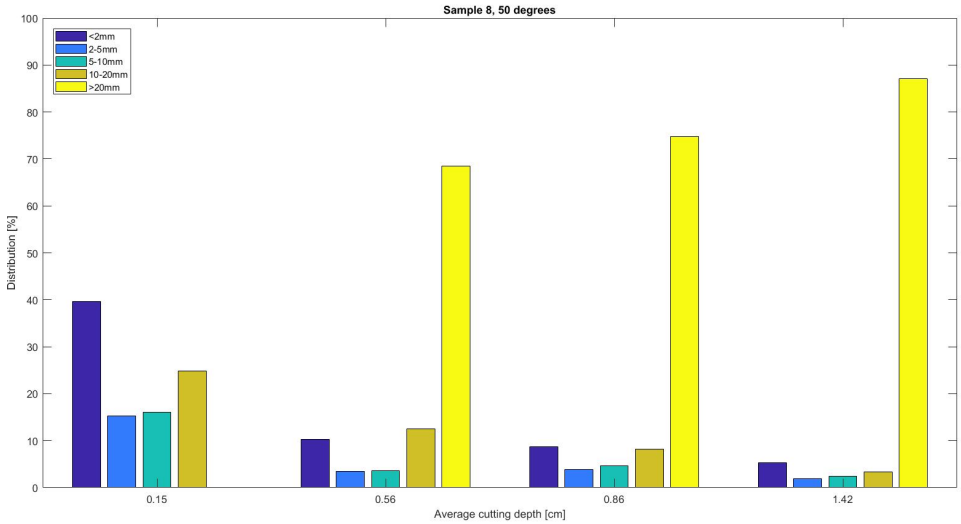

Figure 35: Particle size distributions experiments 9-12

RESULTS OF CUTTING EXPERIMENTS 6A-6C

EXPERIMENTS 6A-6C

For the remaining experiments, the same algorithm as described in chapter 3 is used: for every sample the rock characteristics are listed again first. Afterwards, the force output, together with other relevant data, is given per experiment. Next, the maximum forces are plotted to get an overview of the maximum forces over the depth. Then the cutting profiles are shown together with the particle size distributions.

Table 21: Sample 6: rock characteristics

	F_U	F_B	UCS	BTS	B	E	C	ϕ	δ	ρ
	kN	kN	MPa	MPa	[-]	GPa	MPa	°	°	kg/m^3
Sample 6	40.206	5.395	16.923	1.135	15.220	1.756	4.885	30	20	2294.631

.15. EXPERIMENT 6A

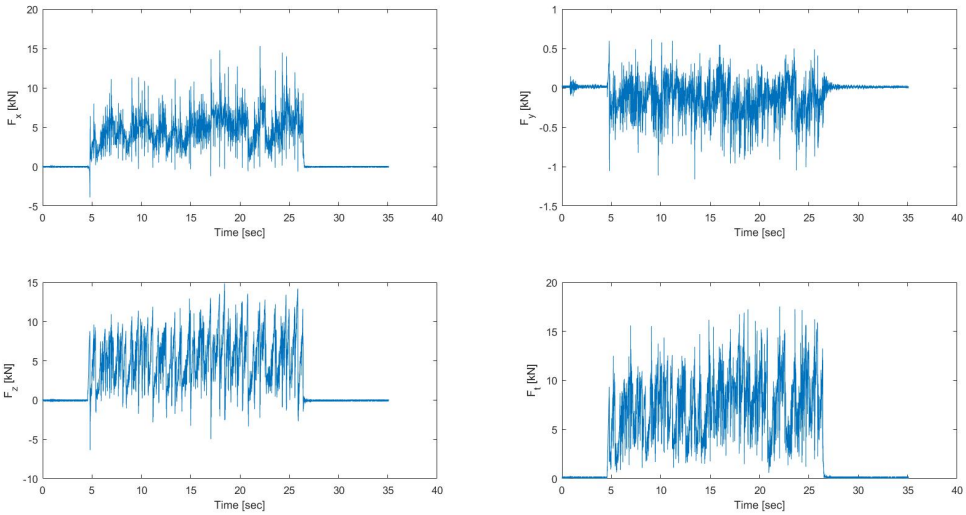

Figure 36: Experiment 6A: force in time

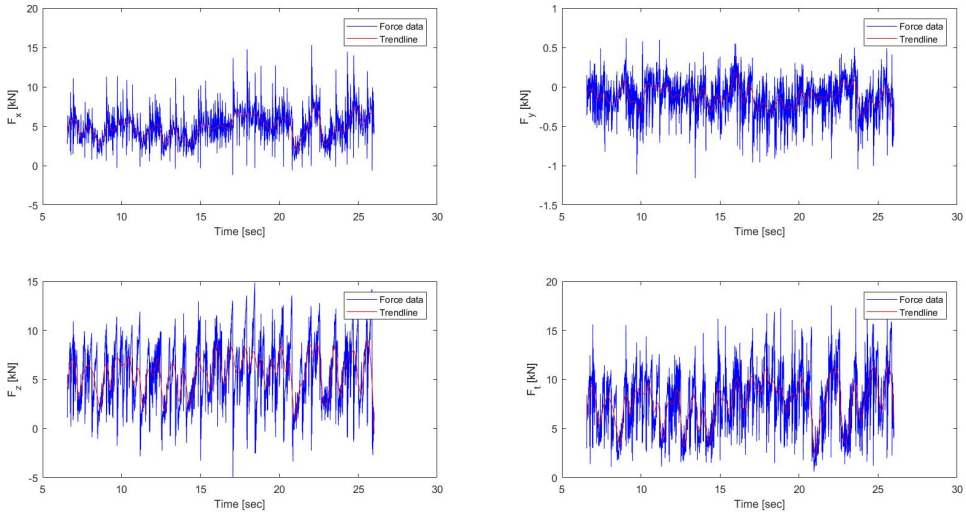

Figure 37: Experiment 6A: force in time

Table 22: Laboratory data of experiment 6A

	Cutting time [sec]	Average depth [cm]	Average width [cm]	Length [m]	Weight [kg]
Experiment 6A	20	0.62	6.27	1	0.618

Table 23: Cutting forces of experiment 6A

	$F_{x,max}$ [kN]	$F_{x,mean}$ [kN]	$F_{y,max}$ [kN]	$F_{y,mean}$ [kN]	$F_{z,max}$ [kN]	$F_{z,mean}$ [kN]	$F_{t,max}$ [kN]	$F_{t,mean}$ [kN]
Experiment 6A	15.32	4.94	0.62	-0.14	14.87	5.59	17.54	7.73

.16. EXPERIMENT 6B

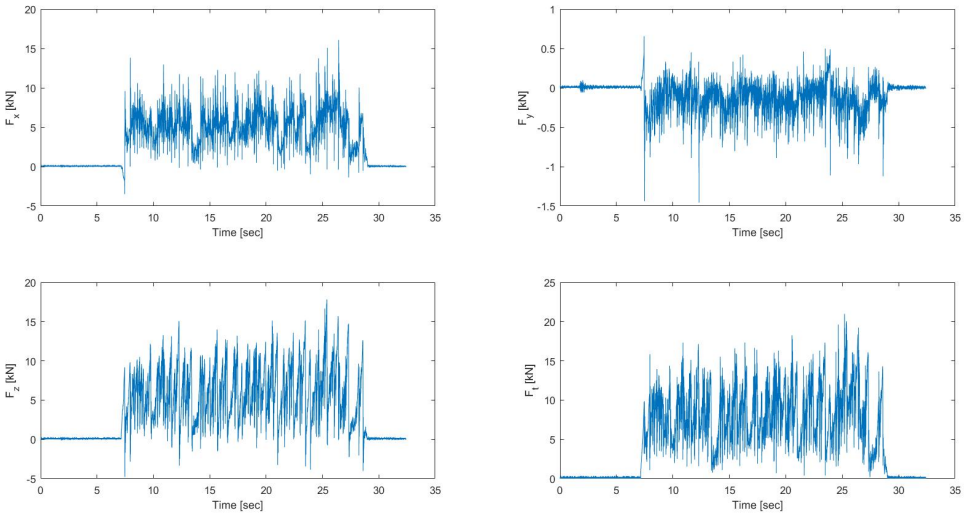

Figure 38: Experiment 6B: force in time

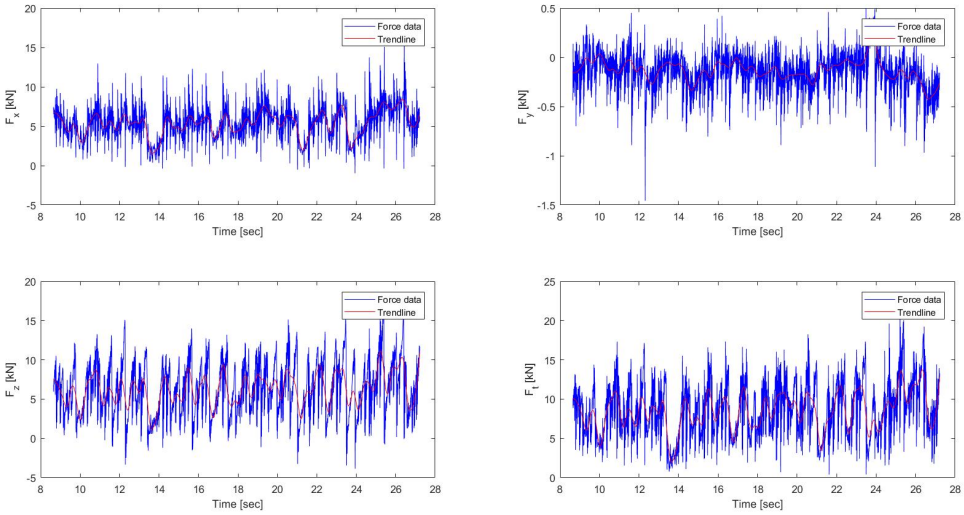

Figure 39: Experiment 6B: force in time

Table 24: Laboratory data of experiment 6B

	Cutting time [sec]	Average depth [cm]	Average width [cm]	Length [m]	Weight [kg]
Experiment 6B	20	0.98	7.64	1	0.868

Table 25: Cutting forces of experiment 6B

	$F_{x,max}$ [kN]	$F_{x,mean}$ [kN]	$F_{y,max}$ [kN]	$F_{y,mean}$ [kN]	$F_{z,max}$ [kN]	$F_{z,mean}$ [kN]	$F_{t,max}$ [kN]	$F_{t,mean}$ [kN]
Experiment 6B	16.08	5.39	0.50	-0.15	17.81	6.23	20.98	8.48

.17. EXPERIMENT 6C

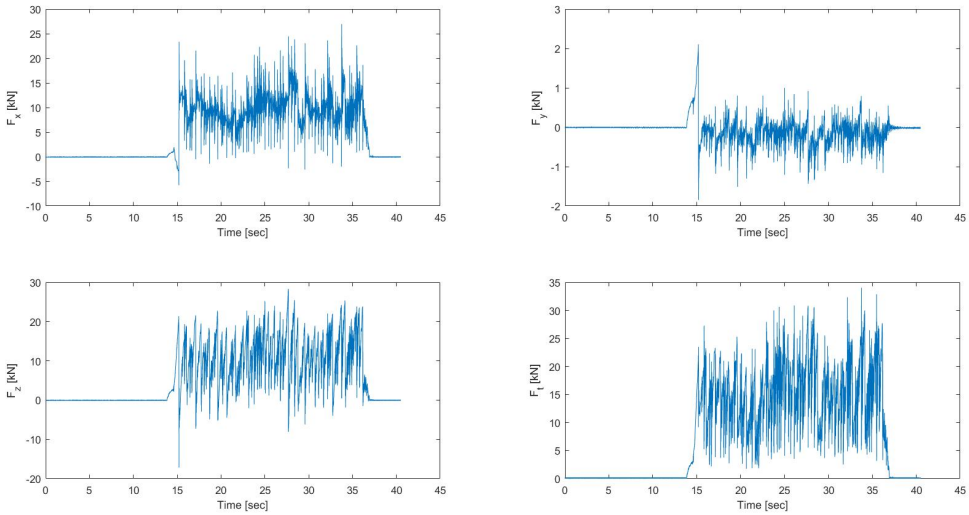

Figure 40: Experiment 6C: force in time

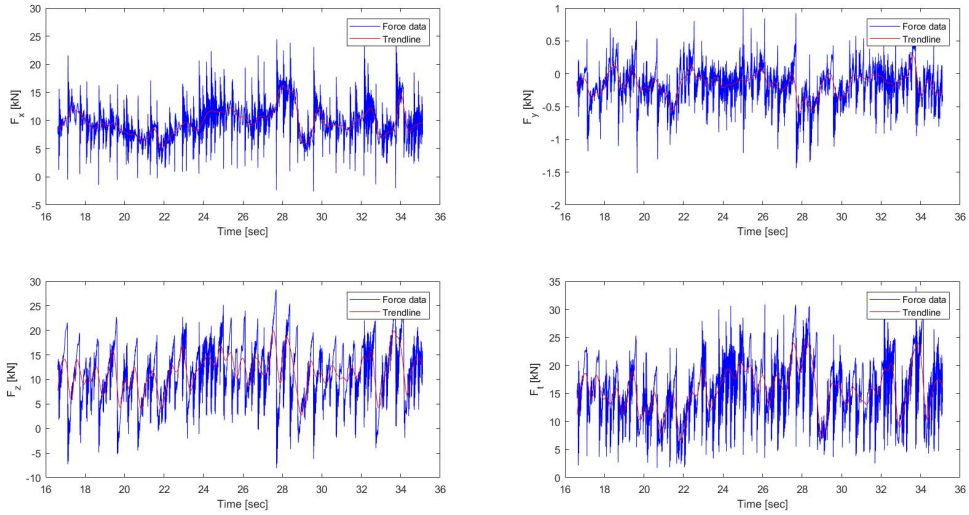

Figure 41: Experiment 6C: force in time

Table 26: Laboratory data of experiment 6C

	Cutting time [sec]	Average depth [cm]	Average width [cm]	Length [m]	Weight [kg]
Experiment 6C	20	1.59	10.45	1	1.553

Table 27: Cutting forces of experiment 6C

	$F_{x,max}$ [kN]	$F_{x,mean}$ [kN]	$F_{y,max}$ [kN]	$F_{y,mean}$ [kN]	$F_{z,max}$ [kN]	$F_{z,mean}$ [kN]	$F_{t,max}$ [kN]	$F_{t,mean}$ [kN]
Experiment 6C	26.95	9.71	1.00	-0.17	28.31	11.24	34.02	15.39

.18. EXPERIMENTS 6A-6C: MAXIMUM FORCES OVER DEPTH

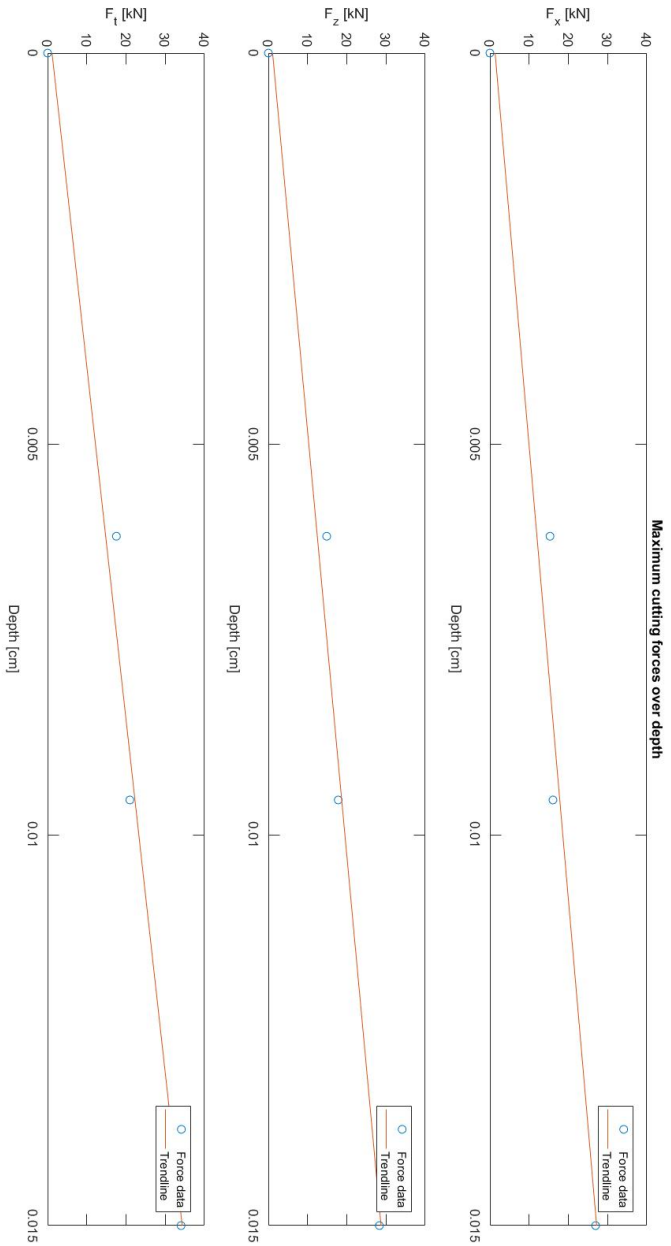

Figure 42: Experiment 13-15: maximum forces over depth

.19. EXPERIMENTS 6A-6C: MAXIMUM FORCES OVER DEPTH

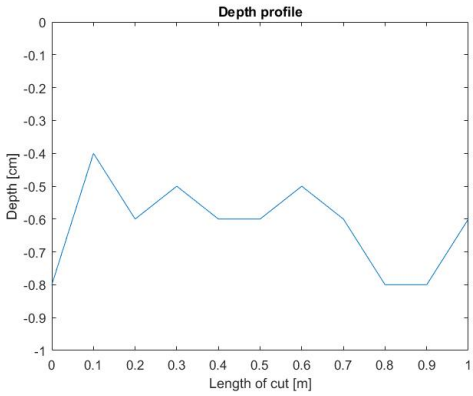

(a) Depth of cut

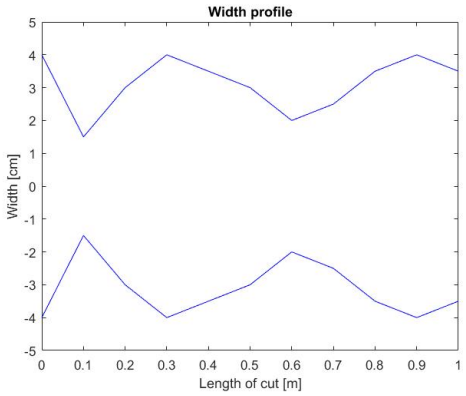

(b) Width of cut

Figure 43: Depth and width of experiment 6A

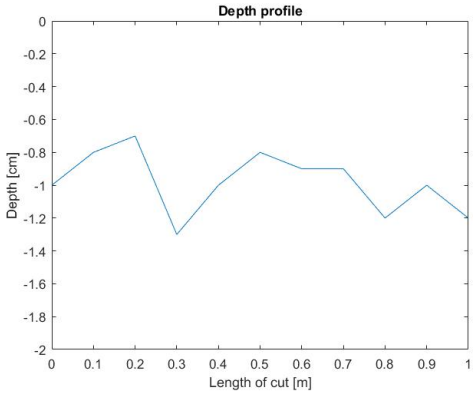

(a) Depth of cut

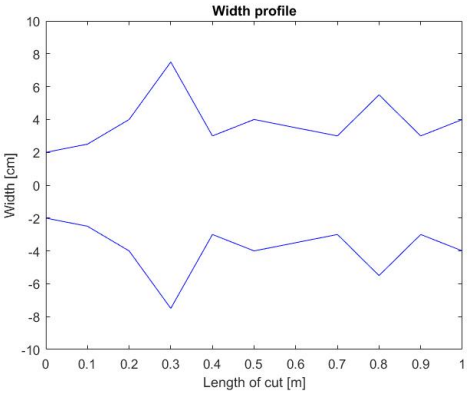

(b) Width of cut

Figure 44: Depth and width of experiment 6B

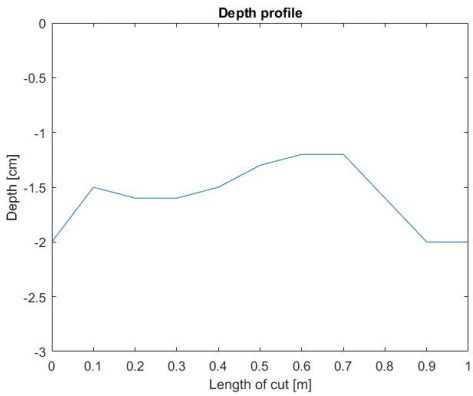

(a) Depth of cut

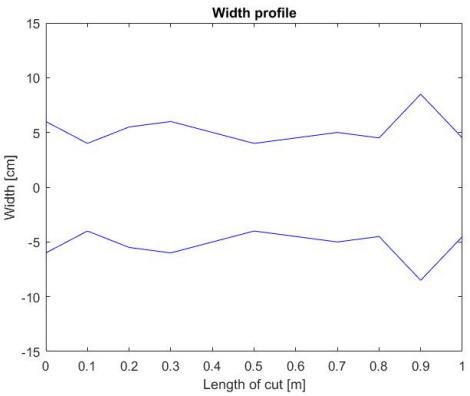

(b) Width of cut

Figure 45: Depth and width of experiment 6C

.20. EXPERIMENTS 6A-6C: PARTICLE SIZE DISTRIBUTIONS

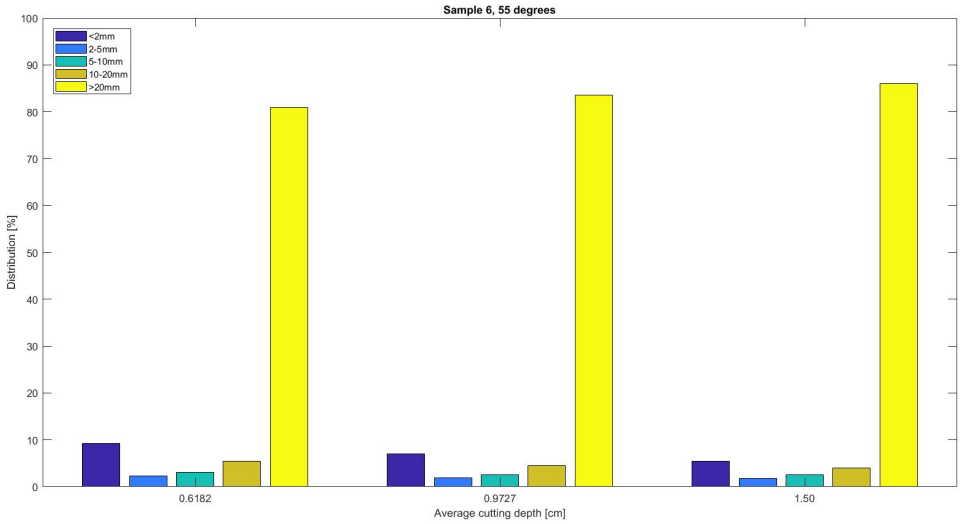

Figure 46: Particle size distributions experiments 13-15

RESULTS OF CUTTING EXPERIMENTS 7A-7C

EXPERIMENTS 7A-7C

For the remaining experiments, the same algorithm as described in chapter 3 is used: for every sample the rock characteristics are listed again first. Afterwards, the force output, together with other relevant data, is given per experiment. Next, the maximum forces are plotted to get an overview of the maximum forces over the depth. Then the cutting profiles are shown together with the particle size distributions.

Table 28: Sample 7: rock characteristics

	F_U	F_B	UCS	BTS	B	E	C	ϕ	δ	ρ
	kN	kN	MPa	MPa	[-]	GPa	MPa	°	°	kg/m^3
Sample 7	48.573	8.021	20.445	1.688	12.083	0.928	5.784	31	21	2369.662

.21. EXPERIMENT 7A

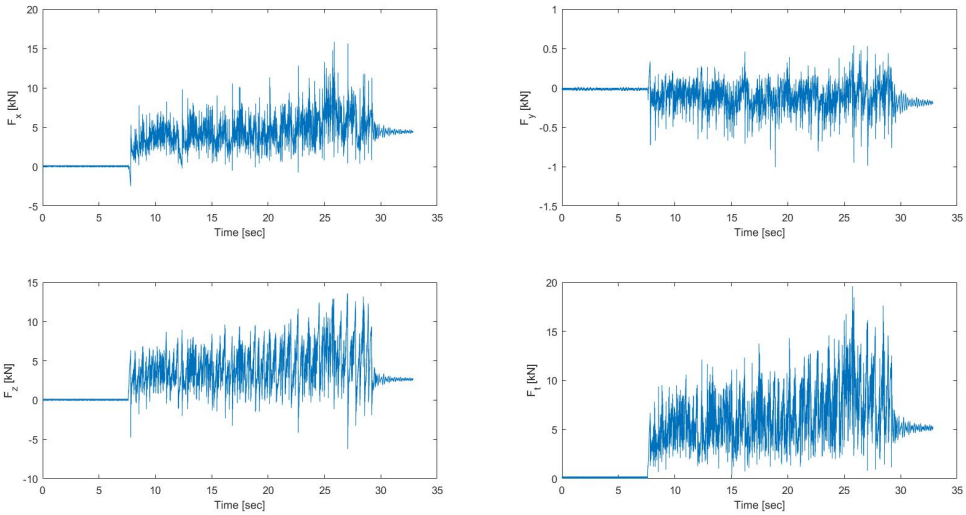

Figure 47: Experiment 7A: force in time

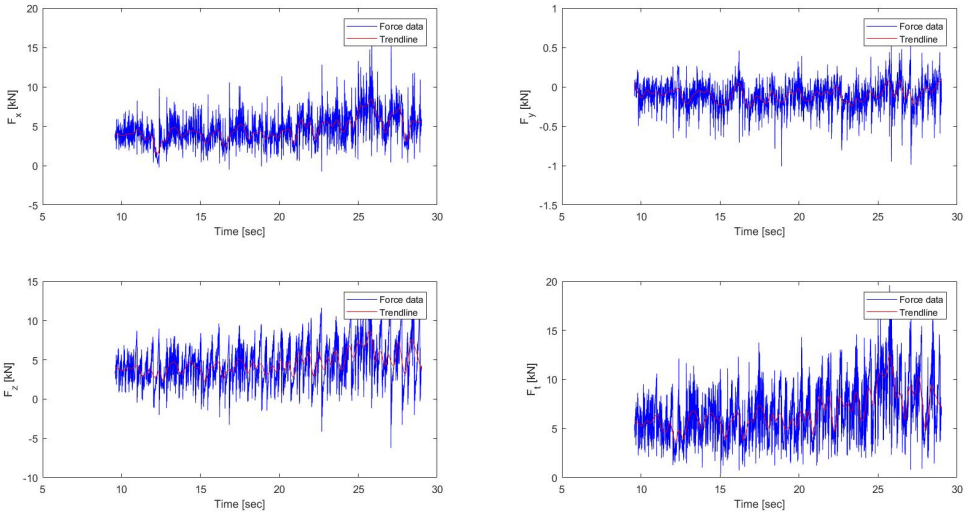

Figure 48: Experiment 7A: force in time

Table 29: Laboratory data of experiment 7A

	Cutting time [sec]	Average depth [cm]	Average width [cm]	Length [m]	Weight [kg]
Experiment 7A	20	0.50	4.18	1	0.237

Table 30: Cutting forces of experiment 7A

	$F_{x,max}$ [kN]	$F_{x,mean}$ [kN]	$F_{y,max}$ [kN]	$F_{y,mean}$ [kN]	$F_{z,max}$ [kN]	$F_{z,mean}$ [kN]	$F_{t,max}$ [kN]	$F_{t,mean}$ [kN]
Experiment 7A	15.84	4.66	0.54	-0.11	13.58	4.52	19.60	6.69

.22. EXPERIMENT 7B

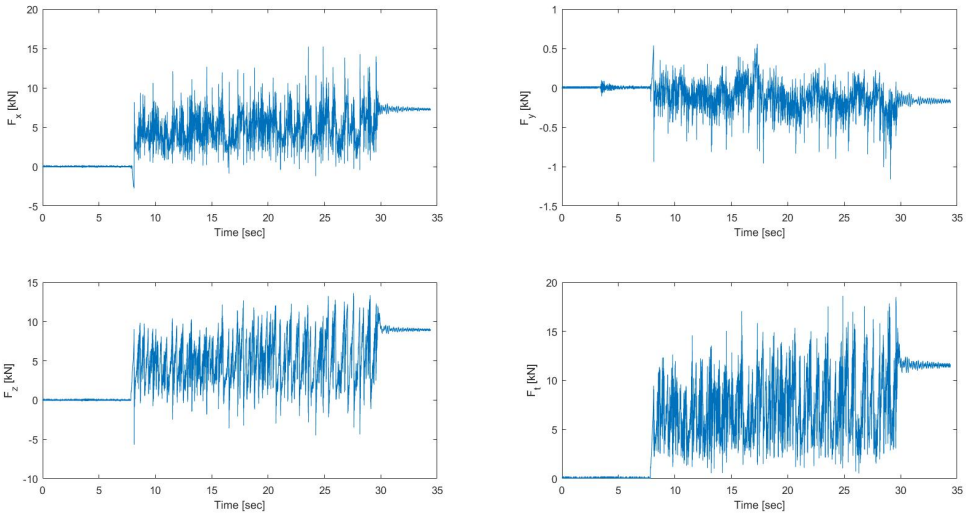

Figure 49: Experiment 7B: force in time

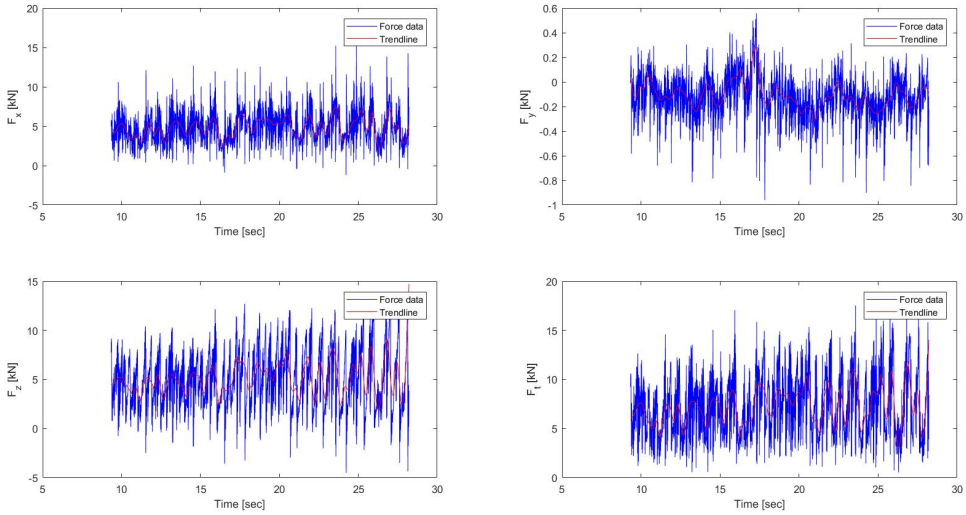

Figure 50: Experiment 7B: force in time

Table 31: Laboratory data of experiment 7B

	Cutting time [sec]	Average depth [cm]	Average width [cm]	Length [m]	Weight [kg]
Experiment 7B	20	0.71	5.82	1	0.391

Table 32: Cutting forces of experiment 7B

	$F_{x,max}$ [kN]	$F_{x,mean}$ [kN]	$F_{y,max}$ [kN]	$F_{y,mean}$ [kN]	$F_{z,max}$ [kN]	$F_{z,mean}$ [kN]	$F_{t,max}$ [kN]	$F_{t,mean}$ [kN]
Experiment 7B	15.23	4.82	0.56	-0.12	13.63	5.03	18.62	7.21

.23. EXPERIMENT 7C

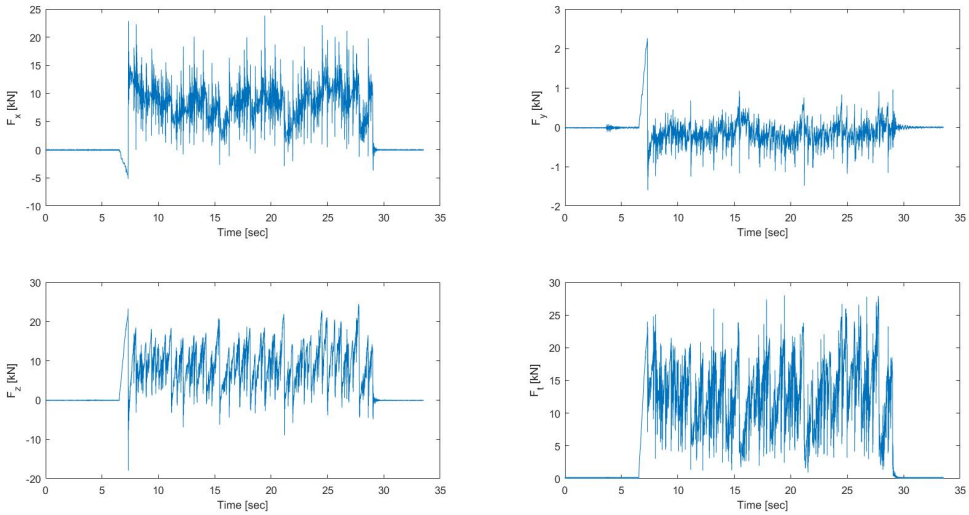

Figure 51: Experiment 7C: force in time

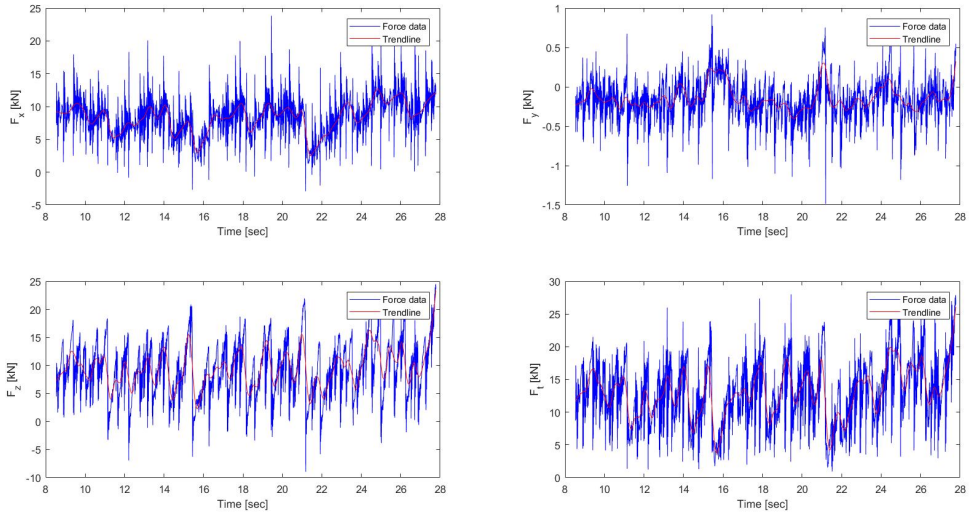

Figure 52: Experiment 7C: force in time

Table 33: Laboratory data of experiment 7C

	Cutting time [sec]	Average depth [cm]	Average width [cm]	Length [m]	Weight [kg]
Experiment 7C	18	1.36	10.40	0.9	1.298

Table 34: Cutting forces of experiment 7C

	$F_{x,max}$ [kN]	$F_{x,mean}$ [kN]	$F_{y,max}$ [kN]	$F_{y,mean}$ [kN]	$F_{z,max}$ [kN]	$F_{z,mean}$ [kN]	$F_{t,max}$ [kN]	$F_{t,mean}$ [kN]
Experiment 7C	23.83	8.37	0.92	-0.16	24.49	9.25	28.00	12.89

.24. EXPERIMENTS 7A-7C: MAXIMUM FORCES OVER DEPTH

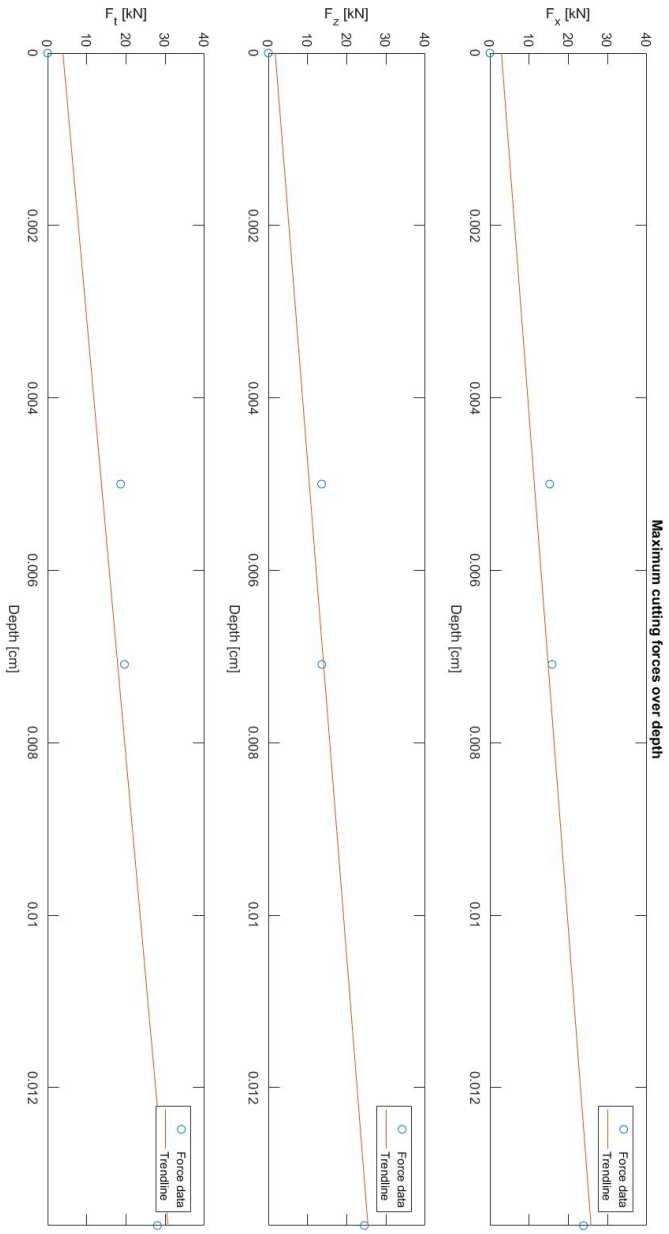

Figure 53: Experiment 16-18: maximum forces over depth

.25. EXPERIMENTS 7A-7C: CUTTING PROFILES

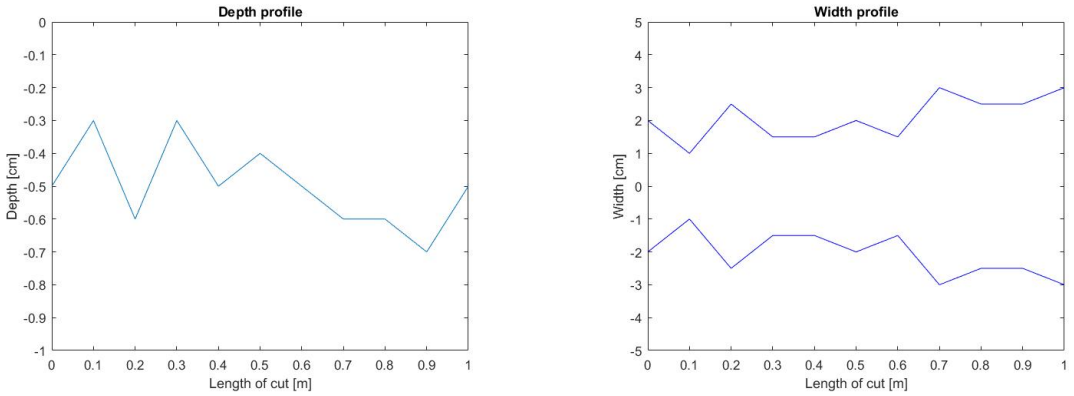

(a) Depth of cut (b) Width of cut

Figure 54: Depth and width of experiment 7A

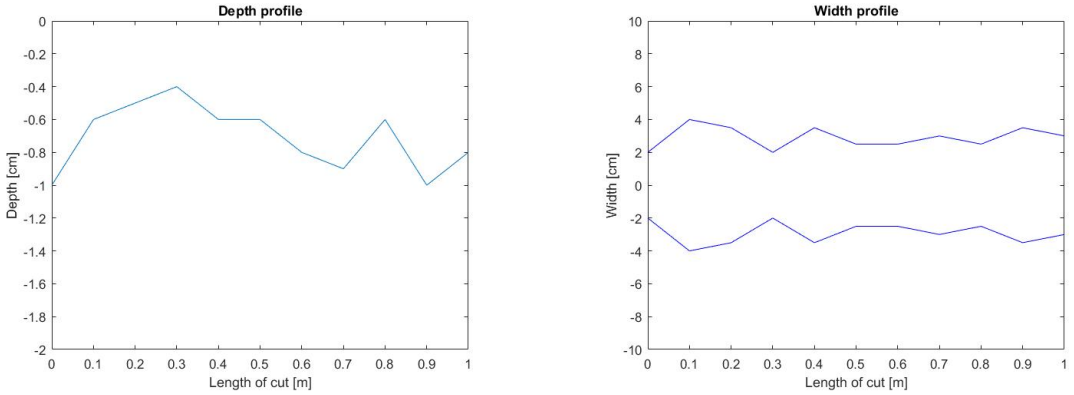

(a) Depth of cut (b) Width of cut

Figure 55: Depth and width of experiment 7B

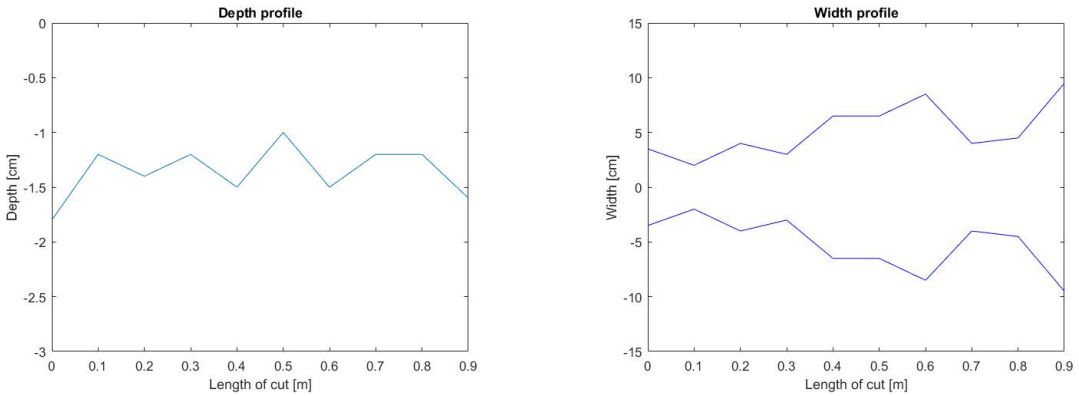

(a) Depth of cut (b) Width of cut

Figure 56: Depth and width of experiment 7C

.26. EXPERIMENTS 7A-7C: PARTICLE SIZE DISTRIBUTIONS

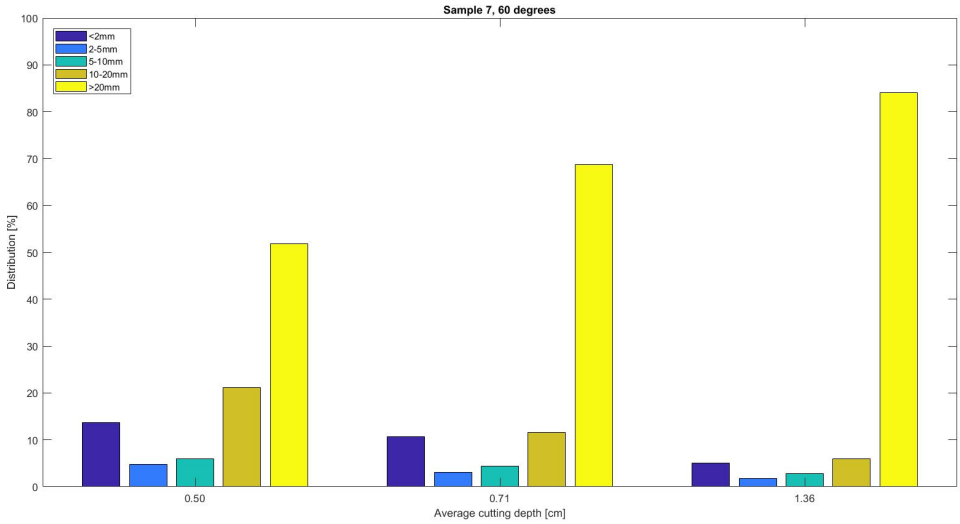

Figure 57: Particle size distributions experiments 16-18

RESULTS OF CUTTING EXPERIMENTS 7.2A-7.2C

EXPERIMENTS 7.2A-7.2C

For the remaining experiments, the same algorithm as described in chapter 3 is used: for every sample the rock characteristics are listed again first. Afterwards, the force output, together with other relevant data, is given per experiment. Next, the maximum forces are plotted to get an overview of the maximum forces over the depth. Then the cutting profiles are shown together with the particle size distributions.

Table 35: Sample 7.2: rock characteristics

	F_U	F_B	UCS	BTS	B	E	C	ϕ	δ	ρ
	kN	kN	MPa	MPa	[-]	GPa	MPa	°	°	kg/m^3
Sample 7.2	48.573	8.021	20.445	1.688	12.083	0.928	5.784	31	21	2369.662

.27. EXPERIMENT 7.2A

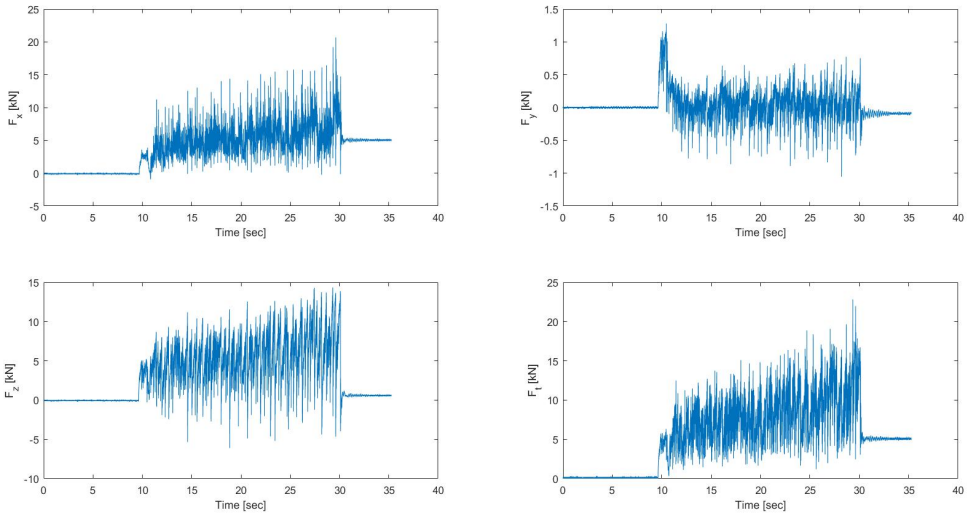

Figure 58: Experiment 7.2A: force in time

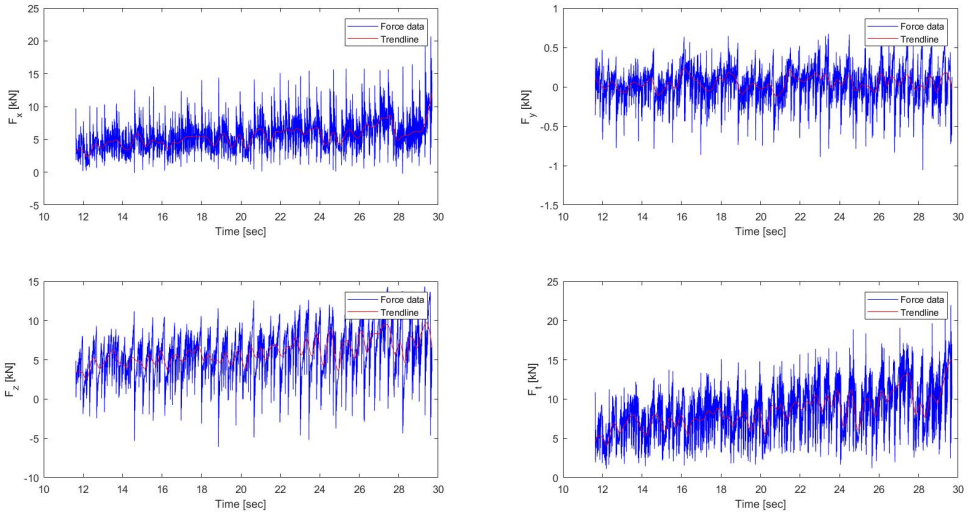

Figure 59: Experiment 7.2A: force in time

Table 36: Laboratory data of experiment 7.2A

	Cutting time [sec]	Average depth [cm]	Average width [cm]	Length [m]	Weight [kg]
Experiment 7.2A	18	0.50	3.5	0.9	0.212

Table 37: Cutting forces of experiment 7.2A

	$F_{x,max}$ [kN]	$F_{x,mean}$ [kN]	$F_{y,max}$ [kN]	$F_{y,mean}$ [kN]	$F_{z,max}$ [kN]	$F_{z,mean}$ [kN]	$F_{t,max}$ [kN]	$F_{t,mean}$ [kN]
Experiment 7.2A	20.67	5.57	0.77	0.03	14.34	5.72	22.80	8.32

.28. EXPERIMENT 7.2B

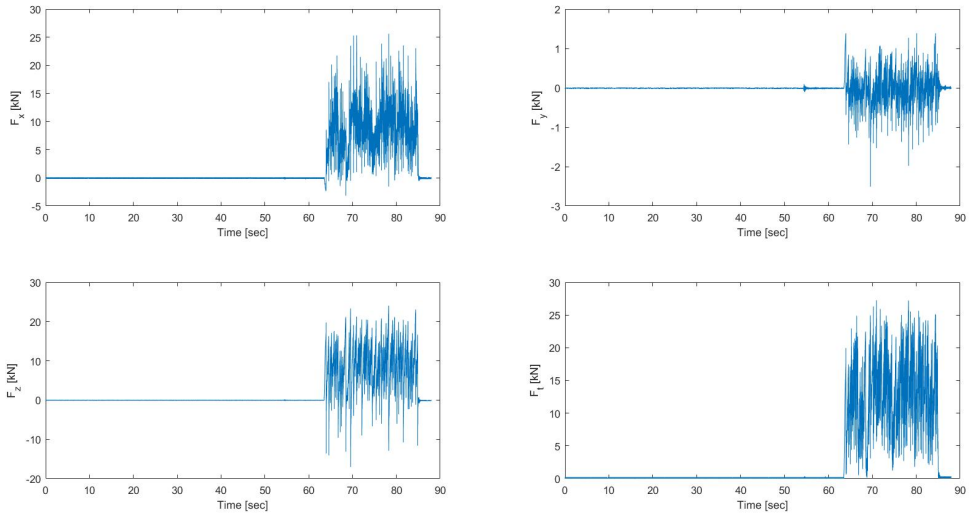

Figure 60: Experiment 7.2B: force in time

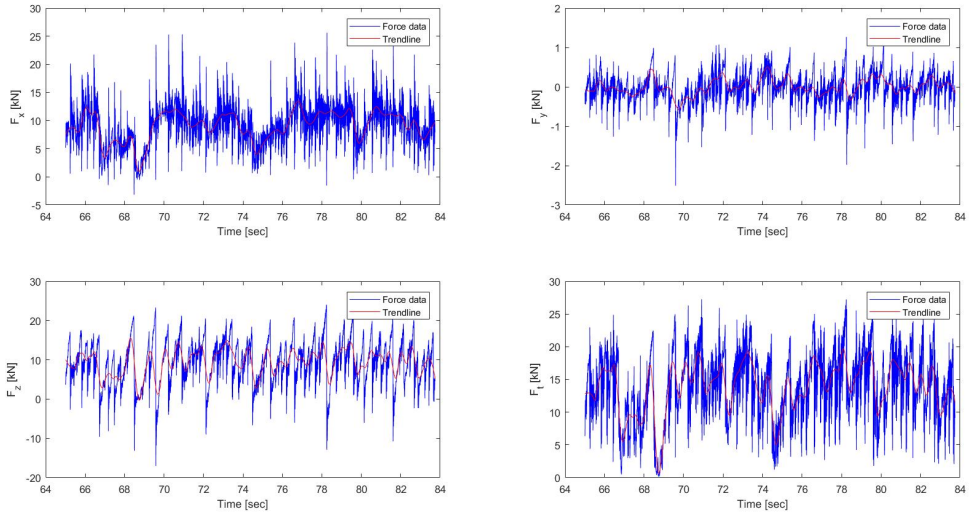

Figure 61: Experiment 7.2B: force in time

Table 38: Laboratory data of experiment 7.2B

	Cutting time [sec]	Average depth [cm]	Average width [cm]	Length [m]	Weight [kg]
Experiment 7.2B	20	1.06	10.09	1	0.438

Table 39: Cutting forces of experiment 7.2B

	$F_{x,max}$ [kN]	$F_{x,mean}$ [kN]	$F_{y,max}$ [kN]	$F_{y,mean}$ [kN]	$F_{z,max}$ [kN]	$F_{z,mean}$ [kN]	$F_{t,max}$ [kN]	$F_{t,mean}$ [kN]
Experiment 7.2B	25.61	9.13	1.39	-0.02	24.04	9.25	27.25	13.69

.29. EXPERIMENT 7.2C

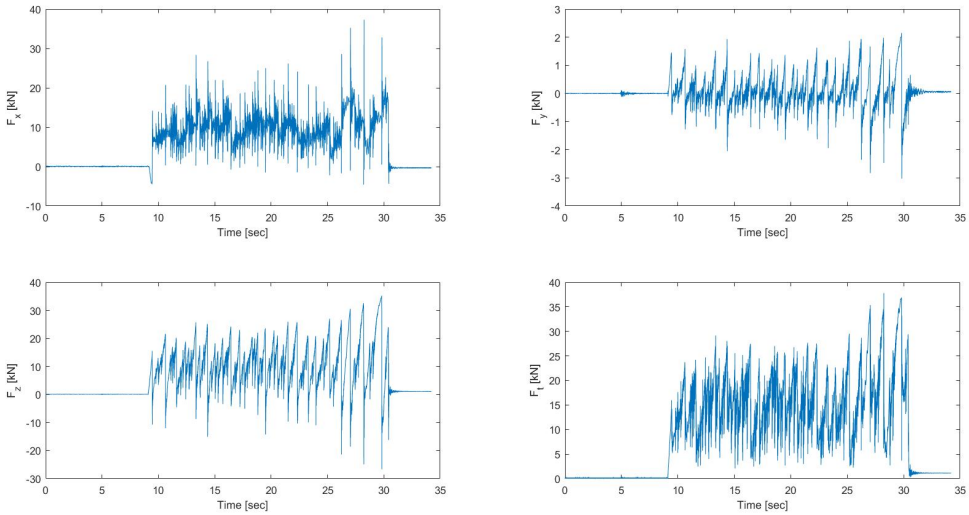

Figure 62: Experiment 7.2C: force in time

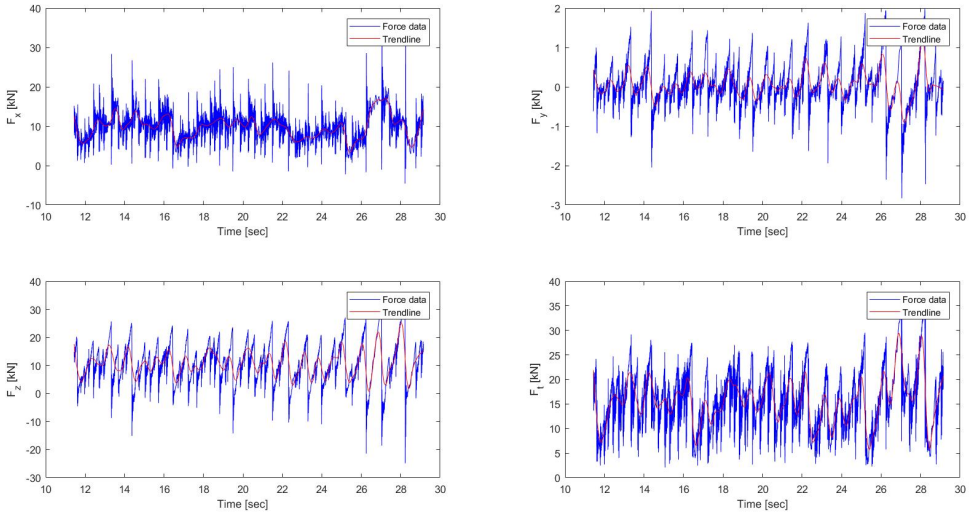

Figure 63: Experiment 7.2C: force in time

Table 40: Laboratory data of experiment 7.2C

	Cutting time [sec]	Average depth [cm]	Average width [cm]	Length [m]	Weight [kg]
Experiment 7.2C	18	1.18	11.20	0.9	0.970

Table 41: Cutting forces of experiment 7.2C

	$F_{x,max}$ [kN]	$F_{x,mean}$ [kN]	$F_{y,max}$ [kN]	$F_{y,mean}$ [kN]	$F_{z,max}$ [kN]	$F_{z,mean}$ [kN]	$F_{t,max}$ [kN]	$F_{t,mean}$ [kN]
Experiment 7.2C	37.39	9.76	1.98	0.06	32.54	10.55	37.81	15.47

.30. EXPERIMENTS 7.2A-7.2C: MAXIMUM FORCES OVER DEPTH

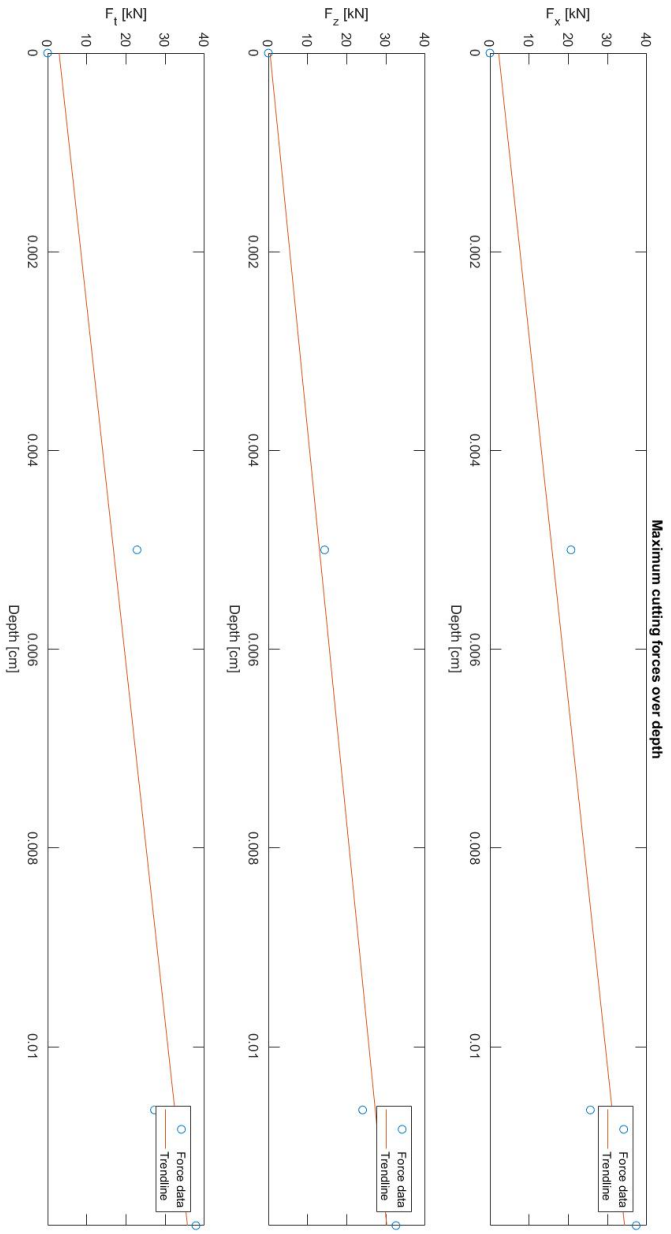

Figure 64: Experiment 19-21: maximum forces over depth

.31. EXPERIMENTS 7.2A-7.2C: CUTTING PROFILES

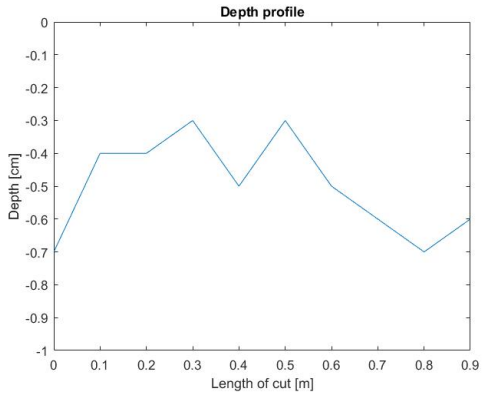

(a) Depth of cut

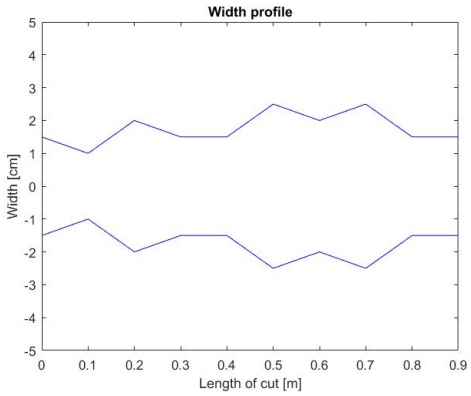

(b) Width of cut

Figure 65: Depth and width of experiment 7.2A

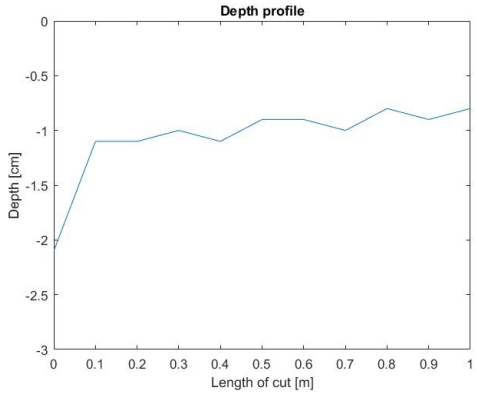

(a) Depth of cut

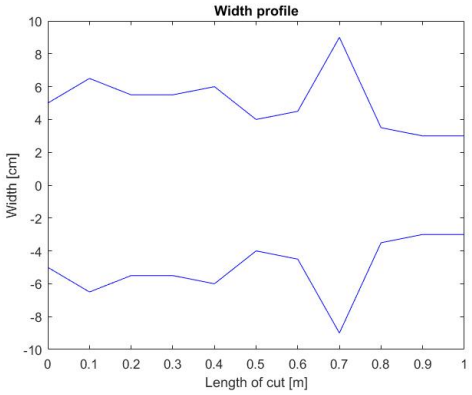

(b) Width of cut

Figure 66: Depth and width of experiment 7.2B

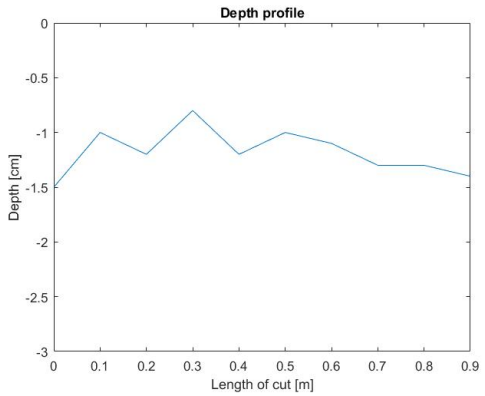

(a) Depth of cut

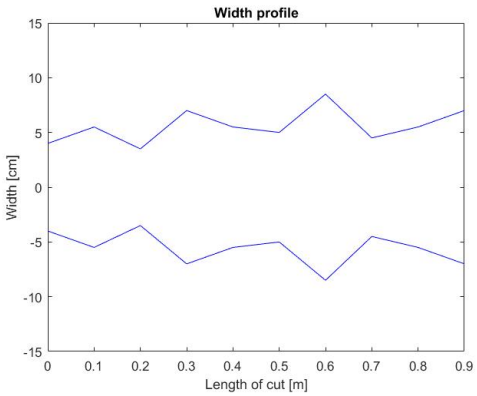

(b) Width of cut

Figure 67: Depth and width of experiment 7.2C

.32. EXPERIMENTS 7.2A-7.2C: PARTICLE SIZE DISTRIBUTIONS

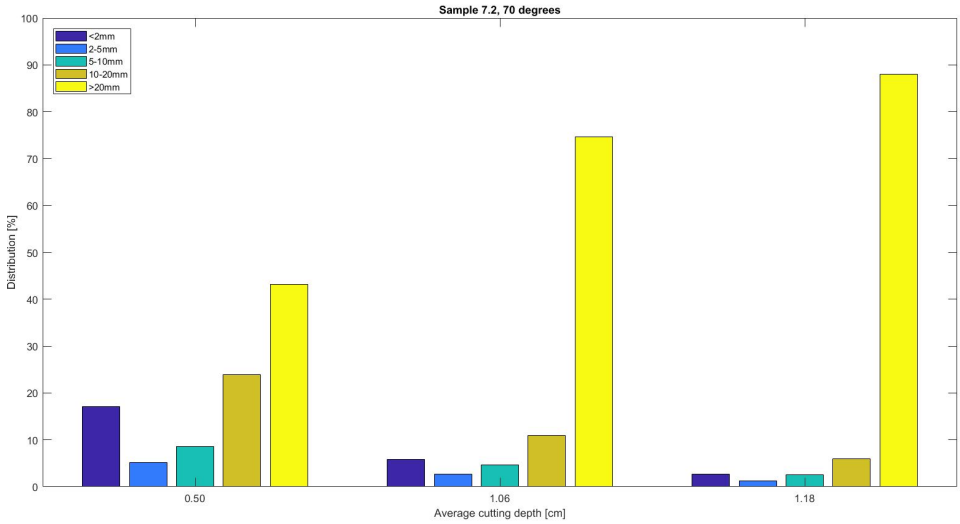

Figure 68: Particle size distributions experiments 19-21

INDENTATION FORCES OVER CUTTING DEPTH

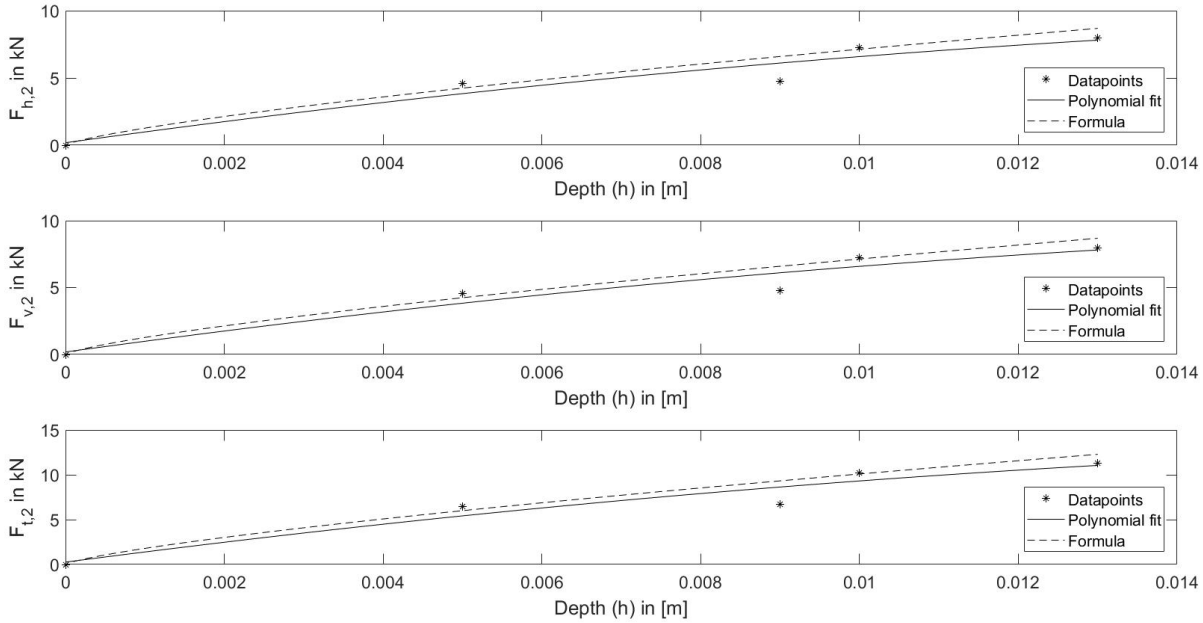

Figure 69: Formula compared with the 40° dataset

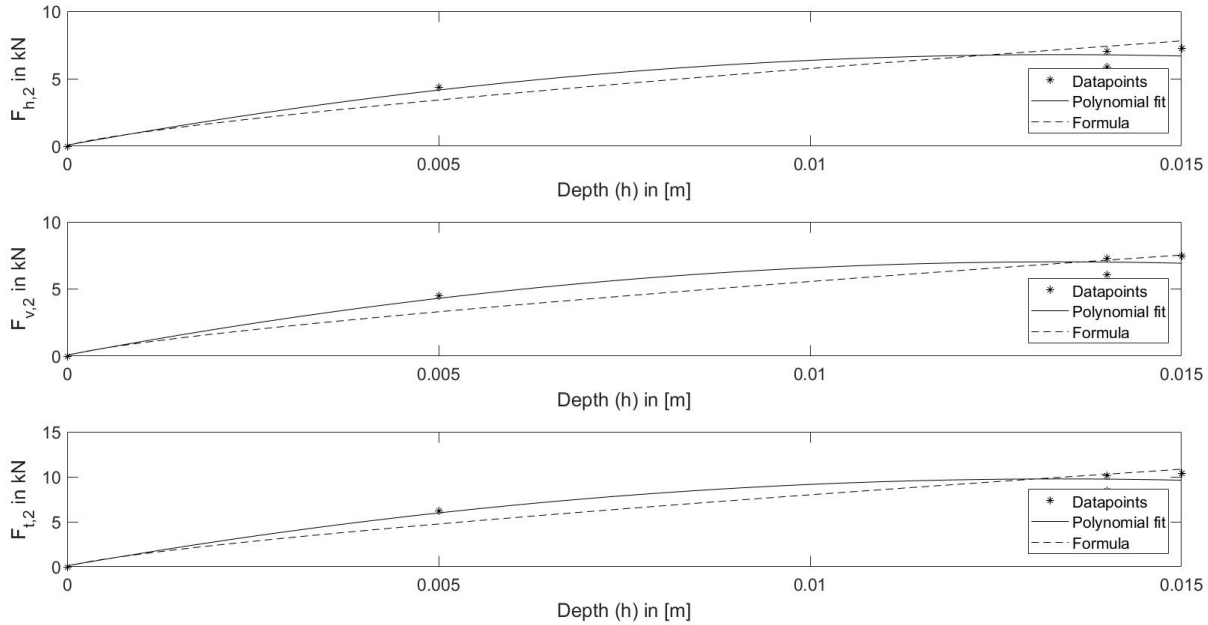

Figure 70: Formula compared with the 45° dataset

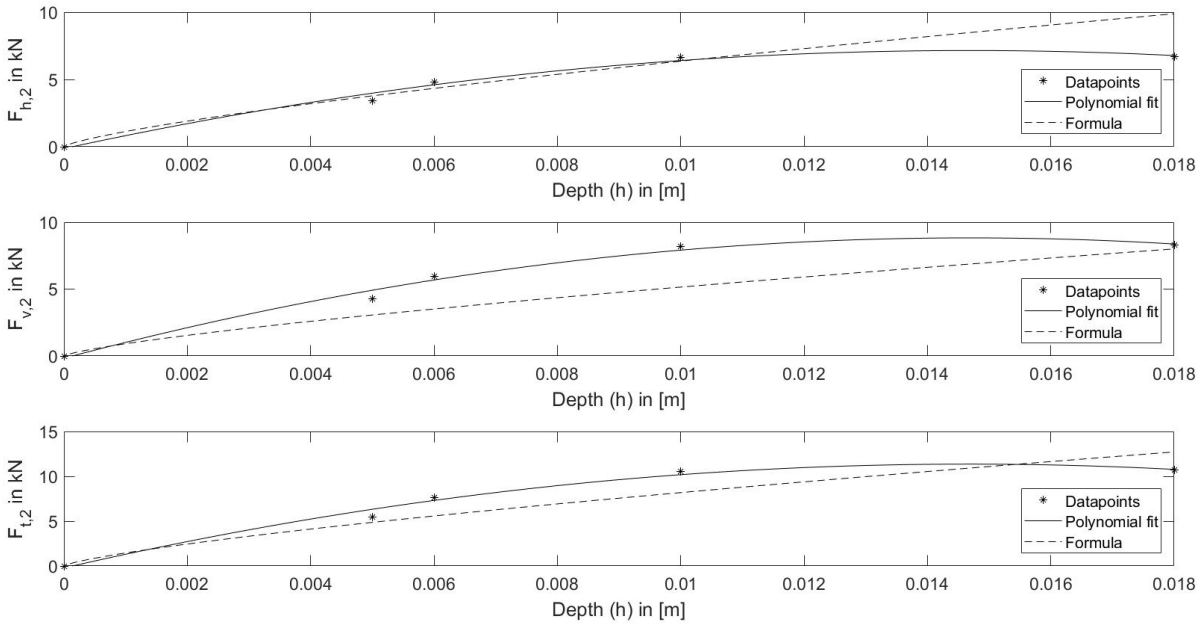

Figure 71: Formula compared with the 50° dataset

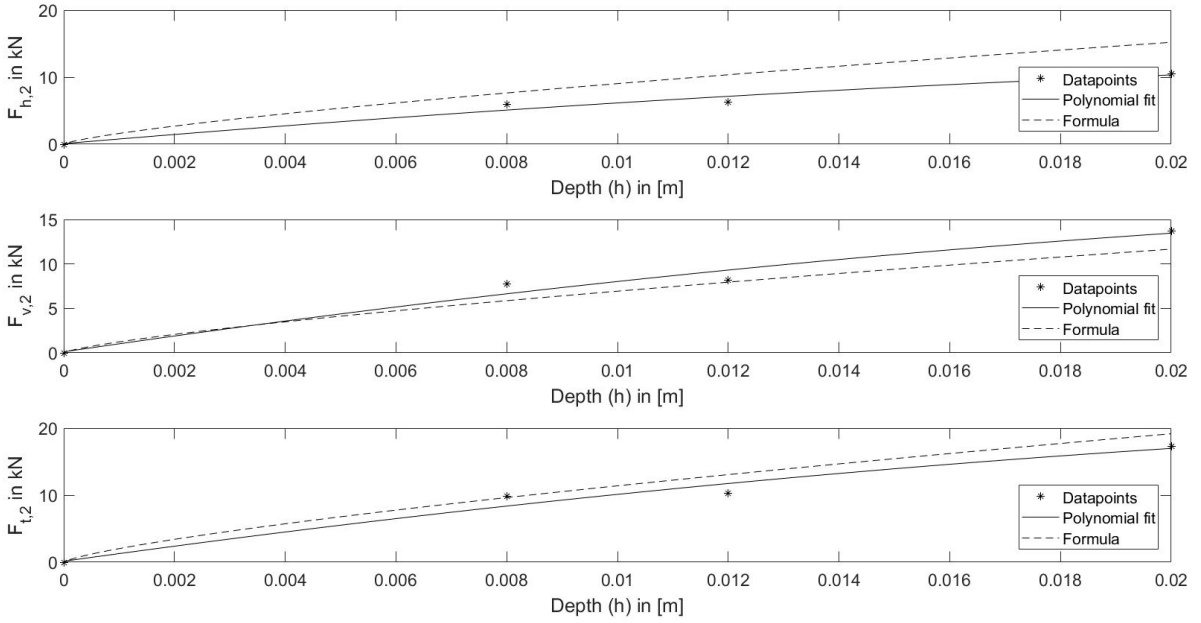

Figure 72: Formula compared with the 55° dataset

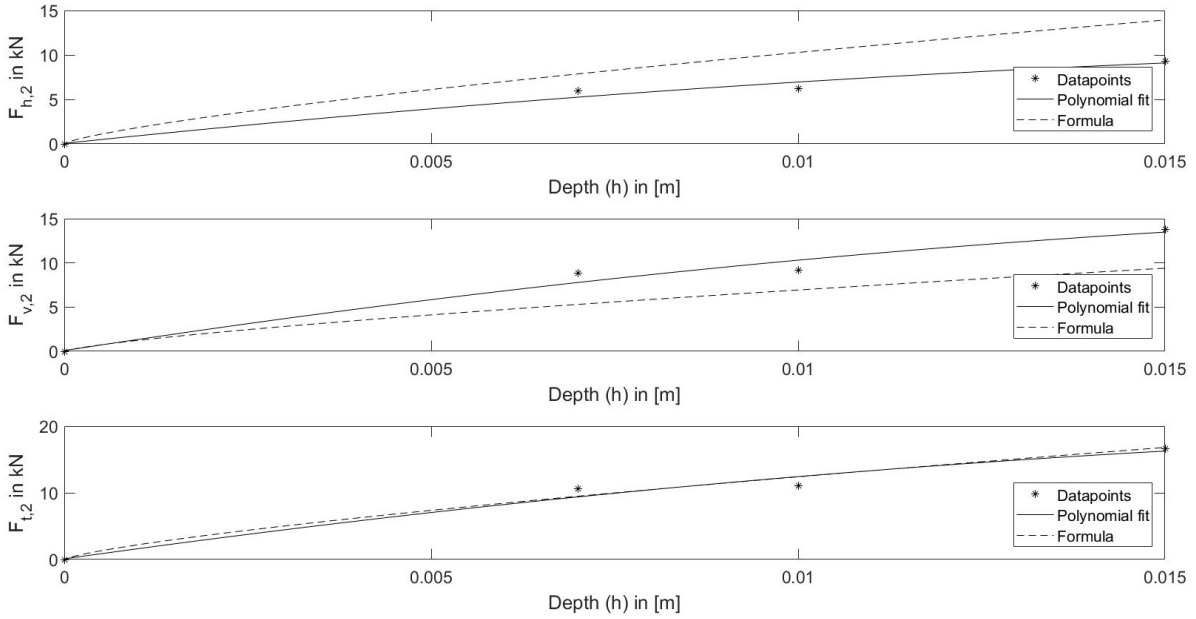

Figure 73: Formula compared with the 60° dataset

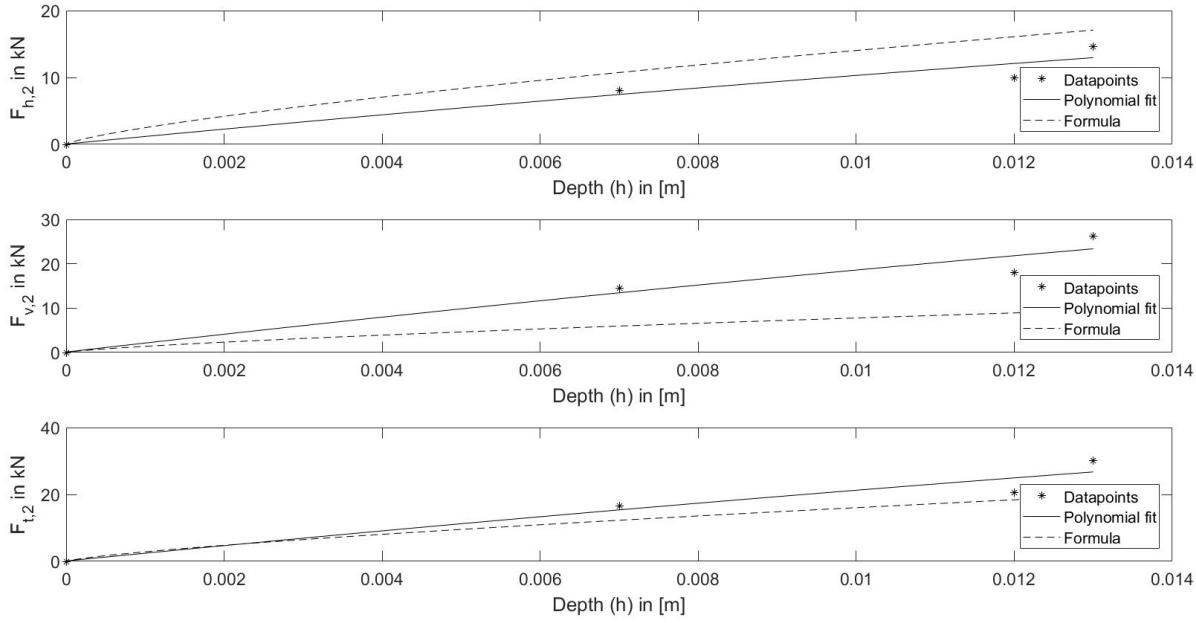

Figure 74: Formula compared with the 70° dataset

TOTAL AREA OF SHEAR PLANE PER EXPERIMENT

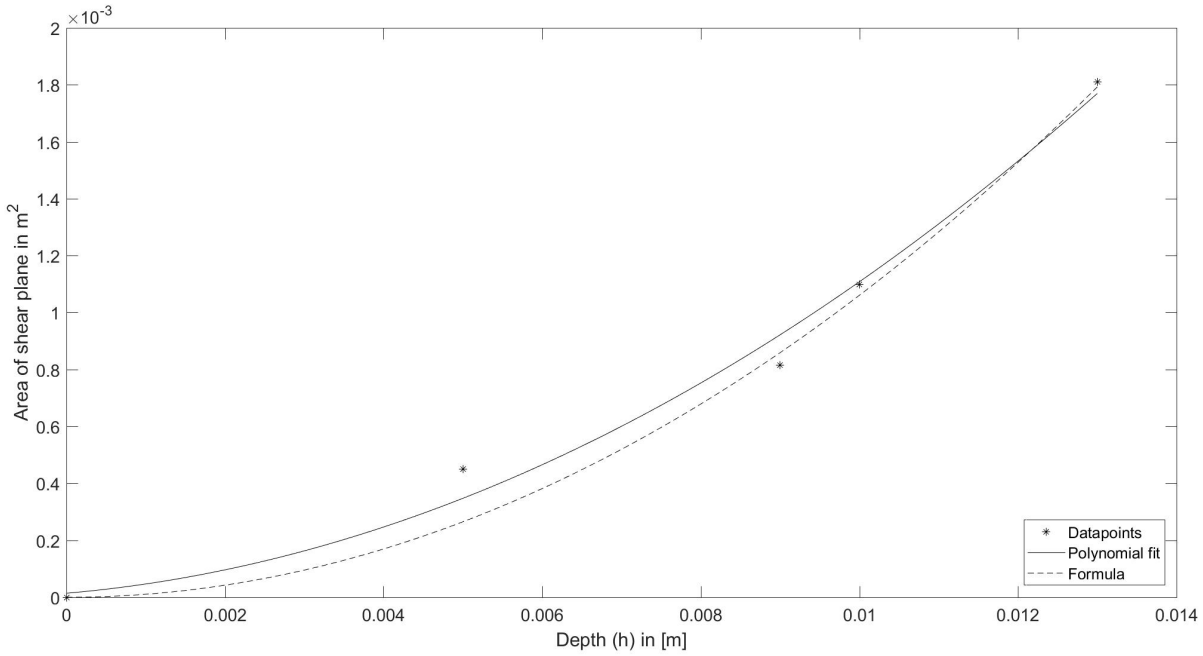

Figure 75: Data points, polynomial fit and composed formula for sample number 5 with 40° cutting angle

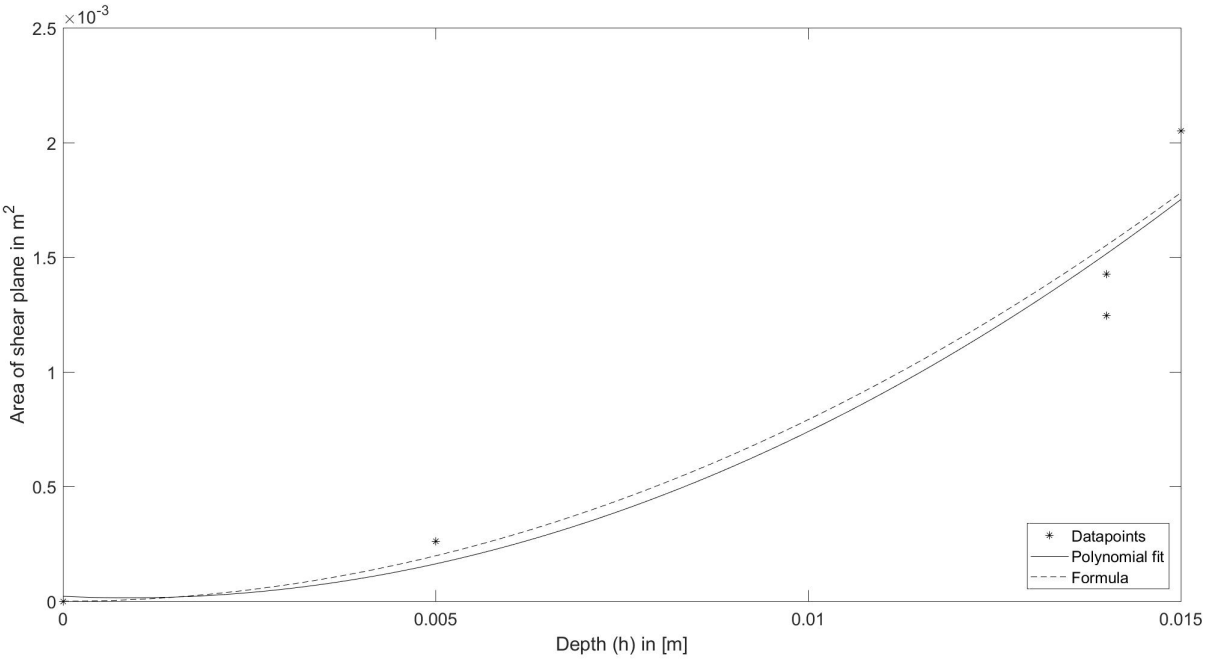

Figure 76: Data points, polynomial fit and composed formula for sample number 9 with 45° cutting angle

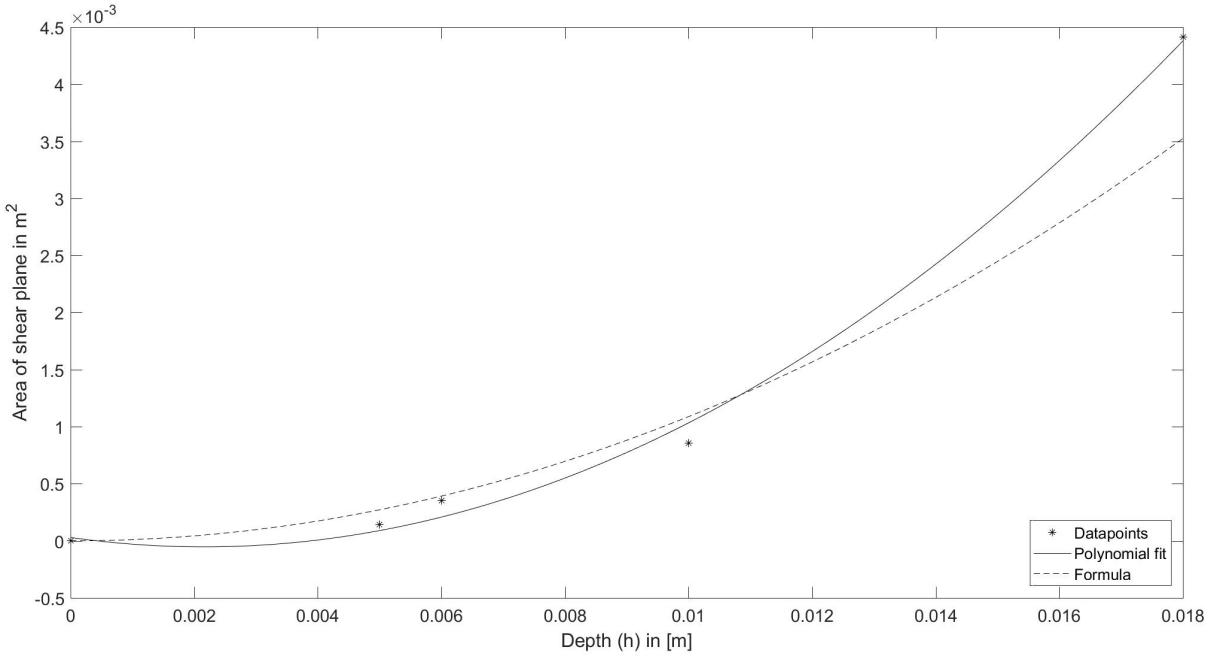

Figure 77: Data points, polynomial fit and composed formula for sample number 8 with 50° cutting angle

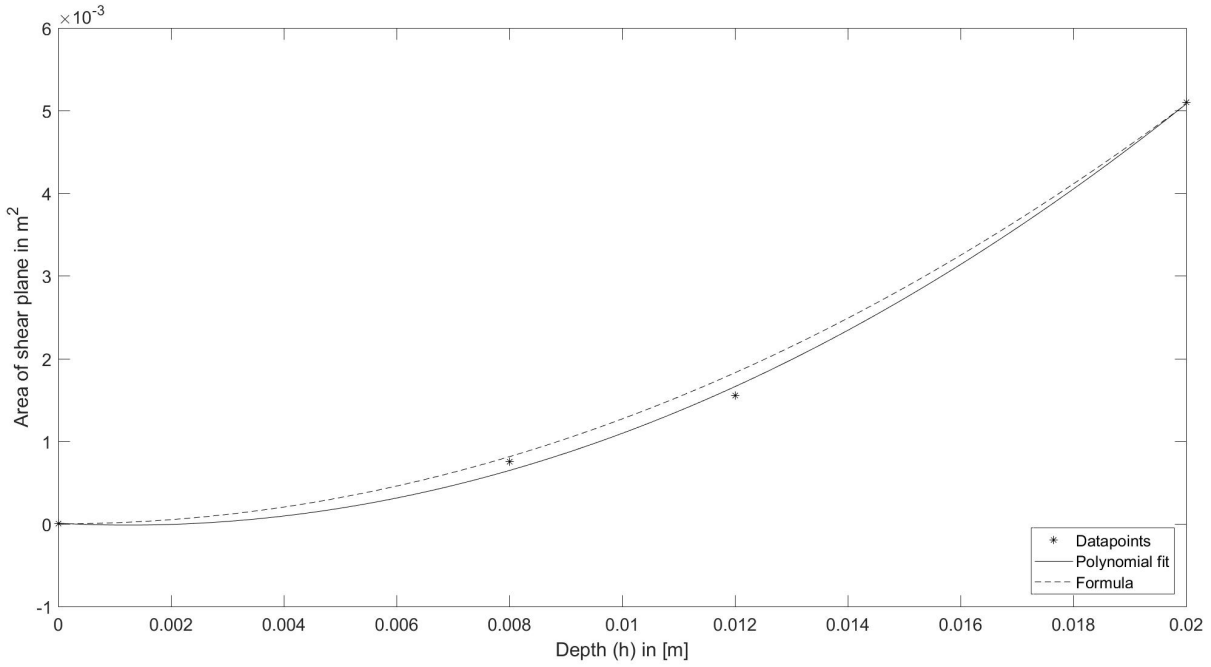

Figure 78: Data points, polynomial fit and composed formula for sample number 6 with 55° cutting angle

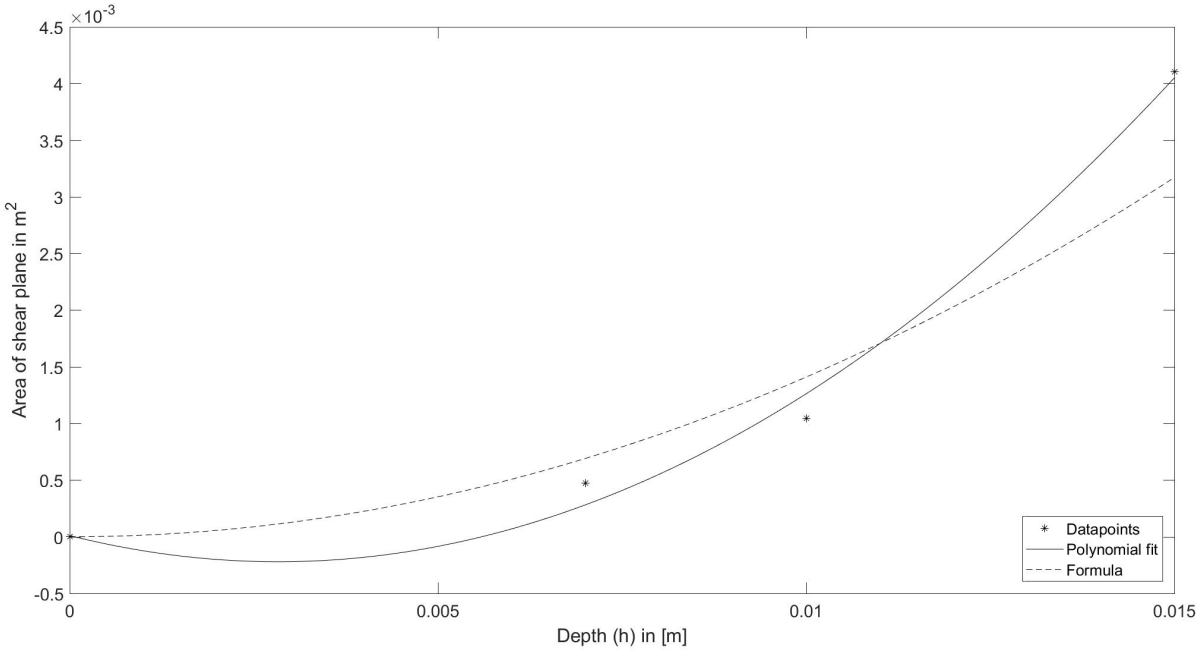

Figure 79: Data points, polynomial fit and composed formula for sample number 7 with 60° cutting angle

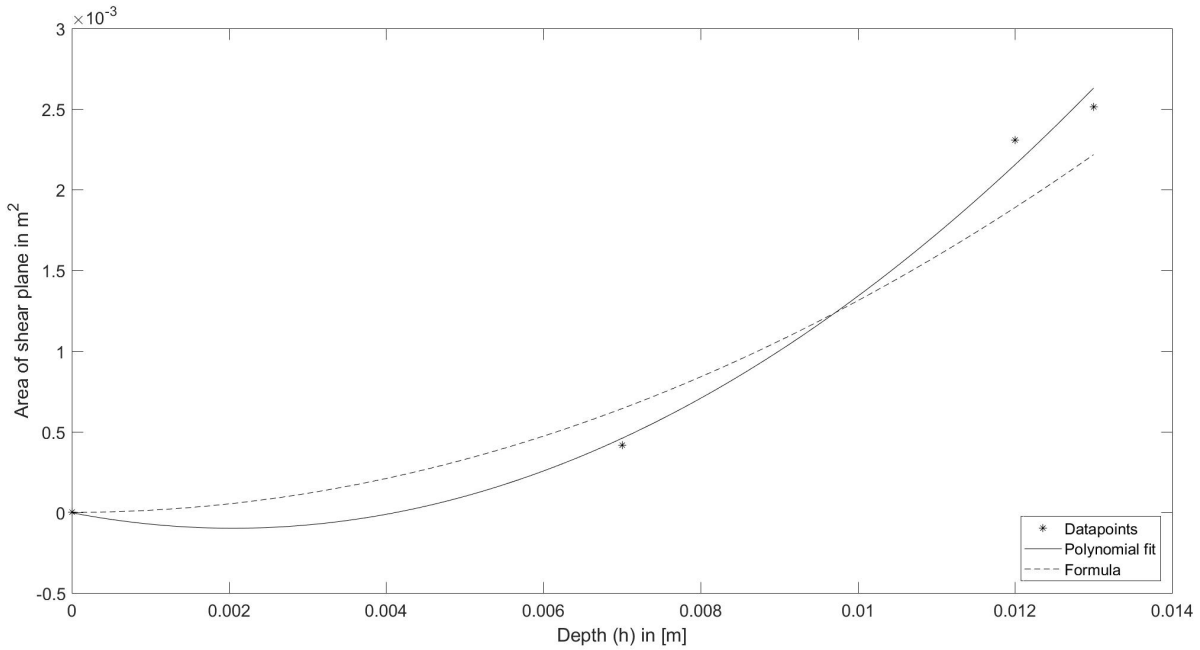

Figure 80: Data points, polynomial fit and composed formula for sample number 7 with 70° cutting angle